IntechOpen

Ballistics

Edited by Charles Osheku

BALLISTICS

Edited by **Charles Osheku**

Ballistics
http://dx.doi.org/10.5772/intechopen.71462
Edited by Charles Osheku

Contributors

Luis Cadarso, Raúl De Celis, Waseem Ghazi Alshanti, Catalin Pirvu, Lorena Deleanu, Bhar Kisabo Aliyu, Charles Attah Osheku, Oluleke Babayomi

First published in London, United Kingdom, 2019 by IntechOpen
IntechOpen is the global imprint of INTECHOPEN LIMITED, registered in England and Wales, registration number: 11086078, The Shard, 25th floor, 32 London Bridge Street
London, SE19SG – United Kingdom
Printed in Croatia

British Library Cataloguing-in-Publication Data
A catalogue record for this book is available from the British Library

Additional hard and PDF copies can be obtained from orders@intechopen.com

Ballistics, Edited by Charles Osheku
p. cm.
Print ISBN 978-1-83880-655-2
Online ISBN 978-1-83880-656-9
eBook (PDF) ISBN 978-1-83880-715-3

Meet the editor

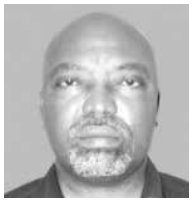

Dr. Charles Attah Osheku was the Director of the Centre for Space Transport and Propulsion, Epe, Lagos, an activity Centre of the National Space Research and Development Agency, Nigeria. He obtained his BSc in Mechanical Engineering from the Obafemi Awolowo University and his MSc and PhD in Mechanical Engineering (Engineering Mechanics) from the University of Lagos, Nigeria. He was the incumbent chairman of the Lagos Branch of Nigeria Society of Engineers' Space Engineering Division and a board member of the Division. Dr. Osheku was a research expert in rockets and missiles; solid fuel physics; solid rocket engine design; structural, flow, and combustion-induced vibrations; aircraft and jet noise modeling; and dissipation and vibration of laminated structures. He has 63 scientific papers to his credit, published in reputable international journals, and ASME International Offshore Mechanics Conferences. He was a COREN (Nigeria)-registered engineer and a professional member of ASME and AIAA.

Contents

Preface

This edited volume is a collection of reviewed and relevant research chapters concerning developments within the ballistics field of study. The book includes scholarly contributions by various authors and is edited by a group of experts pertinent to engineering mechanics. Each contribution comes as a separate chapter complete in itself but directly related to the book's topics and objectives.

The book includes chapters dealing with the following topics: adaptive navigation, guidance and control techniques applied to projectiles and rockets, state-space modeling of a rocket for optimal control system design, discrete element modeling of a projectile impacting and penetrating into granular systems, analytical prediction for grain burn tie and burning area kinematics in a solid rocket combustion chamber and ballistic testing of armor panels based on aramid. The target audience comprises scholars and specialists in the field.

Note from the publisher:

It is with great sadness and regret that we inform the contributing authors and future readers of this book that the Editor, Dr. Charles Attah Osheku, passed away during the publishing process of the book and before having a chance to see its publication. Dr. Osheku was IntechOpen's long-term collaborator and edited his first book with us in 2018 (*Lamination*). The book *Ballistics* was his second edited volume and contains his third published chapter with us. Fruitful collaboration continued until his final days. We would like to acknowledge Dr. Osheku's contribution to scientific publishing, which he made during years of dedicated work, and express our gratitude for his pleasant cooperation with us.

Chapter 1

Adaptive Navigation, Guidance and Control Techniques Applied to Ballistic Projectiles and Rockets

Raúl de Celis and Luis Cadarso

Additional information is available at the end of the chapter

http://dx.doi.org/10.5772/intechopen.73511

Abstract

Accuracy and precision are the cornerstone for ballistic projectiles from the earliest days of this discipline. In the beginnings, impact point precision in artillery devices deteriorated when range were extended, particularly for non-propelled artillery rockets and shells. Later, inertial navigation and guidance systems are introduced and precision was unlinked from range increases. In the last 30 years, hybridization between inertial systems and GNSS devices has improved precision enormously. Unfortunately, during the last stages of flight, inertial and GNSS methods (hybridized or not) feature big errors on attitude and position determination. Low cost devices, which are precise on terminal guidance and do not feature accumulative error, such as quadrant photo-detector, seem to be appropriate to be included on the guidance systems. Hybrid algorithms, which combine GNSSs, IMUs and photodetectors, and a novel technic of attitude determination, which avoids the use of gyroscopes, are presented in this chapter. Hybridized measurements are implemented on modified proportional navigation law and a rotatory force control method. A realistic non-linear flight dynamics model has been developed to perform simulations to prove the accuracy of the presented algorithms.

Keywords: rockets, artillery, flight mechanics, navigation, guidance, control, semi-active laser

1. Introduction

A precision-guided munition (PGM) is a guided munition intended to precisely hit a specific target, and to minimize collateral damage. Considering that the damage effects of explosive weapons decrease with distance, even modest improvements in accuracy enable a target to be attacked with fewer or smaller bombs. The precision of these weapons is dependent both on

the precision of the measurement system used for location determination and the precision in setting the coordinates of the target. The latter critically depends on intelligence information, not all of which is accurate. If the targeting information is accurate, satellite-guided weapons (including inertial navigation in the event of signal loss) are significantly more likely to achieve a successful strike in any given weather conditions than any other type of precision-guided munition [1].

Development of low-cost navigation, guidance and control technologies for unguided rockets is a unique engineering challenge. Over the past several decades, numerous solutions have been proposed, primarily for large artillery projectiles or for slowly rolling airframes [1, 2].

GNSS/IMU hybridizing systems provide accurate solutions for PGMs but in some occasions these solutions might not be enough. For those systems, a circle error probable (CEP) is around 10–20 m in the best cases [3].

Development of algorithms for low-cost high-precision terminal guidance systems is a cornerstone in research on PGMs. [4] propose a robust guidance law which is mainly suitable for systems characterized by moderate glint levels such as electro-optical missiles [5] present a new precision guidance law for three-dimensional intercepts. In contrast to previously published guidance laws, it does not require knowledge of the range to the target. This makes it appropriate for use on platforms which have an imaging device, such as a video camera, as a primary sensor.

Whit the aim of reducing costs, many inertial navigation systems could be replaced with less accurate devices if it were guaranteed that GNSS signal would be continuously available to update the inertial system to limit its error growth.

However, given the uncertainty in most scenarios, an alternate way to reduce system cost and collateral damage is to lower the cost by developing lower-cost inertial sensors while improving their accuracy using other sources of navigation information such as Semi Active laser kits. The benefits of integrated data fusion have been demonstrated across the spectrum of antisubmarine, tactical air, and land warfare [6].

In the research described in this chapter, two measured quantities are used to obtain attitude information for high dynamic and spin rate vehicles: speed and gravity vectors. They are obtained in two different reference frames using a GNSS sensor and a strap-down accelerometer. After that, attitude determination algorithm is integrated in the global hybridized system together with SAL and inertial measurements. Non-linear flight simulations are performed to prove the applicability of the proposed approach for ballistic rocket navigation, guidance, and control.

1.1. Semi-active laser photodetectors (SAL)

Semi-active laser photodetectors (SAL), and particularly quadrant detector devices, have been developed to improve precision in guided weapons. Quadrant photo-detectors have been applied in many engineering ambits, such as measurement, control, laser collimation, target tracking, and particularly in PGM terminal guidance [7]. One of the greatest advantages of quadrant detector

http://dx.doi.org/10.5772/intechopen.73511

equipment is the high performance provided in terms of guidance, typically in the last stages of the trajectory, as compared to the low cost incurred. Coordination can be achieved without requiring lengthy transfer of coordinates which is susceptible to errors. But, constant lines of sight between the target, laser designator and the weapon must be maintained [3].

Quadrant photo-detector is a uniform disk made of silicon containing two gaps across the diameters. There are four independent and equal photo-detectors on the sensing surface, one on each quadrant. The centre of the detector is known very accurately since it is the mechanical intersection of the two gap lines and is not pretended to change with time or temperature. A symmetrical laser or other optical beam centered on the detector generates equal currents from each of the four sectors. If the beam moves from the centre of the detector, the currents from the four sectors change, and a processing method may give the coordinate displacements relative to the centre [8]. Precision on determining the coordinates of intersection of the beam with the photo-detector will determine the key points on the Navigation and Guidance algorithms for the terminal phase on a PGM. A wide dissertation on improving precision in this photodetector is presented in [3].

Modern laser guided ballistic rockets are integrating IMU, GPS and laser guidance capability, offering high precision, all-weather attack capability. For example, [9] design a missile target tracker using a filter/correlator based on forward-looking infrared sensor measurements. In this chapter, improvements on existing methods for terminal guidance are presented, which apply an effective hybridization algorithm in order to obtain an accurate vector between rocket and target from a combination of sensors previously mentioned, namely IMU, GPS and SAL.

1.2. Attitude determination technics and integration on the global guidance

Obtaining precise attitude information is essential for navigation and control. Its effectiveness is determined by the degree of precision of navigation and control systems, including inertial measurement units [10]. There is an extensive body of literature regarding attitude estimation using various sensor inputs [11].

Traditionally, in order to obtain accurate values for determining attitude, expensive and/or weighty units, such as laser or fiber optic gyroscopes and accelerometers, or their MEMS equivalents, must be employed. Moreover, when high-demanding maneuvers are performed this equipment may become extremely expensive.

It is well-known that the attitude of an aero-vehicle may be determined, starting from an initial condition, integrating the angular rates (pitch, roll, and yaw rates) of the vehicle and propagating them forward in time. Nevertheless, accuracy requirements usually cannot be satisfied by using inexpensive sensors [10]. This problem becomes even more important when the vehicle cannot be reused: low-cost attitude determination systems are of key importance for these applications.

For example, [12] describe an attitude determination system that is based on two measurements of non-zero, non-co-linear vectors. Using the Earth's magnetic field and gravity as the two measured quantities, a low-cost attitude determination system is proposed.

[13] develop an inexpensive Attitude Heading Reference System for general aviation applications by fusing low cost automotive grade inertial sensors with GPS. The inertial sensor suit consists of three orthogonally mounted solid-state rate gyros.

[14] describe an attitude estimation algorithm derived by post-processing data from a small low cost Inertial Navigation System recorded during the flight of a sub-scale commercial off the shelf UAV. Estimates of the UAV attitude are based on MEMS gyro, magnetometer, accelerometer, and pitot tube inputs.

[15] state that low-cost GNSS receivers and antennas can provide a precise attitude and drift-free position information, but accuracy is not continuous. Inertial sensors are robust to GNSS signal interruption and very precise over short time frames, which enables a reliable cycle slip correction. But low-cost inertial sensors suffer from a substantial drift. The authors propose a tightly coupled position and attitude determination method for two low-cost GNSS receivers, a gyroscope and an accelerometer and obtain a heading with an accuracy of 0.25° and an absolute position with an accuracy of 1 m.

Similar developments may be found within space vehicles, for example in [16]. In [17] the use of an inertial navigation system (INS) and a multiple GPS antenna system for attitude determination of an off-road vehicle is developed. And in [18], attitude determination using GPS carrier phase is successfully applied to aircraft in experiments.

Also, improved algorithms for estimating attitude in case of failures have been proposed in the literature. For example, [19] introduce algorithms with filter gain correction for the case of measurement malfunctions. Two different algorithms are proposed and applied for the attitude estimation process of a pico-satellite. The results of these algorithms are compared for different types of measurement faults in different estimation scenarios and recommendations about their applications are given.

However, as stated in [20], many of the presented methods, such as the ones employing local magnetic field vectors, are only valid for estimating the orientation of a slow-rotation body: for high spin rate bodies, electromagnetic interactions degrade magnetic measurements.

2. Non-linear flight dynamics model

This segment portrays the nonlinear flight dynamic model utilized as a part of this tests, including actuations, and navigation and control performances.

2.1. Rocket

The guidance and control detailing proposed in this investigation applies to a 140-mm axisymmetric turning rocket with wrap around balancing out blades. It highlights supersonic dispatch speed and a turn rate of roughly 150 Hz. The control system features a roll-decoupled fuse set at the nose of the rocket. This fuse is composed of four canard surfaces, decoupled 2 by 2. keeping in mind the end goal to produce control regulated in modulus and argument, situated in an orthogonal plane in respect to rocket, and its related moment as it is exposed in **Figure 1**.

The non-controlled solid propellant thrust, mass, inertia moments (I_x and I_y) and centre of gravity coordinate from nose (X_{CG}) versus time are shown in **Table 1**.

Numerical simulations were employed to determine aerodynamic coefficients for the rocket under examination, which are showed in **Figure 2**.

2.2. Coordinate systems definition

Two axis systems are defined along this paper: north east down axes (*NED*) and body axes (*B*). NED axes are defined by sub index *NED*. x_{NED} pointing north, y_{NED} perpendicular to x_{NED} and pointing East, and z_{NED} forming a clockwise trihedron. Body axes are defined by sub index *B*.

Figure 1. The 140-mm axisymmetric rocket with wrap around fins and a roll-decoupled fuse.

Time (s)	0.00	0.02	0.10	0.20	0.70	1.20	1.70	1.75	1.95	2.00	2.15	2.30	2.70	3.20	100.00
Thrust (kN)	0.00	25.00	22.50	23.00	24.00	25.50	28.50	29.16	15.00	10.00	5.00	2.50	0.00	0.00	0.00
Mass (kg)	62.40	62.30	61.52	60.58	55.76	50.67	45.13	44.54	42.72	42.47	42.00	41.77	41.57	41.57	41.57
$I_x\ (m \cdot s^2)$	0.19	0.19	0.19	0.19	0.18	0.17	0.16	0.16	0.15	0.15	0.15	0.15	0.15	0.15	0.15
$I_y\ (m \cdot s^2)$	18.85	18.83	18.71	18.57	17.80	16.96	16.02	15.91	15.59	15.54	15.46	15.42	15.38	15.38	15.38
$X_{CG}\ (m)$	1.13	1.13	1.13	1.13	1.11	1.10	1.07	1.07	1.06	1.06	1.06	1.06	1.06	1.06	1.06

Table 1. 140 mm axisymmetric rocket main parameters versus time.

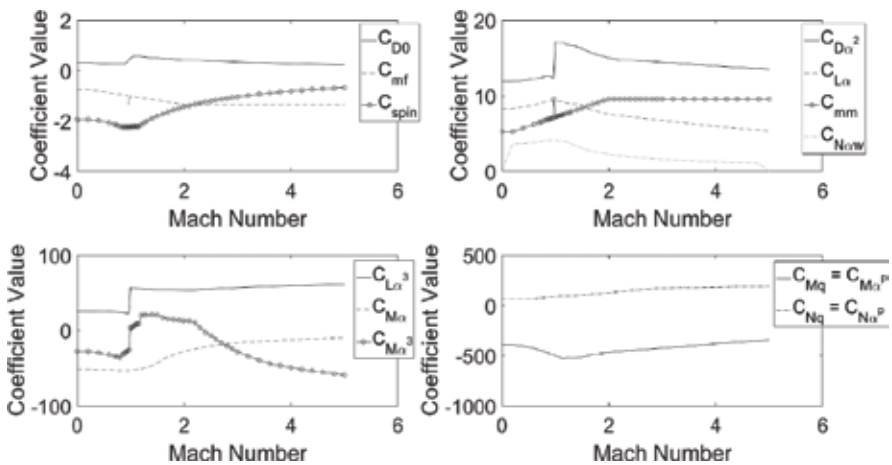

Figure 2. Aerodynamic coefficients vs. Mach number.

x_B pointing forward and contained in the plane of symmetry of the rocket, z_B perpendicular to x_B, pointing down and contained in the plane of symmetry of the rocket, and y_B forming a clockwise trihedral. The origin of body axes is located at the centre of mass of the rocket and they are severely coupled to the roll-decoupled fuse. This concept is shown on **Figure 3**.

2.3. Mathematical equations

Total forces and moments on the rocket are given (expressed in body axes) by (1) and (2), respectively:

$$\vec{F_B}=\vec{D_B}+\vec{L_B}+\vec{M_B}+\vec{P_B}+\vec{T_B}+\vec{W_B}+\vec{C_B}+\vec{CF_B}\,, \tag{1}$$

$$\vec{M_B}=\vec{O_B}+\vec{P_{M_B}}+\vec{M_{M_B}}+\vec{S_B}+\vec{CM_B} \tag{2}$$

where $\vec{D_B}$ is the drag force, $\vec{L_B}$ is the lift force, $\vec{M_B}$ is the Magnus force, $\vec{P_B}$ is the pitch damping force, $\vec{T_B}$ is the thrust force, $\vec{W_B}$ is the weight force and $\vec{C_B}$ is the Coriolis force, $\vec{CF_B}$ is the control force executed by the airfoils, $\vec{O_B}$ is the overturn moment, $\vec{P_{M_B}}$ is the pitch damping moment, $\vec{M_{M_B}}$ is the Magnus moment and $\vec{S_B}$ is the spin damping moment and $\vec{CM_B}$ is the control moment executed by the airfoils. Rocket forces in body axes include contributions from drag,

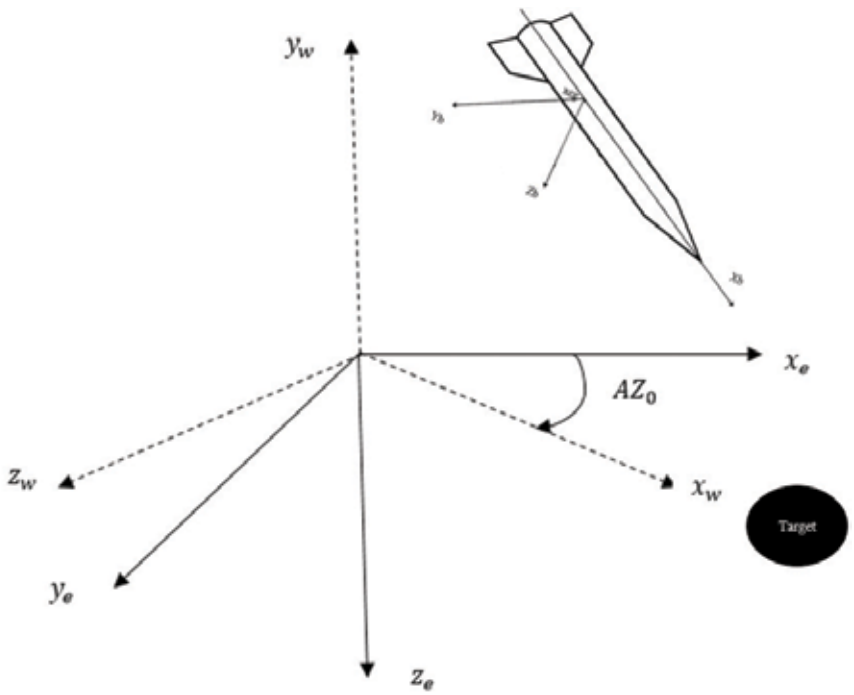

Figure 3. Reference systems.

lift, Magnus, pitch damping, thrust, weight and Coriolis forces, which are described by the following expressions:

$$\vec{D_B} = -\frac{\pi}{8} d^2 \rho \left(C_{D_0} + C_{D_{\alpha^2}} \alpha^2 \right) \left\| \vec{v_B} \right\| \vec{v_B} \,, \tag{3}$$

$$\vec{L_B} = -\frac{\pi}{8} d^2 \rho \left(C_{L_\alpha} \cdot \alpha + C_{L_{\alpha^3}} \alpha^2 \right) \left(\left\| \vec{v_B} \right\|^2 \vec{x_B} - \left(\vec{x_B} \cdot \vec{v_B} \right) \vec{v_B} \right), \tag{4}$$

$$\vec{M_B} = -\frac{\pi}{8} d^3 \rho \frac{C_{mf}}{I_x} \left(\vec{L_B} \cdot \vec{x_B} \right) \left(\vec{x_B} \times \vec{v_B} \right), \tag{5}$$

$$\vec{P_B} = \frac{\pi}{8} d^3 \rho \frac{C_{Nq}}{I_y} \left\| \vec{v_B} \right\|^2 \left(\vec{L_B} \times \vec{x_B} \right), \tag{6}$$

$$\vec{T_B} = T(t) \, \vec{x_B} \,, \tag{7}$$

$$\vec{W_B} = m \, \vec{g_B} \,, \tag{8}$$

$$\vec{C_B} = -2m \, \vec{\Omega} \times \vec{v_B} \,, \tag{9}$$

where d is the rocket caliber, ϱ is the air density, C_{D_0} is the drag force linear coefficient, $C_{D_{\alpha^2}}$ is the drag force square coefficient, α is the total angle of attack, C_{L_α} is the lift force linear coefficient, $C_{L_{\alpha^3}}$ is the lift force cubic coefficient, C_{mf} is the Magnus force coefficient, $\vec{L_B}$ is the rocket angular momentum expressed in body axes, I_x *and* I_y are the rocket inertia moments in body axes, C_{Nq} is the pitch damping force coefficient, $\vec{x_B}$ is the rocket nose pointing vector expressed in body axes, $\vec{g_B}$ is the gravity vector in body axes, $\vec{\Omega}$ is the earth angular speed vector, and $\vec{v_B}$ is the rocket velocity expressed in body axes.

Keeping in mind the end goal to demonstrate the control forces and moments in body reference frame for each of the four fins, it must be viewed as first the effective incidence aerodynamic speed on each of the four control surfaces. The expressions for control force on each of the four control surfaces are characterized in the accompanying equations:

$$\vec{CF_B} = \sum_{i=1}^{4} \left[\frac{1}{8} \frac{\alpha_{Ef_i}}{\left\| \alpha_{Ef_i} \right\|} d^2 \rho \pi \left\| \vec{v_{xEf_i}} \right\|^2 \left[C_{N\alpha w} \cos \alpha_{Ef_i} + \frac{2}{d^2 \pi} S_{exp} \sin^2 \alpha_{Ef_i} \right] \left(\vec{u_{FN_i}} \cos \delta_i - \vec{x_B} \sin \delta_i \right) \right], \tag{10}$$

where $C_{N\alpha w}$ is the aerodynamic coefficient of the normal force for a fin, S_{exp} is the reference surface of the fin, δ_i responds to fin deflection angle, $\vec{u_{FN_i}}$ depends on fin orientation, concretely in body axes, $\vec{u_{FN_1}} = [0\ 1\ 0]$, $\vec{u_{FN_3}} = [0\ -1\ 0]$, $\vec{u_{FN_2}} = [0\ 0\ 1]$, $\vec{u_{FN_4}} = [0\ 0\ -1]$, and, α_{Ef_i} and $\vec{v_{xEf_i}}$ are the effective angle of attack and the effective aerodynamic speed on each of the four fins, respectively. These last two magnitudes are modeled as it is expressed in the following equations:

$$\vec{v_{xEf_i}} = \vec{v_B} - \left[\vec{v_B} \cdot \vec{u_{b_i}} \right] \vec{u_{b_i}} \,, \tag{11}$$

$$\alpha_{Ef_i} = acos\left[\frac{\left(\vec{v_B} - \left[\vec{v_B} \cdot \vec{u_{b_i}}\right]\vec{u_{b_i}}\right)}{\left\|\left(\vec{v_B} - \left[\vec{v_B} \cdot \vec{u_{b_i}}\right]\vec{u_{b_i}}\right)\right\|} \cdot \vec{x_B}\right] + \delta_i, \tag{12}$$

where $\vec{u_{b_i}}$ depends again on fin orientation, concretely in body axes, $\vec{u_{b_2}} = [0\ 1\ 0]$, $\vec{u_{b_4}} = [0\ -1\ 0]$, $\vec{u_{b_3}} = [0\ 0\ 1]$, $\vec{u_{b_1}} = [0\ 0\ -1]$.

Likewise, rocket moments in body axes include contributions from overturning, pitch damping, Magnus, and spin damping moments, which are described by the following:

$$\vec{O_B} = \frac{\pi}{8} d^3 \rho \left(C_{M_\alpha} + C_{M_{\alpha^3}} \alpha^2\right) \left\|\vec{v_B}\right\|^2 \left(\vec{v_B} \times \vec{x_B}\right) \tag{13}$$

$$\vec{P_{M_B}} = \frac{\pi}{8} \frac{d^3 \rho}{I_y} C_{M_q} \left\|\vec{v_B}\right\| \left(\vec{L_B} - \left(\vec{L_B} \cdot \vec{x_B}\right) \vec{x_B}\right) \tag{14}$$

$$\vec{M_{M_B}} = -\frac{\pi}{8} \frac{d^4 \rho}{I_x} C_{mm} \left(\left(\vec{L_B} \cdot \vec{x_B}\right)\left(\left(\vec{v_B} \cdot \vec{x_B}\right) \vec{x_B}\right) - \vec{v_B}\right) \tag{15}$$

$$\vec{S_B} = \frac{\pi}{8} \frac{d^4 \rho}{I_x} C_{spin} \left\|\vec{v_B}\right\| \left(\vec{L_B} \cdot \vec{x_B}\right) \vec{x_B} \tag{16}$$

where C_{M_α} is the overturning moment linear coefficient, $C_{M_{\alpha^3}}$ is the overturning moment cubic coefficient, C_{M_q} is the pitch damping moment coefficient, C_{mm} is the Magnus moment coefficient and C_{spin} is the spin damping moment coefficient.

The control moment provided by the control surfaces may be expressed as follows:

$$\vec{CM_B} = \sum_{i=1}^{4} \left[\left[\left(d_{ax}\ \vec{x_B} + d_{lat}\ \vec{u_{b_i}}\right] \times \vec{CF_{B_i}}\right], \tag{17}$$

where d_{ax} is the longitudinal distance, parallel to $\vec{x_B}$, of fin centre of pressure (CP) to rocket centre of mass (CG), which depends on Mach number; d_{lat} is the lateral distance, which is orthogonal to $\vec{x_B}$ and parallel to $\vec{u_{b_i}}$ for each fin, from fin centre of pressure to rocket centre of mass, which is supposed to be constant in this model.

To solve the motion of the rocket a body reference frame, which is coupled to the fuse, is used. Note that, because the fuse is uncoupled from the back part, which turns at high rates, Magnus force and moment and gyroscopic effects coming from the rear part must be modeled and included in the equations of motion. The turn rate of the back piece of the rocket is modeled as follows:

$$p_r = -\int \left(K_s \delta(t_0) - \frac{\frac{\pi}{8} d^4 \rho}{I_x} C_{spin} \left\|\vec{v_B}\right\| \left\|\left(\vec{L_B} \cdot \vec{x_B}\right) \vec{x_B}\right\|\right) dt, \tag{18}$$

where $\delta(t_0)$ is a Dirac's delta and K_s an experimental constant. Note that initial spin speed is modeled as an impulse which correlates to experimental data. It is accepted that the fuse

mass is unimportant, which infers that non-apparent responses are included amongst fuse and aft part. Then, considering the aft impact is communicated as additional forces and moments to the Newton-Euler equations expressed in the B reference framework, the equations of motion may be expressed as follows: $\vec{F_B} = \frac{d\vec{mv_B}}{dt} + \vec{\omega'_B} \times \vec{mv_B}$ and $\vec{M_B} = \frac{d\vec{L'_B}}{dt} + \vec{\omega'_B} \times \vec{L'_B}$, where $\vec{\omega'_B} = \begin{pmatrix} p_r + p \\ q \\ r \end{pmatrix}$ and $\vec{L'_B} = \begin{bmatrix} I_x & 0 & 0 \\ 0 & I_y & 0 \\ 0 & 0 & I_y \end{bmatrix} \vec{\omega'_B} = \bar{\bar{I}} \cdot \vec{\omega'_B}$ are the angular speed and momentum, respectively, of the joint body, namely rocket and fuse. The aerodynamic and gyroscopic contributions of the aft part are computed separately and moved to the left part of Newton-Euler equations as follows:

$$\vec{M_r} = -\frac{\pi}{8} d^3 \rho \frac{C_{mf}}{I_x} \left[\vec{\omega'_B} \ \bar{\bar{I}} \cdot \vec{x_b} \right] \left(\vec{x_b} \times \vec{v_b} \right), \tag{19}$$

$$\vec{M_{Mr}} = -\frac{\frac{\pi}{8} d^4 \rho}{I_x} C_{mm} \left(\left[\vec{\omega'_B} \ \bar{\bar{I}} \cdot \vec{x_b} \right] \left(\left(\vec{v_B} \cdot \vec{x_B} \right) \vec{x_B} \right) - \vec{v_B} \right), \tag{20}$$

$$\vec{G_r} = -\bar{\bar{I}} \frac{d}{dt} \vec{\omega'_B} + \vec{\omega_B} \times \vec{L'_B}, \tag{21}$$

$$\vec{F_{ext}} + \vec{M_r} = \frac{d\ \vec{mv_B}}{dt} + \vec{\omega_B} \times \vec{mv_B}, \tag{22}$$

$$\vec{M_{ext}} + \vec{M_{Mr}} + \vec{G_r} = \frac{d\ \vec{L_B}}{dt} + \vec{\omega_B} \times \vec{L_B}, \tag{23}$$

where $\vec{M}_r$ is the Magnus force of the rotating part of the rocket, $\vec{M}_{Mr}$ is the Magnus moment of the rotating part of the rocket, $\vec{G}_r$ is the gyroscopic moment of the rotating part of the rocket, p, q and r are the angular speed components of the fuse, $\vec{\omega_B}$.

The conditions of movement given by Eq. (22) and Eq. (23) are integrated forward in time employing a fixed time step Runge-Kutta of fourth order to acquire a single flight trajectory.

3. Semi-active laser quadrant photodetector model

Semi-active laser kit consists of a quadrant photo detector that may be modeled as it is shown in **Figure 4**, where the external circle models the locator and the inward one the laser spot.

In order to estimate laser footprint spot centre coordinates, electric intensities given by each of the photo-diodes (I1; I2; I3 and I4), which depend on area lit up by the laser spot, might be utilized. The following conditions characterize the most reasonable calculation, where x_{quad}, y_{quad} are the calculated laser footprint spot centre coordinates.

$$\begin{bmatrix} x_{quad} \\ y_{quad} \end{bmatrix} = \begin{bmatrix} ln\dfrac{I_2}{I_4} \\ ln\dfrac{I_1}{I_3} \end{bmatrix} \tag{24}$$

The following mathematical relationship is always kept: $\frac{y_c}{x_c} = \frac{y_{quad}}{x_{quad}}$, i.e., the transformation is conformal as showed in (25), where x_c and y_c are the genuine spot focus positions, not positions gotten by (24). Radial measurements may be interpolated introducing desired radius using the equivalences showed by the accompanying **Table 2**, where genuine and measured radial distances, r_c and r_{quad}, respectively, are given by Eqs. (26) and (27):

$$\theta_c = \theta_{quad} = \text{atan}\frac{y_{quad}}{x_{quad}} \tag{25}$$

$$r_{quad} = \sqrt{x_{quad}^2 + y_{quad}^2} \tag{26}$$

$$r_c = f\left(r_{quad}\right) \tag{27}$$

Then, the measurement output of the quadrant detector sensor may be expressed as it is indicated in (28), where R_{quad} is the physical radius of the quadrant detector:

$$\begin{bmatrix} x_c \\ y_c \end{bmatrix} = R_{quad} \begin{bmatrix} r_c \cos\theta_c \\ r_c \sin\theta_c \end{bmatrix} \tag{28}$$

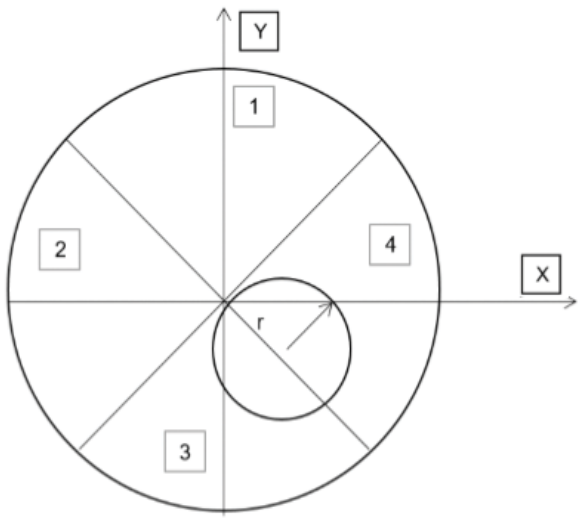

Figure 4. Quadrant photo-detector configuration used.

r_{quad}	0.48	0.99	1.50	2.01	2.67	3.68	5.88
r_c	0.1	0.2	0.3	0.4	0.5	0.6	0.7

Table 2. Interpolation between measured radial distance, r_{quad} and real radial distance, r_c.

4. Trajectory control algorithms

This section describes in detail the proposed navigation, guidance, and control algorithms.

Navigation for this vehicle alludes to the assurance, amid the totality of flight, of the rocket position and attitude, and target position. So as to decide rocket position integration of accelerometers' data and GNSS sensor measurements might be hybridized and utilized as a part of the routing procedure. The elements of these estimations are not objective of this section.

As expressed before, one way for calculating attitude might be the estimation of various vectors in two reference frameworks.

On the off chance that a GNSS sensor gadget is prepared on the flying machine, velocity vector can be specifically calculated from sensor data in the NED axis. Another estimation of the velocity vector in body triad can be acquired from an arrangement of accelerometers prepared on the ship, one on each of the axis. These gadgets can quantify variations in speed. After integrating along time, from an initial condition given, velocity vector can be obtained.

A vector which might be utilized to characterize the rotation of the vehicle is the gravity vector. It is extremely easy to be resolved in NED ternion as it is constantly parallel to z_{NED}. Note that accuracy might be expanded utilizing more entangled models, i.e., it can be demonstrated relying upon latitude and longitude.

The cornerstone of the displayed attitude calculation technique is estimating gravity vector in body axis. For instance, by deciding the constant component of the measured acceleration employing a low pass filter, where Jerk in body axes is calculated by derivation of acceleration; at that point, it is integrated so as to get the non-steady part of increasing speed, and, by subtracting this non-steady segment from the measured acceleration, gravity vector is evaluated. Be that as it may, this technique is not legitimate when the air ship pivots. Another technique to acquire gravity vector is integrating the mechanization equations; at that point, control thusly the subsequent conditions. Once more, gyros are required to implement this method. Basically, it consists on subtracting the contribution of the specific aerodynamic and inertial forces, which can be obtained from expressions (3) to (10) and dividing them by the vehicle mass, from the acceleration measurements of the accelerometers. The Eq. (29) aims to express this fact:

$$\vec{g_B} = \vec{A_B} - \frac{1}{m}\left(\vec{D_B} + \vec{L_B} + \vec{M_B} + \vec{P_B} + \vec{T_B} + \vec{C_B} + \vec{CF_B}\right), \tag{29}$$

where $\vec{g_B}$ is the gravity vector expressed in body axes and $\vec{A_B}$ is the acceleration measured by accelerometers.

Another vector that may be expressed in both reference systems is the line of sight vector, which is especially useful during terminal phase, is the line of sight vector. It can be expressed in NED axes by subtracting target position from vehicle position obtained by GNSS measurements, and in body reference frame from SAL measurements as it is expressed in (30), where d_p is the distance from the quadrant detector to the centre of mass of the rocket.

$$\widetilde{LOS_B} = \frac{\begin{bmatrix} d_p & x_c & y_c \end{bmatrix}}{\sqrt{d_p^2 + x_c^2 + y_c^2}} \tag{30}$$

Attitude can be determined operating with these pairs of vectors with matrixial algorithms as it is stated on [21].

The guidance consists of a modified proportional law, governed by the following equations: Eq. (31) gives the yaw error; Eq. (32) determines the pitch error; and Eq. (33) estimates time to impact (t_{go}).

$$\psi_{err} = \frac{\vec{LOS}_{NED} - \vec{v_{NED}}\ t_{go}}{t_{go}^2} \cdot [0\ 0\ 1] \tag{31}$$

$$\theta_{err} = \frac{\vec{LOS}_{NED} - \vec{v_{NED}}\ t_{go}}{t_{go}^2} \cdot [-1\ 0\ 0] \tag{32}$$

$$t_{go} = \frac{1}{g}\vec{v_{NED}} \cdot [0\ 1\ 0] + \frac{1}{g}\sqrt{\left(\vec{v_{NED}} \cdot [0\ 1\ 0]\right)^2 + 2g\ \vec{LOS}_{NED} \cdot [0\ 1\ 0]} \tag{33}$$

Next, the utilized control law is presented, which gets as result two control parameters to be employed by the actuation system. Control is handled by a double loop feedback system, which uses accelerations and angular speed in body axes. The inner loop is only used as a system of stability augmentation. The two control parameters are the control angle for the rotating force (ϕ_c) and the module of the control force (τ_c). The control angle for the rotating force is defined in Eq. (34), taking pitch (θ_{err}) and yaw (ψ_{err}) errors as inputs. The module of the control force produced is also controlled. It is calculated in Eq. (35); note that this is done by processing the quadratic average of pitch and yaw errors. In these expressions $L1$ and $L2$ are experimental gains, K_i, K_d and K_p are the integral, derivative, and proportional constants of the controller, and K_{mod} is a constant to adjust the control force module.

$$\begin{aligned} \phi_c = {} & K_p\left[atan\frac{\theta_{err} - L1\theta}{L2(\psi_{err} - L1\psi)} - atan\frac{acc_{zb}}{acc_{yb}}\right] \\ & + K_i\int\left[atan\frac{\theta_{err} - L1\theta}{L2(\psi_{err} - L1\psi)} - atan\frac{acc_{zb}}{acc_{yb}}\right]dt \\ & + K_d\frac{d}{dt}\left[atan\frac{\theta_{err} - L1\theta}{L2(\psi_{err} - L1\psi)} - atan\frac{acc_{zb}}{acc_{yb}}\right] + atan\frac{\theta_{err} - L1\theta}{L2(\psi_{err} - L1\psi)} \end{aligned} \tag{34}$$

$$\tau_c = K_{mod}\sqrt{(\theta_{err} - L1\theta)^2 + \left(L2\left(\psi_{err} - L1\psi\right)\right)^2} \tag{35}$$

http://dx.doi.org/10.5772/intechopen.73511

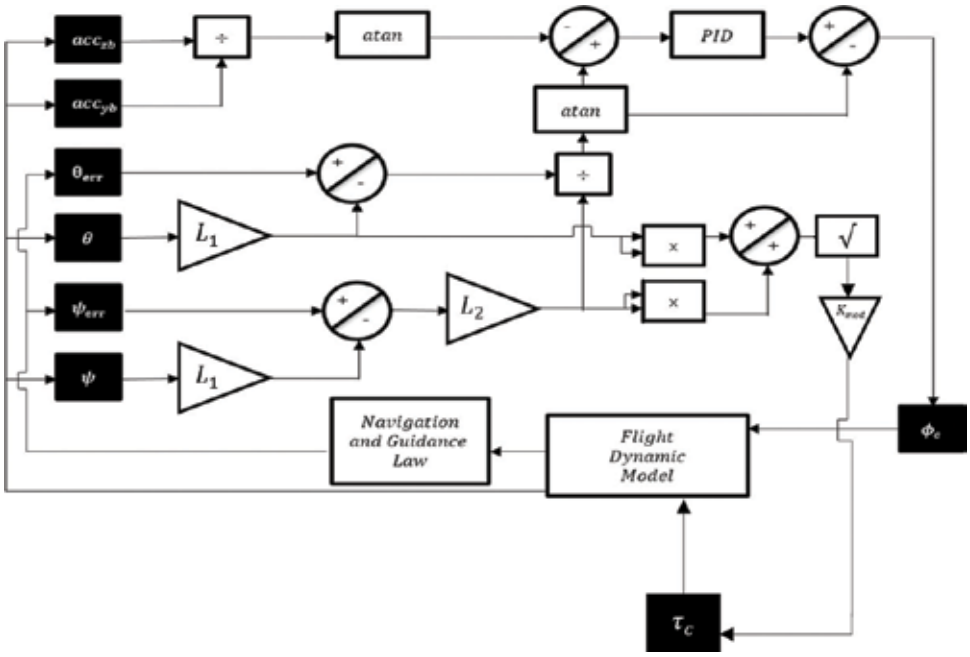

Figure 5. Control system scheme.

Figure 5 shows the logic of the controller. It has three fundamental sources of info: the acceleration of the rocket in body axis, communicated by its three components [acc_{xb}; acc_{yb}; acc_{zb}], the pitch and yaw errors and the measurements from gyros on each axis, [ϕ, θ, ψ].

Generally, the controller ascertains the required pointing angle of the aerodynamic force figuring the arc-tangent of the quotient of the pitch and yaw error. This gives an angle at which the aerodynamic force, in the $y_b - z_b$ plane, must point to reach the target. However, the gyroscopic effect due to the spinning part of the rocket makes the response difficult to govern, i.e., imposing a ϕ_c of 90° will not make the rocket to respond upwards. Subsequently, the acceleration of the rocket must be likewise measured, without representing gravity, so as to have the effect between the difference between the angle that forms the projection of the aerodynamic force in the $y_b - z_b$ plane with y_b and ϕ_c.

In order to translate these control parameters into fin deflections, i.e., δ_1, δ_2, δ_3 *and* δ_4 managed by two actuators, the relationships in (36) are applied.

$$\delta_1 = \delta_3 = \tau_c \sin\phi_c; \delta_2 = \delta_4 = \tau_c \cos\phi_c \tag{36}$$

5. Simulation results

MATLAB/Simulink R2016a on a desktop computer with a processor of 2.8 Ghz and 8 GB RAM was used. The rest of this section is divided in three different subsections. The first one presents the ballistic flights of the nominal trajectories to which the navigation, guidance and control algorithms developed will be applied. The second one describes the Monte Carlo

simulations to be performed. And the last one compares the results of ballistic flights, controlled flights with GNSS/Accelerometer guided trajectory and controlled flights with GNSS/Accelerometer/Photo-detector guidance.

5.1. Ballistic trajectories

To test the developed algorithms, three nominal trajectories will be employed, which differ in their launch or initial pitch angle: 20°, 30° and 45°. **Table 3** shows the characteristic parameters for these shots: initial pitch angle in the first column, initial lateral correction in the second one, and impact point in the last one. Initial lateral correction is performed in order to compensate Coriolis force and gyroscopic effects.

The results for the ballistic trajectories for the three proposed initial pitch angles are shown in **Figure 6**. It shows impact point dispersion patterns for each of the ballistic cases. Also, the circular error probable (CEP) may be observed for each of the initial shot pitch angle.

5.2. Monte Carlo simulations

Monte Carlo analysis is conducted to determine closed-loop performance across a full spectrum of uncertainty in initial conditions, sensor data acquisition, atmospheric conditions, and thrust properties. For atmospheric conditions variations in turbulence are considered using the specification MIL-F-8785C and the Dryden Wind turbulence model. Monte Carlo simulation distribution parameters are listed in the next **Table 4**. A set of 2000 shots is performed for each of the following combinations: ballistic shots, GNSS/Accelerometer assisted shots and GNSS/Accelerometer/Photo-Detector assisted shots. Initial shot angles of

Initial pitch angle (°)	Initial lateral correction (°)	Impact point (m)
20	0.1524	18790.38
30	0.1989	23007.26
45	0.3082	26979.00

Table 3. Nominal trajectories' parameters.

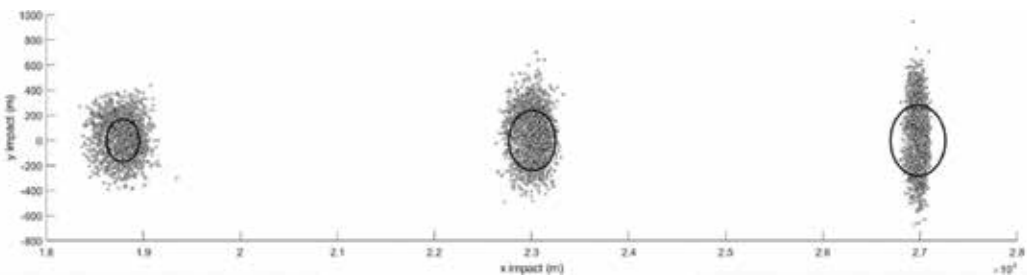

Figure 6. Ballistic shots for 20°, 30° and 45° initial pitch angles.

Parameter	Mean	Standard deviation
Initial φ	0°	20°
Initial pitch	Nominal (20°, 30°, 45°)	0.01°
Wind speed	10 m/s	5 m/s
Wind direction	0°	20°
Thrust at each time instant	T(t)	10 N
Initial azimuth deviation	Nominal lat. correction	0.01°

Table 4. Monte Carlo simulation parameters.

Parameter	C_1	C_2	K_i	K_p	K_d	K_{mod}	L_1	L_2
Value	−7.5°	−19 deg	1	0.3	0.025	0.08	0.01	1

Table 5. Values for the constants.

20°, 30° and 45° are performed. Note that a total of 18,000 simulation shots are performed at the end of simulation campaign.

5.3. Discussion

Values for navigation, guidance and control parameters defined on previous sections ($C1$, $C2$, K_i, K_p, K_d, K_{mod}, $L1$ and $L2$) are expressed in **Table 5**. These parameters where selected experimentally in the model in order to obtain stable flight conditions.

Figure 7 shows detailed information about comparisons between different approaches. On the top, middle and bottom rows, shots with launch angles of 20, 30 and 45° are presented, respectively. Furthermore, on the left column ballistic flights and GNSS/Accelerometer assisted flights are compared, on the middle column GNSS/Accelerometer and GNSS/Accelerometer/Photo-detector assisted flights, and finally on the right column ballistic flights and GNSS/Accelerometer/Photo-detector assisted flights are compared for each of the three-initial pitch or launch angles. Controlled flights exhibit tighter impact groupings, getting tighter for the GNSS/Accelerometer/Photo-detector controller. Spread in the impact distribution does remain in the guided flights with GNSS/Accelerometer controller due to the difficulties discussed before, especially on sensors subsection, where it is explained the typical error of GNSS sensors and its associated accuracy problems during terminal guidance phase.

The circular error probable (CEP) for each of the targets and for ballistic and controlled flights is shown in **Table 6**. The first column shows the initial pitch angle, the second one the CEP for the ballistic flight, the third one the CEP for the GNSS/Accelerometer Controlled Flight, and the last column the CEP for the GNSS/Accelerometer/Photo-detector Controlled Flight. The CEP for ballistic shots increases as initial pitch angle increases, while for controlled flights it remains stable, obtaining much better results for GNSS/Accelerometer/Photo-detector controller. Note that improvements or reductions on the CEP are above the 95%.

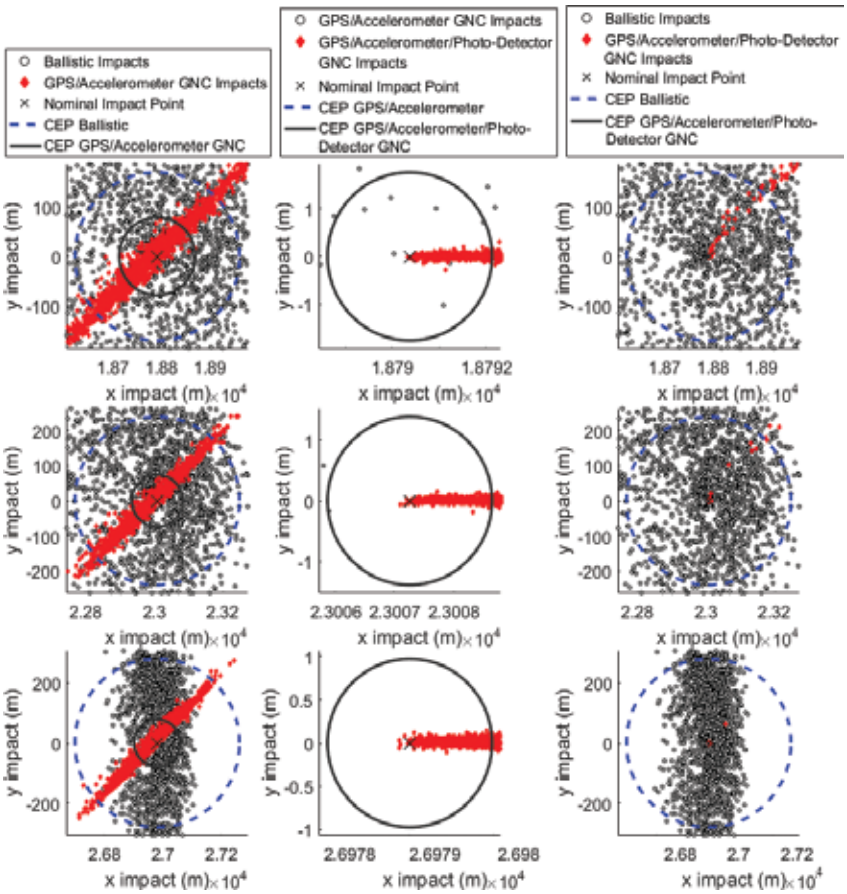

Figure 7. Detailed shots for different algorithms.

Initial pitch angle (°)	Ballistic flight (m)	GNSS/accelerometer controlled flight (m)	GNSS/accelerometer/photo-detector controlled flight (m)
20	169.34	78.27	1.75
30	239.37	73.80	1.39
45	281.59	78.84	0.97

Table 6. Circle error probable for the different cases.

6. Conclusions

A novel approach for navigation, guidance and control of high-rate spinning ballistic rockets, which is based on an innovative hybridization between GNSS/Accelerometer and semi-active laser quadrant photo-detector, has been developed.

Because ballistic rockets cannot be reused and high precision is of key importance, expensive equipment, e.g., sensors, has been traditionally employed. In this paper, however, it has been demonstrated that high precision may be obtained while using commercial off the shelf equipment, which is not usually highly precise.

Attitude determination is based on an algorithm which hybridizes data coming from multiple sensors and on a gravity vector estimator, avoiding the use of gyros. This approach is embedded in a two-phase guidance algorithm and a novel control technique for high-rate spinning rockets. The guidance algorithm is based on a modified proportional law while the control algorithm is based on a simple but effective and robust double-input double-output controller.

The proposed algorithms improve enormously accuracy by mixing those inaccurate signals in the terminal trajectory, with the signals of a precise semi-active laser quadrant detector, which is able to determine line of sight with high fidelity in body axes. Using the proposed hybridized algorithm during the last phases of flight, improves accuracy nearly to the ideal case as it was proved in simulations.

Author details

Raúl de Celis* and Luis Cadarso

*Address all correspondence to: raul.decelis@urjc.es

European Institute for Aviation Training and Accreditation (EIATA), Rey Juan Carlos University, Fuenlabrada, Madrid, Spain

References

[1] Celis RD, Cadarso L, Sánchez J. Guidance and control for high dynamic rotating artillery rockets. Aerospace Science and Technology. 2017;**64**:204-212. DOI:10.1016/j.ast.2017.01.026

[2] Hamilton R. Precision guided munitions and the new era of warfare. Air Power Studies Centre, Royal Australian Air. DOI: http://fas.org/man/dod-101/sys/smart/docs/paper53.htm

[3] Celis RD, Cadarso L. Improved algorithms for spot center determination in a semi-active laser quadrant detector for terminal guidance in artillery rockets. IEEE Transactions on Aerospace and Electronic Systems. 2016; Submitted, 2nd Round of Review

[4] Gurfil P. Robust guidance for electro-optical missiles. IEEE Transactions on Aerospace and Electronic Systems. 2003;**39**(2):450-461

[5] Manchester IR, Savkin AV, Faruqi FA. Method for optical-flow-based precision missile guidance. IEEE Transactions on Aerospace and Electronic Systems. 2008;**44**(3):835-851

[6] Waltz EL, Buede DM. Data fusion and decision support for command and control. IEEE Transactions on Systems, Man, and Cybernetics. 1986;**16**(6):865-879

[7] Holldack K, Peatman WB, Schroeter T. Vertical photon beam position measurement at bending magnets using lateral diodes. Review of Scientific Instruments. 1995;**66**(2):1889-1891

[8] Shen CB, Sun BG, Ma TJ, Lu P, Lin SF, Wang XH. Research of signal-processing methods in four-quadrant photodetector. In: ICEMS, editor. In Electrical Machines and Systems, IEEE International Conference on. 2008. pp. 917-919

[9] Maybeck PS, Herrera TD, Evans RJ. Target tracking using infrared measurements and laser illumination. IEEE Transactions on Aerospace and Electronic Systems. 1994;**30**(3): 758-768

[10] Ma DM, Shiau JK, Wang I, Lin YH, et al. Attitude determination using a mems-based flight information. Sensors. 2011;**12**(1):1-23

[11] Crassidis JL, Markley FL, Cheng Y. Survey of nonlinear attitude estimation methods. Journal of Guidance, Control, and Dynamics. 2007;**30**(1):12-28

[12] Gebre-Egziabher D, Elkaim GH, Powell J, Parkinson BW. A gyro-free quaternion-based attitude determination system suitable for implementation using low cost sensors. In: IEEE, editor. Position Location and Navigation Symposium. 2000. pp. 185-192

[13] Gebre-Egziabher D, Hayward RC, Powell JD. A low-cost gps/inertial attitude heading reference system (ahrs) for general aviation applications. In: IEEE, editor. Position Location and Navigation Symposium; IEEE. 1998. pp. 518-525

[14] Eure KW, Quach CC, Vazquez SL, Hogge EF, Hill BL. An Application of UAV Attitude Estimation Using a Low-Cost Inertial Navigation System. NASA; 2013;TM-2013-218144

[15] Henkel P, Iafrancesco M. Tightly coupled position and attitude determination with two low-cost gnss receivers. In: IEEE, editor. Wireless Communications Systems (ISWCS), 2014 11th International Symposium on; IEEE. 2014. pp. 895-900

[16] Springmann JC, Cutler JW. Flight results of a low-cost attitude determination system. Acta Astronautica. 2014;**99**:201-214

[17] Bevly DM, Rekow A, Parkinson B. Comparison of INS vs. carrier phase DGPS for attitude determination in the control of off-road vehicles. Navigation. 2000;**47**(4):257-266

[18] Cohen CE, Parkinson BW, McNally BD. Flight tests of attitude determination using GPS compared against an inertial navigation unit. Navigation. 1994;**41**(1):83-97

[19] Soken HE, Hajiyev C. Pico satellite attitude estimation via robust unscented Kalman filter in the presence of measurement faults. ISA Transactions. 2010;**49**(3):249-256

[20] Yun X, Bachmann ER, McGhee RB. Simplified quaternion-based algorithm for orientation estimation from earth gravity and magnetic field measurements. IEEE Transactions on Instrumentation and Measurement. 2008;**57**(3):638-650

[21] de Celis R, Cadarso L. Aircraft attitude determination algorithms employing gravity vector estimations and velocity measurements. In: Oleg Gusikhin, Kurosh Madani, editors. 14th International Conference on Informatics in Control, Automation and Robotics; 26–28 July 2017; Madrid. INSTICC; 2017. p. 377-385

Chapter 2

State-Space Modeling of a Rocket for Optimal Control System Design

Aliyu Bhar Kisabo and Aliyu Funmilayo Adebimpe

Additional information is available at the end of the chapter

http://dx.doi.org/10.5772/intechopen.82292

Abstract

This chapter is the first of two others that will follow (a three-chapter series). Here we present the derivation of the mathematical model for a rocket's autopilots in state space. The basic equations defining the airframe dynamics of a typical six degrees of freedom (6DoFs) are nonlinear and *coupled*. Separation of these nonlinear coupled dynamics is presented in this chapter to isolate the *lateral* dynamics from the *longitudinal* dynamics. Also, the need to determine aerodynamic coefficients and their derivative components is brought to light here. This is the crux of the equation. Methods of obtaining such coefficients and their derivatives in a sequential form are also put forward. After the aerodynamic coefficients and their derivatives are obtained, the next step is to trim and linearize the decoupled nonlinear 6DoFs. In a novel way, we presented the linearization of the decoupled 6DoF equations in a generalized form. This should provide a lucid and easy way to implement trim and linearization in a computer program. The longitudinal model of a rocket presented in this chapter will serve as the main mathematical model in two other chapters that follow in this book.

Keywords: rocket, six degrees of freedom (6DoFs), state space, trimming, linearization

1. Introduction

Over the years, a number of authors [1–4] have considered modeling rocket/missile dynamics for atmospheric flights. In the majority of the published work on these mathematical models, trimming and locally linearization are done without detailed explanation to the variables in the decoupled airframe dynamics. As such, the easy-to-write computer programs to facilitate this process numerically have been impeded.

With the advent of fast processors and numerical software like MATLAB®, Maple, Python, etc., it is now possible to take a complex nonlinear 6DoF equation like that of a rocket and run a program that can trim and linearize it with ease. This has made the field of control system design to grow at an exponential rate [5].

It is a known fact that the mathematical models are developed with their use in mind. This means before delving into the realization of a model, one should be well informed of the purpose for which that mathematical model will serve [6]. Especially, in the field of control system design, a mathematical model in transfer function might not be ideal for *optimal control* design. However, problem-solving environments (PSEs) like MATLAB®/Simulink come with built-in functions capable of transforming, say state-space model, to transfer functions. One should bear in mind that this is not without a "cost."

2. Mathematical model

A nontrivial part of any control problem is modeling the process. The objective is to obtain the simplest mathematical description that adequately predicts the response of the physical system to all inputs. For a rigid dynamic body, its motion can be described in translational, rotational, and angular inclinations at all times.

2.1. Translational motion

An accelerometer is often used to measure force on a dynamic body. For a rocket in motion, these forces [7] are represented as given in (1). Actually, this is a measure of the specific *force*, i.e., the nongravitational force per unit mass in *x*,*y*,*z*-directions, respectively. The specific force (also called the *g-force* or *mass-specific force*) has units of acceleration or ms^{-1}. So, it is not actually a force at all but a type of acceleration:

$$\begin{aligned}\dot{u} &= \frac{F_{A_{x_b}} + F_{P_{x_b}} + F_{g_{x_b}}}{m} - (qw - rv), m/s^2 \\ \dot{v} &= \frac{F_{A_{y_b}} + F_{P_{y_b}} + F_{g_{y_b}}}{m} - (ru - pw), m/s^2 \\ \dot{w} &= \frac{F_{A_{z_b}} + F_{P_{z_b}} + F_{g_{z_b}}}{m} - (pv - qu), m/s^2\end{aligned} \tag{1}$$

where

$F_{A_{xb}}, F_{A_{yb}}, F_{A_{zb}}$ = components of aerodynamic force vector F_A expressed in the body.

coordinate system, *N*.

$F_{g_{xb}}, F_{g_{yb}}, F_{g_{zb}}$ = components of gravitational force vector F_g expressed in body coordinate system, *N*.

$F_{p_{xb}}, F_{p_{yb}}, F_{p_{zb}}$ = components of thrust vector F_p expressed in the body coordinate system, *N*.

http://dx.doi.org/10.5772/intechopen.82292

m = instantaneous rocket mass, kg.

p, q, r = components of angular rate vector ω expressed in body coordinate system (roll, pitch, and yaw, respectively), rad/s.

u, v, w = components of absolute linear velocity vector V_x expressed in the body coordinate system, m/s.

$\dot{u}, \dot{v}, \dot{w}$ = components of linear acceleration expressed in body coordinate system, m/s^2.

The aerodynamic forces have the following components:

$$\begin{aligned} F_{A_{x_b}} &= -0.5\rho V_M^2 C_A S \\ F_{A_{y_b}} &= 0.5\rho V_M^2 C_{N_y} S \\ F_{A_{z_b}} &= 0.5\rho V_M^2 C_{N_z} S \end{aligned} \tag{2}$$

where

C_A = aerodynamic axial force coefficient, dimensionless.

C_N = aerodynamic normal force coefficient, dimensionless.

C_{Ny} = coefficient corresponding to component of normal force on yb-axis

$$C_{N_y} = C_N \frac{-v}{\sqrt{v^2 + w^2}}, \text{dimensionless}$$

C_{Nz} = coefficient corresponding to component of normal force on zb-axis

$$C_{N_z} = C_N \frac{1}{\sqrt{v^2 + w^2}}, \text{dimensionless}$$

S = aerodynamic reference area, m^2.

V_M = magnitude of velocity vector of the center of mass of the rocket, m/s.

ρ = atmospheric density, kg/m^3.

The propulsive forces in (1), as depicted in (**Figure 1**), are computed [8] as follows:

$$\begin{aligned} F_{p_{x_b}} &= F_p \cos\gamma_2 \cos\gamma_1, N \\ F_{p_{y_b}} &= F_p \cos\gamma_2 \sin\gamma_1, N \\ F_{p_{z_b}} &= -F_p \sin\gamma_2, N \end{aligned} \tag{3}$$

where

F_p = magnitude of total instantaneous thrust force vector, N.

F_{pxb}, F_{pyb}, F_{pzb} = components of thrust vector F_p expressed in body coordinate system, N.

γ_1 = angle measured from xb-axis to projection of thrust vector F_p on x_b y_b-plane, rad (deg).

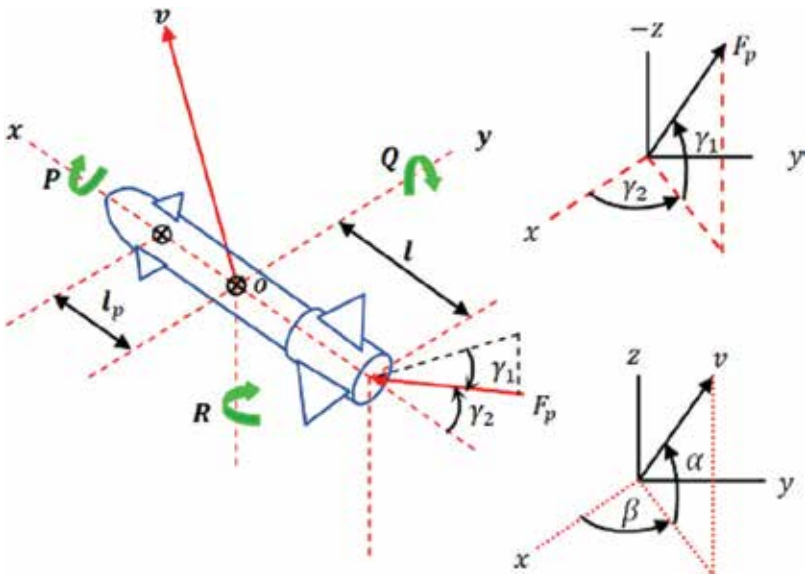

Figure 1. Propulsion force from the nozzle of a rocket.

γ_2 = angle measured from projection of thrust vector F_p on x_b y_b-plane to the thrust vector F_p, rad.

l_p = the distance from the aerodynamic center to center of mass, m.

l = the distance from the center of mass to nozzle, m.

If the rocket was designed for thrust vector control via gimbaling of the nozzle, F_p will be computed as given in (3). Here we assume that F_p is acting along the line of symmetry of the rocket because the nozzle is fixed (fin control). Hence, the magnitude of the thrust force F_p is calculated by

$$F_p = F_{pref} + \left(p_{ref} - p_a\right) A_e, N \tag{4}$$

where

A_e = rocket nozzle exit area, m^2.

F_{pref} = reference thrust force, N.

P_a = ambient atmospheric pressure, Pa.

P_{ref} = reference ambient pressure, Pa.

The gravitational forces in (1) are computed as follows:

$$\begin{aligned} F_{g_{x_e}} &= 0, N \\ F_{g_{y_e}} &= 0, N \\ F_{g_{z_e}} &= mg, N \end{aligned} \tag{5}$$

where

F_{gxe}, F_{gye}, F_{gze} = components of gravitational force vector F_g expressed in earth coordinate system, *N*.

g = acceleration due to gravity, m/s^2.

m = instantaneous mass of rocket, kg.

The dependence of the acceleration due to gravity on the altitude of the rocket is given by

$$g = g_0 \left[\frac{R_e^2}{(R_e + h)^2} \right], m/s^2 \tag{6}$$

where

g = acceleration due to gravity, m/s^2.

g_0 = acceleration due to gravity at earth surface (nominally *9.8* m/s^2), m/s^2.

h = altitude above sea level, m.

R_e = radius of the earth, m.

The gravitational force expressed in body coordinates is computed by multiplying (5) by matrix (7):

$$\left[\mathrm{T}_{e/\mathrm{b}}\right] = \begin{bmatrix} c\theta c\psi & s\phi s\theta c\psi - c\phi s\psi & c\phi s\theta c\psi + s\phi s\psi \\ c\theta s\psi & s\phi s\theta s\psi + c\phi c\psi & c\phi s\theta c\psi - s\phi c\psi \\ -s\theta & s\phi c\theta & c\phi c\theta \end{bmatrix}, \text{dimensionless} \tag{7}$$

where

c = cosine function *(cθ = cos θ)*, dimensionless.

s = *sine* function *(sθ = sin θ)*, dimensionless.

θ = the Euler angle of rotation in elevation (pitch) of body frame relative to earth frame, rad (deg).

φ = the Euler angle of rotation in roll of body frame relative to earth frame, rad (deg).

ψ = the Euler angle of rotation in azimuth (heading) of body frame relative to earth frame, rad (deg).

$[T_{e/b}]$ = transformation matrix from earth to body.

A vector v expressed in the body coordinate system can be transformed to the earth coordinate system by the matrix equation

$$v_e = \left[T_{e/b}\right] v_b \tag{8}$$

Hence, considering (5) we can write the following:

$$\begin{bmatrix} F_{g_{x_b}} \\ F_{g_{y_b}} \\ F_{g_{z_b}} \end{bmatrix} = \left[T_{b/e}\right] \begin{bmatrix} F_{g_{x_e}} \\ F_{g_{y_e}} \\ F_{g_{z_e}} \end{bmatrix}, N \tag{9}$$

The terms F_{gxb}, F_{gyb}, and F_{gzb} are the components of the gravitational force substituted into (1).

The **mass** in (1) is given below:

$$m = m_0 - \frac{1}{I_{sp}} \int_0^t F_{p_{ref}} dt, kg \tag{10}$$

where

F_{pref} = reference thrust force, N.

I_{sp} = specific impulse of propellant, Ns/kg.

m_0 = rocket mass at time zero (i.e., at the time of launch), kg.

t = simulated time, s.

2.2. Rotational motion

A gyroscope or gyro is a device that measures the angular acceleration or rotational motion of a dynamic body. On a rocket, this rotational motion can be described as

$$\begin{aligned} \dot{p} &= \frac{L_A + L_p - qr\left(I_z - I_y\right)}{I_x}, rad/s^2\left(\deg/s^2\right) \\ \dot{q} &= \frac{M_A + M_p - rp(I_x - I_z)}{I_y}, rad/s^2\left(\deg/s^2\right) \\ \dot{r} &= \frac{N_A + N_p - pq\left(I_y - I_x\right)}{I_z}, rad/s^2\left(\deg/s^2\right) \end{aligned} \tag{11}$$

where

L_A, M_A, N_A = components of aerodynamic moment vector M_A expressed in body coordinate system (roll, pitch, and yaw, respectively), Nm.

L_p, M_p, N_p = components of propulsion moment vector M_p expressed in body coordinate system (roll, pitch, and yaw, respectively), Nm.

I_x, I_y, I_z = components of inertia (diagonal elements of inertia matrix when products of inertia are zero), kg-m^2.

p, q, r (P, Q, R) = components of angular rate vector ω expressed in body coordinate system (roll, pitch, and yaw, respectively), rad/s (deg/s).

$\dot{p}, \dot{q}, \dot{r}$ = components of angular acceleration $\dot{\omega}$ expressed in body coordinate (roll, pitch, and yaw, respectively), rad/s^2 (deg/s^2).

$$\begin{aligned} L_A &= 0.5\rho V_M^2 C_l S d, Nm \\ M_A &= 0.5\rho V_M^2 C_m S d, Nm \\ N_A &= 0.5\rho V_M^2 C_n S d, Nm \end{aligned} \tag{12}$$

where

C_l = aerodynamic roll moment coefficient about center of mass, dimensionless.

C_m = aerodynamic pitch moment coefficient about center of mass, dimensionless.

C_n = aerodynamic yaw moment coefficient about center of mass, dimensionless.

d = aerodynamic reference length of body, m.

The aerodynamic moment coefficients are of the form

$$\begin{aligned} C_l &= C_{l_\delta}\delta_r + \frac{d}{2V_M}\left(C_{l_p}p\right) \\ C_m &= C_{m_{ref}} - C_{N_z}\frac{x_{cm} - x_{ref}}{d} + \frac{d}{2V_M}\left(C_{m_q} + C_{m_{\dot{\alpha}}}\right)q \text{ dimensionless} \\ C_n &= C_{n_{ref}} + C_{N_y}\frac{x_{cm} - x_{ref}}{d} + \frac{d}{2V_M}\left(C_{n_r} + C_{n_{\dot{\beta}}}\right)r \end{aligned} \tag{13}$$

where

C_{lp} = roll damping derivative relative to roll rate p, rad^{-1} (deg^{-1}).

$C_{l\delta}$ = slope of curve formed by roll moment coefficient C_1 versus control surface deflection, rad^{-1}(deg^{-1}).

C_{mref} = pitching moment coefficient about reference moment station, dimensionless.

C_{mq} = pitch damping derivatives relative to pitch rate q, rad^{-1}(deg^{-1}).

$C_{m_{\dot{\alpha}}}$ = pitch damping derivative relative to angle of attack rate $\dot{\alpha}$ (slope of curve formed by C_α verses α), rad^{-1} (deg^{-1}).

C_{Ny} = coefficient corresponding to component of normal force on yb-axis, dimensionless.

C_{Nz} = coefficient corresponding to component of normal force on zb-axis, dimensionless.

$C_{n_{\dot{r}}}$ = yaw damping derivative relative to yaw rate $\dot{r}$, rad^{-1}(deg^{-1}).

C_{nref} = yawing moment coefficient about reference moment station, dimensionless.

$C_{n_{\dot{\beta}}}$ = yaw damping derivative relative to angle of sideslip rate $\dot{\beta}$, rad-l (deg-1).

x_{cm} = instantaneous distance from rocket nose to center of mass, m.

x_{ref} = distance from rocket nose to reference moment station, m.

δ_r = effective control surface deflection causing rolling moment, rad (deg).

Considering that the rocket we intend to control is via fin deflection, fins on the rocket will be designated as shown in **Figure 2**.

Hence, the following moment coefficients are also given as

$$\begin{aligned} C_{m_{ref}} &= C_{m_\alpha}\alpha + C_{m_\delta}\delta_\eta \\ C_{n_{ref}} &= C_{n_\beta}\beta + C_{n_\delta}\delta_\zeta \end{aligned}, \text{ dimensionless} \tag{14}$$

where

C_{mref} = pitching moment coefficient about reference moment station (this is the static value normally measured in the wind tunnel.), dimensionless.

C_{m_α} = slope of curve formed by pitch moment coefficient. C_m versus angle of attack, α rad^{-1} (deg^{-1}) slope of tune formed.

C_{m_δ} = slope of tune formed by pitch moment coefficient C_m versus control surface deflection for pitch, δ_p rad^{-1} (deg^{-1}).

C_{n_β} = slope of curve formed by yawing moment coefficient C_n versus angle of sideslip β, rad^{-1} (deg^{-1}).

C_{n_δ} = slope of curve formed by yaw moment coefficient C_n versus effective control surface deflection for yaw, δ_y rad^{-1} (deg^{-1}).

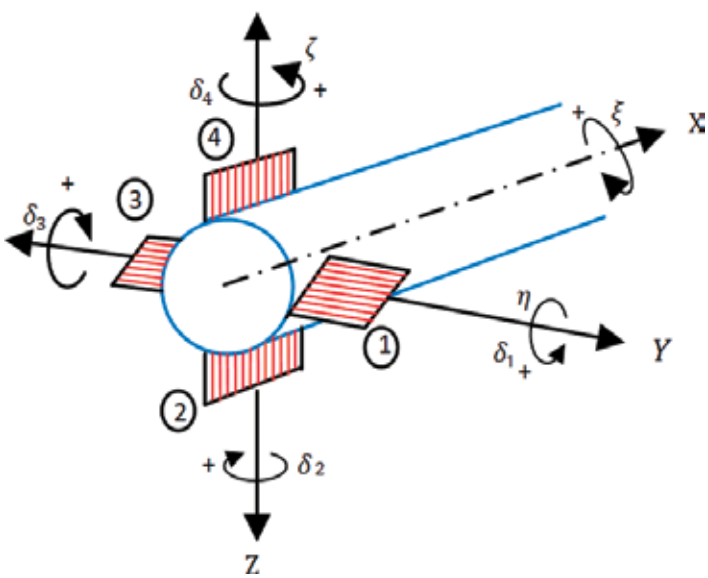

Figure 2. Fin control and designation for control.

http://dx.doi.org/10.5772/intechopen.82292

α = angle of attack, rad (deg).

β = angle of sideslip, rad (deg).

$\delta_\eta = \delta_1 = \delta_3$ effective control surface deflection causing pitching moment, rad (deg).

$\delta_\zeta = \delta_4 = \delta_2$ = effective control surface deflection causing yawing moment, rad (deg).

The angle of attack, angle of sideslip, and roll angle required for the realization of the aerodynamic coefficients are

$$\begin{aligned} \alpha &= Tan^{-1}\left(\frac{w}{u}\right) \text{or } \alpha_t = \tan^{-1}\left[\sqrt{\left(\frac{v^2+w^2}{u}\right)}\right] \\ \beta &= \sin^{-1}\left(\frac{v}{V_M}\right) \qquad \text{, rad (deg)} \\ \phi &= \tan^{-1}\left(\frac{v}{w}\right) \end{aligned} \tag{15}$$

where $\varnothing$ is aerodynamic roll angle, rad (deg), and α_t is the total angle of attack.

Table 1 gives a list of the aerodynamic coefficients that must be obtained for every rocket design before a model can be realized. There exist numerical and semi-numerical means of obtaining such coefficients. Examples of software that can do semiempirical computation of such coefficients and their derivatives are Missile Digital DATCOM® [9] and Flexible Structures Simulator (FSS) [10]. Finally, a wind tunnel test is expected to validate and update all coefficients and their derivatives before the system engineer delves in the control design.

The third and final component to fully describe the motion of a rocket is its angular inclination or attitude. We chose the Euler angles to describe the attitude of the rocket.

2.3. The Euler angles

Missile attitude is required for a number of simulation functions including the calculation of angle of attack, seeker gimbal angles, fuze look angles, and warhead spray pattern. In simulations with six degrees of freedom, the missile attitude is calculated directly by integrating the set of equations that define the Euler angle rates, i.e.,

$$\begin{aligned} \dot{\phi} &= p + \left(q\sin\phi + r\cos\phi\right)\tan\theta, rad/s(\deg/s) \\ \dot{\theta} &= q\cos\phi - r\sin\phi, rad/s(\deg/s) \\ \dot{\psi} &= \frac{q\sin\phi + r\cos\phi}{\cos\theta}, rad/s(\deg/s) \end{aligned} \tag{16}$$

where

θ = the Euler angle rotation in elevation (pitch angle), rad (deg).

ϕ = the Euler angle rotation in roll (roll angle), rad (deg).

$\dot{\psi}, \dot{\theta}, \dot{\phi}$ = rates of change of the Euler angles in heading, pitch, and roll, respectively, rad/s (deg/s).

P, q, r = components of angular rate vector w expressed in body coordinate system (roll, pitch, and yaw, respectively), rad/s.

The three heading angle of $\dot{\psi}, \dot{\theta}, \dot{\phi}$ can be measured directly using a magnetometer. Note also that the Euler angles in (16) can all be derived by integrating gyroscopic measurements. As such we might not need an instrument that will measure it directly. Nevertheless, a magnetometer can be added to the instrumentation on board to measure heading.

S/N	Variable	Description
1	C_N	Normal force coefficient (body axis)
2	C_L	Lift coefficient (wind axis)
3	C_M	Pitching moment coefficient (body axis)
4	X_{cp}	Center of pressure in calibers from moment reference center
5	C_A	Axial force coefficient (body axis)
6	C_D	Drag coefficient (wind axis)
7	C_Y	Side force coefficient (body axis)
8	C_n	Yawing moment coefficient (body axis)
9	C_l	Rolling moment coefficient (body axis)
10	$C_{N\alpha}$	Normal force coefficient derivative with angle of attack
11	$C_{M\alpha}$	Pitching moment coefficient derivative with angle of attack
12	$C_{Y\beta}$	Side force coefficient derivative with sideslip angle
13	$C_{n\beta}$	Yawing moment coefficient derivative with sideslip angle (body axis)
14	$C_{l\beta}$	Rolling moment coefficient derivative with sideslip angle (body axis)
15	C_{Mq}	Pitching moment coefficient derivative with pitch rate
16	C_{Nq}	Normal force coefficient derivative with pitch rate
17	C_{Aq}	Axial force coefficient derivative with pitch rate
18	$C_{M_{\dot{\alpha}}}$	Pitching moment derivative with rate of change of angle of attack
19	$C_{N_{\dot{\alpha}}}$	Normal force derivative with rate of change of angle of attack
20	C_{lp}	Rolling moment coefficient derivative with roll rate
21	C_{np}	Yawing moment coefficient derivative with roll rate
22	C_{Yp}	Side force coefficient derivative with roll rate
23	C_{lr}	Rolling moment coefficient derivative with yaw rate
24	C_{nr}	Yawing moment coefficient derivative with yaw rate
25	C_{Yr}	Side force coefficient derivative with yaw rate

Table 1. Aerodynamic coefficients as a function of angle of attack.

http://dx.doi.org/10.5772/intechopen.82292

Combining (1), (11), and (16) gives a complete six-degree-of-freedom equation of motion for a rocket in flight as shown in **Figure 3**. This could be written together as given in (17). In today's modern aerospace industry, a single device like the MPU6050, a MEM-based integrated chip, can be used to give numerical values for state variables of (17) on any dynamic body. For control system design, the rocket system as described in (17) needs to be separated into the two planes (decouple); these are called the lateral (*la*) and longitudinal (*lo*) dynamic equations of motion:

$$\begin{aligned}
\dot{u} &= \frac{F_{A_{x_b}} + F_{P_{x_b}} + F_{g_{x_b}}}{m} - (qw - rv), m/s^2 \\
\dot{v} &= \frac{F_{A_{y_b}} + F_{P_{y_b}} + F_{g_{y_b}}}{m} - (ru - pw), m/s^2 \\
\dot{w} &= \frac{F_{A_{z_b}} + F_{P_{z_b}} + F_{g_{z_b}}}{m} - (pv - qu), m/s^2 \\
\dot{p} &= \frac{L_A + L_p - qr(I_z - I_y)}{I_x}, rad/s^2(\deg/s^2) \\
\dot{q} &= \frac{M_A + M_p - rp(I_x - I_z)}{I_y}, rad/s^2(\deg/s^2) \\
\dot{r} &= \frac{N_A + N_p - pq(I_y - I_x)}{I_z}, rad/s^2(\deg/s^2)
\end{aligned} \tag{17}$$

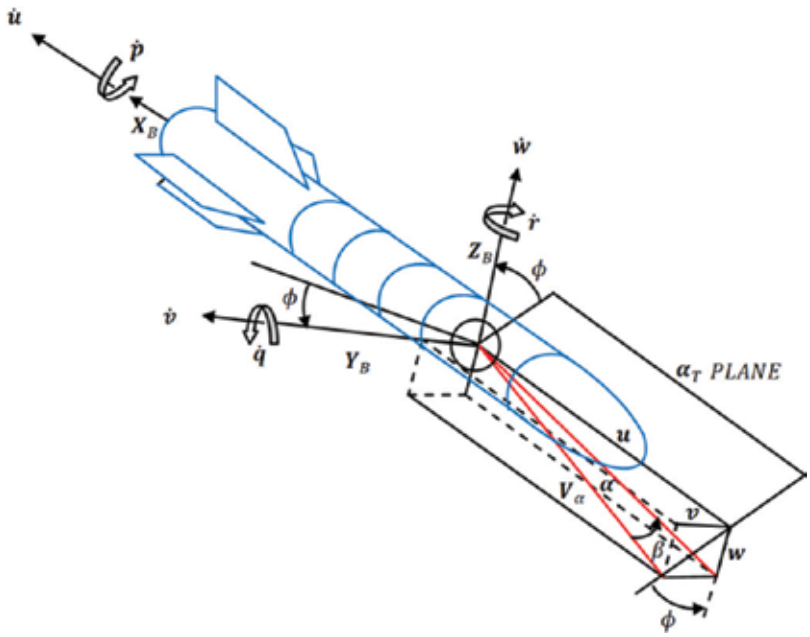

Figure 3. Six-degree-of-freedom motion of a rocket.

$$\dot{\phi} = p + \left(q \sin\phi + r \cos\phi \quad \tan\theta, rad/s(\deg/s)\right.$$

$$\dot{\theta} = q \cos\phi - r \sin\phi, rad/s(\deg/s)$$

$$\dot{\psi} = \frac{q \sin\phi + r \cos\phi}{\cos\theta}, rad/s(\deg/s)$$

Since the control system we intend to design is in a family of linear controllers and (17) is a nonlinear system of differential equations, trimming and linearization must be done.

2.4. Trimming

To trim or find equilibrium values requires a good knowledge of advance computational techniques. A trim point, also known as an equilibrium point, is a point in the parameter space of a dynamic system at which the system is in a steady state. The trim problem for a rocket can be described as finding a set of suitable input values to satisfy a set of conditions. Hence, a trim point involves setting of its controls that causes the rocket to fly straight and level in the longitudinal plane. The suitable input values are the control surface deflections, the thrust setting, and the rocket attitude [11]. The set of conditions are the rocket's accelerations. The variables associated with the trim problems can be divided into three categories:

- Objective variables
- Control variables
- Flight condition variables

The objective variables need to be driven toward the specified values, often zero (i.e., steady flight with zero sideslip). The objective parameters are combined in the objective vectors o_{la} (state vectors) and o_{lo}, for the lateral and longitudinal missile dynamics as

$$o_{la} = \left[\dot{v} \;\; \dot{p} \;\; \dot{r} \;\; \beta\right]^T. \tag{18}$$

$$o_{lo} = \left[\dot{u} \quad \dot{w} \quad \dot{q} \quad \alpha\right]^T. \tag{19}$$

The sideslip angle is also included, since for most cases, there are multiple solutions to the trim problem, each with a different sideslip angle. In the desired solution, the sideslip angle should be zero. In that case, the drag is at a minimum. The control parameters are adjusted in order to drive the objective parameters to their specified values. Together, they form the control vectors c_{la} and c_{lo}, described in (22). The control variables (input variables) describe the trimmed pilot control and the aircraft attitude:

$$c_{la} = \left[\delta_a \quad \delta_r \quad \phi \quad \psi\right]^T, \tag{20}$$

$$c_{lo} = \left[\delta_e \quad \tau \quad \theta\right]^T, \tag{21}$$

Finally, the 12 states of the 6DoF equation of motion must be initialized with the initial state conditions. In MATLAB®, the *trim* command is used to find equilibrium points. The object of

trimming is to bring the forces and moments acting on the rocket into a state of equilibrium. That is the condition when the axial, normal, and side forces and the roll, pitch, and yaw moments are all zero. Mathematically, trimming combines implicit and explicit Jacobian approaches. The Jacobian trim approach is the preferred method for rigid rocket. The Jacobian method is robust, since trim convergence is likely to occur even with rough estimates of the Jacobian and a rough first guess. Note that in general, any optimization routine could be used to solve the trim problem, as long as it is robust enough.

The Jacobian approach is based on the assumption that the change of the objective vector is linearly related to the change in the control input, which is shown in (22):

$$o_{i+1} - o_i = J_i[c_{i+1} - c_i]. \tag{22}$$

In (22), J_i is the Jacobian matrix evaluated near control input c_i. Its entries are first-order partial derivatives and represent the effect of changes in each control input on acceleration.

Note that changes in lateral plane induce changes in the longitudinal plane and vice versa; thus, we can write (23) the Jacobian for the lateral dynamics and (24) for the longitudinal or pitch dynamics:

$$J_i = \left.\frac{\partial o}{\partial c}\right|_{c_{i(la)}} = \begin{bmatrix} \frac{\partial \dot{u}}{\partial \delta_a} & \frac{\partial \dot{u}}{\partial \delta_r} & \frac{\partial \dot{u}}{\partial \phi} & \frac{\partial \dot{u}}{\partial \psi} \\ \frac{\partial \dot{v}}{\partial \delta_a} & \frac{\partial \dot{v}}{\partial \delta_r} & \frac{\partial \dot{v}}{\partial \phi} & \frac{\partial \dot{v}}{\partial \psi} \\ \frac{\partial \dot{w}}{\partial \delta_a} & \frac{\partial \dot{w}}{\partial \delta_r} & \frac{\partial \dot{w}}{\partial \phi} & \frac{\partial \dot{w}}{\partial \psi} \\ \frac{\partial \dot{p}}{\partial \delta_a} & \frac{\partial \dot{p}}{\partial \delta_r} & \frac{\partial \dot{p}}{\partial \phi} & \frac{\partial \dot{p}}{\partial \psi} \\ \frac{\partial \dot{q}}{\partial \delta_a} & \frac{\partial \dot{q}}{\partial \delta_r} & \frac{\partial \dot{q}}{\partial \phi} & \frac{\partial \dot{q}}{\partial \psi} \\ \frac{\partial \dot{r}}{\partial \delta_a} & \frac{\partial \dot{r}}{\partial \delta_r} & \frac{\partial \dot{r}}{\partial \phi} & \frac{\partial \dot{r}}{\partial \psi} \\ \frac{\partial \beta}{\partial \delta_a} & \frac{\partial \beta}{\partial \delta_r} & \frac{\partial \beta}{\partial \phi} & \frac{\partial \beta}{\partial \psi} \end{bmatrix}_{c_i}. \tag{23}$$

$$J_i = \left.\frac{\partial o}{\partial c}\right|_{c_{i(lo)}} = \begin{bmatrix} \frac{\partial \dot{u}}{\partial \delta_e} & \frac{\partial \dot{u}}{\partial \tau} & \frac{\partial \dot{u}}{\partial \theta} \\ \frac{\partial \dot{v}}{\partial \delta_e} & \frac{\partial \dot{v}}{\partial \tau} & \frac{\partial \dot{v}}{\partial \theta} \\ \frac{\partial \dot{w}}{\partial \delta_e} & \frac{\partial \dot{w}}{\partial \tau} & \frac{\partial \dot{w}}{\partial \theta} \\ \frac{\partial \dot{p}}{\partial \delta_e} & \frac{\partial \dot{p}}{\partial \tau} & \frac{\partial \dot{p}}{\partial \theta} \\ \frac{\partial \dot{q}}{\partial \delta_e} & \frac{\partial \dot{q}}{\partial \tau} & \frac{\partial \dot{q}}{\partial \theta} \\ \frac{\partial \dot{r}}{\partial \delta_e} & \frac{\partial \dot{r}}{\partial \tau} & \frac{\partial \dot{r}}{\partial \theta} \\ \frac{\partial \beta}{\partial \delta_e} & \frac{\partial \beta}{\partial \tau} & \frac{\partial \beta}{\partial \theta} \end{bmatrix}_{c_i}. \tag{24}$$

If the rocket is assumed to be at equilibrium, or trim condition, then the equations of motion can be linearized, and the 6DoF equation of motion can be resolved into their lateral and longitudinal states.

2.5. Linearization

The system of first-order nonlinear differential equations of the rocket as presented by (17) is said to be in state variable form if its mathematical model is described by a system of n first-order differential equations and an algebraic output equation as [12]:

$$\begin{aligned} \dot{x}_1 &= f_1(x_1, \ldots, x_n, u) \\ \dot{x}_2 &= f_2(x_1, \ldots, x_n, u) \\ &\ldots \\ \dot{x}_n &= f_n(x_1, \ldots, x_n, u) \\ y &= h(x_1, \ldots, x_n, u) \end{aligned} \tag{25}$$

The column vector $x = [x_1, \ldots x_n]^{\mathrm{T}}$ is called the *state* of the system. The scalars u and y are called the control input and the system output, respectively, denoting

$$f(x,u) = \begin{bmatrix} f_1(x_1, \ldots, x_n, u) \\ f_2(x_1, \ldots, x_n, u) \\ \vdots \\ f_n(x_1, \ldots, x_n, u) \end{bmatrix}. \tag{26}$$

Concisely, (26) is written as

$$\begin{aligned} \dot{x} &= f(x,u), \\ y &= h(x,u). \end{aligned} \tag{27}$$

where f and h are nonlinear functions of x and u; then, we say that the system is nonlinear. To linearize (26), we desire it to become

$$\begin{aligned} \dot{x} &= Ax + Bu \\ y &= Cx + Du. \end{aligned} \tag{28}$$

where A is n x n, B is n x 1, C is 1 x n, and D is all scalar in MATLAB®/Simulink.

One reason for approximating the nonlinear system (26) by a linear model of the form (28) is that, by so doing, one can apply rather simple and systematic linear control design techniques. Given the nonlinear system (26) and an equilibrium or trimmed points $x^* = [x_1^* \ldots x_n^*]^T$ obtained when $u = u^*$, noting that $\Delta x = x = x^*$, we define a coordinate transformation as follows:

$$\Delta x = \begin{bmatrix} \Delta x_1 \\ \vdots \\ \Delta x_n \end{bmatrix} = \begin{bmatrix} x_1 - x_1^* \\ \vdots \\ x_n - x_n^* \end{bmatrix}.$$

Further, denoting $\Delta u = u - u^*$, $\Delta y = y - h(x^*, u^*)$. The new coordinates $\Delta x, \Delta u,$ and Δy represent the variations of x, u, and y from their equilibrium values. You have to think of these as a

new state, new control input, and new output, respectively. The linearization of (26) is at x in which the equilibrium or trim [12] state is given by

$$\begin{aligned} \Delta\dot{x} &= A\Delta x + B\Delta u \\ \Delta y &= C\Delta x + D\Delta u, \end{aligned} \tag{29}$$

where

$$A = \left[\frac{\partial f}{\partial u}\right]_{x^*,u^*} = \begin{bmatrix} \frac{\partial f_1}{\partial x_1}\left(x_1^*,\ldots,x_n^*,u^*\right) & \cdots & \frac{\partial f_1}{\partial x_n}\left(x_1^*,\ldots,x_n^*,u^*\right) \\ \cdots & \cdots & \cdots \\ \frac{\partial f_n}{\partial x_1}\left(x_1^*,\ldots,x_n^*,u^*\right) & \cdots & \frac{\partial f_n}{\partial x_n}\left(x_1^*,\ldots,x_n^*,u^*\right) \end{bmatrix},$$

$$B = \left[\frac{\partial f}{\partial u}\right]_{x^*,u^*} = \begin{bmatrix} \frac{\partial f_1}{\partial u}\left(x_1^*,\ldots,x_n^*,u^*\right) \\ \vdots \\ \frac{\partial f_n}{\partial u}\left(x_1^*,\ldots,x_n^*,u^*\right) \end{bmatrix},$$

$$C = \left[\frac{\partial h}{\partial x}\right]_{x^*,u^*} = \begin{bmatrix} \frac{\partial h}{\partial x_1}\left(x_1^*,\ldots,x_n^*,u^*\right) & \cdots & \frac{\partial h}{\partial x_n}\left(x_1^*,\ldots,x_n^*,u^*\right) \end{bmatrix}, D = \left[\frac{\partial h}{\partial u}\right]_{x^*,u^*}.$$

Note that the matrices A, B, C, and D have constant coefficients in that all partial derivatives are evaluated at the numerical values $\left(x_1^*,\ldots,x_n^*,u^*\right)$.

2.6. Lateral dynamics of a rocket

Equations of motion in the lateral plane are described by (30). Note that (30) comprises of one of the force equations (F_y), one of the momentum equations (M_y), and two of the Euler angles from the 6DoF equations (decoupled from (17)):

$$\begin{aligned} \dot{v} &= \frac{F_{A_{y_b}} + F_{P_{y_b}} + F_{g_{y_b}}}{m} - (ru - pw), m/s^2 \\ \dot{p} &= \frac{L_A + L_p - qr\left(I_z - I_y\right)}{I_x}, rad/s^2\left(\deg/s^2\right) \\ \dot{r} &= \frac{N_A + N_p - pq\left(I_y - I_x\right)}{I_z}, rad/s^2\left(\deg/s^2\right) \\ \dot{\phi} &= p + \left(q\sin\phi + r\cos\phi\right)\tan\theta, rad/s(\deg/s) \\ \dot{\psi} &= \frac{q\sin\phi + r\cos\phi}{\cos\theta}, rad/s(\deg/s) \end{aligned} \tag{30}$$

For a completely computed aerodynamic coefficients and their derivatives, (30) can be expressed in state-space form [13] as

$$\begin{bmatrix} \dot{v} \\ \dot{p} \\ \dot{r} \\ \dot{\phi} \\ \dot{\psi} \end{bmatrix} = \begin{bmatrix} y_v & y_p & y_r & y_\phi & y_\psi \\ l_v & l_p & l_r & l_\phi & l_\psi \\ n_v & n_p & n_r & n_\phi & n_\psi \\ 0 & 1 & 0 & 0 & 0 \\ 0 & 0 & 1 & 0 & 0 \end{bmatrix} \begin{bmatrix} v \\ p \\ r \\ \phi \\ \psi \end{bmatrix} + \begin{bmatrix} y_\xi & y_\zeta \\ l_\xi & l_\zeta \\ n_\xi & n_\zeta \\ 0 & 0 \\ 0 & 0 \end{bmatrix} \begin{bmatrix} \xi \\ \zeta \end{bmatrix}. \tag{31}$$

All the variables in A matrix of (31) are the lateral dimensionless aerodynamic stability derivatives with respect to the system state vectors. The variables in B matrix of (31) are the lateral dimensionless aerodynamic control derivatives with respect to the designated control surfaces.

2.7. Longitudinal dynamics of a rocket

The longitudinal dynamics in motion is also called the pitch plane. Equations describing the motion of a rocket in this plane can be described as given in (32). Note that (32) comprises two of the force equations (F_x and F_z), two of the momentum equations (M_x and M_z), and two of the Euler angles from the 6DoF equations as given in (17):

$$\begin{aligned} \dot{u} &= \frac{F_{A_{x_b}} + F_{P_{x_b}} + F_{g_{x_b}}}{m} - (qw - rv), m/s^2 \\ \dot{w} &= \frac{F_{A_{z_b}} + F_{P_{z_b}} + F_{g_{z_b}}}{m} - (pv - qu), m/s^2 \\ \dot{q} &= \frac{M_A + M_p - rp(I_x - I_z)}{I_y}, rad/s^2 \left(\deg/s^2\right) \\ \dot{\theta} &= q\cos\phi - r\sin\phi, rad/s(\deg/s) \end{aligned} \tag{32}$$

Just as with (31), (32) can also be re-expressed in state space as

$$\begin{bmatrix} \dot{u} \\ \dot{w} \\ \dot{q} \\ \dot{\theta} \end{bmatrix} = \begin{bmatrix} x_u & x_w & x_q & x_\theta \\ z_u & z_w & z_q & z_\theta \\ m_u & m_w & m_q & m_\theta \\ 0 & 0 & 1 & 0 \end{bmatrix} \begin{bmatrix} u \\ w \\ q \\ \theta \end{bmatrix} + \begin{bmatrix} x_\eta & x_\tau \\ z_\eta & z_\tau \\ m_\eta & m_\tau \\ 0 & 0 \end{bmatrix} \begin{bmatrix} \eta \\ \tau \end{bmatrix} \tag{33}$$

In MATLAB® the *linmod* [14] command is used to invoke linearization. The assumption made for decoupling the linear model is that the cross-coupling effects between the two modes are negligible. These assumptions are:

- The rocket is designed with conventional control surfaces that do not give significant cross-coupling control between the lateral and longitudinal modes.
- The rocket is symmetrical about the xz plane in which the inertia cross-coupling in (xy and xz planes) result to cross-coupling between the lateral and longitudinal modes is minimum.

http://dx.doi.org/10.5772/intechopen.82292

It can be shown that a typical trimmed and linearized model of the pitch plane (longitudinal dynamics) for a rocket [15] is given as presented in (34). Notice that compared to (33), the velocity in x-direction is not included in (34). This is basically due to the fact that in this pitch plane, translational motion for a rocket is predominantly in the z-direction (velocity w):

$$\begin{bmatrix} \dot{\theta} \\ \dot{q} \\ \dot{w} \end{bmatrix} = \begin{bmatrix} 0 & 1 & 0 \\ 14.7805 & 0 & 0.01958 \\ -100.858 & 1 & -0.1256 \end{bmatrix} \begin{bmatrix} \theta \\ q \\ w \end{bmatrix} + \begin{bmatrix} 0 \\ 3.4858 \\ 20.42 \end{bmatrix} \delta_\eta + \begin{bmatrix} 0 \\ 14.7805 \\ -94.8557 \end{bmatrix} \alpha_w$$
$$y = \begin{bmatrix} 1 & 0 & 0 \end{bmatrix} \begin{bmatrix} \theta \\ q \\ w \end{bmatrix} \tag{34}$$

where

$$A = \begin{bmatrix} 0 & 1 & 0 \\ 14.7805 & 0 & 0.01958 \\ -100.858 & 1 & -0.1256 \end{bmatrix}, B = \begin{bmatrix} 0 \\ 3.4858 \\ 20.42 \end{bmatrix}, G = \begin{bmatrix} 0 \\ 14.7805 \\ -94.8557 \end{bmatrix} C = \begin{bmatrix} 1 & 0 & 0 \end{bmatrix}, D = 0.$$

3. Discussion of result

From (34), it can be seen that a three state variable models have been realized in state space. This implies that modern observer like the Kalman filter can be designed to estimate and predict the trajectory of such rocket dynamics. This mathematical model also can be used to design all the control algorithms that fall in the class of modern (optimal theory) control. Particularly, this model is important in the realization of the longitudinal autopilot system of a rocket.

4. Conclusion

Mathematical models are the bedrock of almost all scientific activities. Here we were able to define the nonlinear airframe dynamics of a rocket in 6DoF. We went further to decouple the 6DoF equations of motion for the rocket and presented forms in which the decoupled 6DoF is easily trimmed and linearized with a computer program like MATLAB®. The process presented here can be repeated for any size of the rocket and aircrafts/unmanned aerial vehicle (UAV). Note that if the aerospace vehicle being model is not a rocket, and a state-space model is needed, all the procedures outlined in this chapter will be the same. The only changes that will be accommodated will come from the numerical values of the aerodynamic coefficients and their derivatives.

Author details

Aliyu Bhar Kisabo* and Aliyu Funmilayo Adebimpe

*Address all correspondence to: aliyukisabo@yahoo.com

Centre for Space Transport and Propulsion (CSTP), Epe, Lagos-State, Nigeria

References

[1] Papp I. Missile mathematical model and system design. Atlantic Association for Research in the Mathematical Sciences. 2017;**16**(1):29-35

[2] Farhan AF. State space model for autopilot design of aerospace vehicles. In: Weapons Systems Division. Defence Science and Technology Organisation, DSTO-TR-1990; 2007

[3] Chelaru T-V, Barbu C. Mathematical model for sounding rockets, using attitude and rotation angles. International Journal of Applied Mathematics and Informatics. 2009; **3**(2):35-44

[4] Belega B-A. A mathematical model for computing the trajectory of rockets in a resistant medium taking into account the Earth's rotation. The system differential equations of the rocket trajectory. In: International Conference of Scientific Paper AFASES 2012; 2012

[5] Siouris GM. Missile Guidance and Control Systems. New York: Springer-Verlag, Inc; 2004. ISBN: 0-387-00726-1

[6] Blakelock JH. Automatic Control of Aircraft and Missiles. New York: John Wiley & Sons, Inc; 1965

[7] Missile Flight Simulation Part One Surface-to-Air Missiles, MIL-HDBK-1211(MI) 17 July 1995. In: Military Handbook. 1995

[8] Tewari A. Advance Control of Aircraft, Spacecraft and Rockets. United Kingdom: John Wiley & Sons, Ltd; 2011. ISBN 9781119971207

[9] MISSILE DATCOM User's Manual—2011 Revision. Christopher Rosema, Joshua Doyle, Lamar Auman, and Mark Underwood-U.S. Army Aviation & Missile Research, Development and Engineering Centre. William B. Blake-Control Design and Analysis Branch Control Sciences Division. AFRL-RB-WP-TR-2011-3071 (Supersedes 2008 Revision, AFRL-RB-WP-TR-2009-3015)

[10] User Manual. Software Package for Flexible Structures Simulation (FSS). International Institute for Advanced Aerospace Technologies of St. Petersburg State University of Aerospace Instrumentation. Performed according to the Contract No. I-011-2012; 2013

[11] Yang WY et al. Applied Numerical Methods Using MATLAB. Hoboken, New Jersey: John Wiley & Sons, Inc; 2005. ISBN 0-471-69833-4

[12] White RE. Computational Mathematics: Models, Methods, and Analysis with MATLAB and MPI. New York: Chaoman & Hall/CRC; 2004. ISBN: 1-58488-364-2

[13] Cook MV. Flight Dynamics Principles: A Linear Approach to Aircraft Stability and Control. 2nd ed. Burlington, USA: Butterworth-Heinemann. 2007. ISBN: 978-0-7506-6927-6

[14] User's Guide. Control System ToolboxTM. Revised for Version 9.7 (Release 2014a). The MathWorks, Inc; 2014

[15] Kisabo AB. Expendable Launch Vehicle Flight Control-Design & Simulation with Matlab/Simulink. Germany: Lambert Academic Publishing (LAP). ISBN: 978-3-8443-2729-8; 2011

Chapter 3

Discrete Element Modeling of a Projectile Impacting and Penetrating into Granular Systems

Waseem Ghazi Alshanti

Additional information is available at the end of the chapter

http://dx.doi.org/10.5772/intechopen.75550

Abstract

From theoretical standpoint, it is difficult to analytically build a general theory and physical principles that critically describe the mechanical behaviour of granular systems. There are many substantial gaps in understanding the mechanical principles that govern these particulate systems. In this chapter, based on a two-dimensional soft particle discrete element method (DEM), a numerical approach is developed to investigate the vertical penetration of a non-rotating and rotating projectile into a granular system. The model outcomes reveal that there is a linear proportion between the projectile's impact velocity and its penetration downward displacement. Moreover, depending on the rotation direction, there is a significant deviation of the x-coordinate of the final stopping point of a rotating projectile from that of its original impact point. For negative angular velocities, a deviation to the right occurs while a left deviation has been recorded for positive angular velocities.

Keywords: discrete element method, granular bed, rotating projectile, penetration, vertical impact

1. Introduction

A granular material is any collection of many macroscopic discrete solids, whose typical size ranges from micrometres to centimetres such as sand, coal, sugar, and rice. It is obvious that these materials cannot be characterised as gas, fluid, or solid. But, they have hybrid state between these three phases depending on the average energy of the individual grains inside the granular system. Piles, snow avalanches, and planetary rings (interstellar dust) are, respectively, considered as solid, fluid, and gas phases for granular materials [1].

In 1895, the German engineer H. A. Janssen [2] made the first attempt to study the dynamical behaviour of the granular systems under specific conditions. He investigated the pressure propagation along the wall of a silo filled with granular solids. Nevertheless, the science of granular materials has a standing research history that has deep roots in time. A general theory that governs the mechanical behaviour of the granular materials has not yet been established due to the complex behaviours of these particulate systems. Most of the successful theories in physics are based on forming a linear differential equation that contains physical quantities from the system under study. But, the knowledge needed to learn about the dynamics of granular materials requires the construction of nonlinear differential equation that can be solved only in rare cases. Therefore, efforts have mainly been made over the past 50 years to build theories that are based on linear differential equations to study these particulate systems. The absence of comprehensive physical principles of granular materials makes the physics of granular materials still not completely understood.

It is well known that the experiment studies of granular materials are limited, and are not capable of capturing most of the internal features of the granular dynamical systems governed by cohesion, friction, and collisions of the particles. Thus, the exploit of such investigations in granular material studies become ineffective and unreliable in most cases. Accordingly, modellers start to employ new techniques and approaches in their investigations relevant to the mechanics of granular materials. Away from experimental and physical approaches, new techniques have been proposed to investigate the behaviour of granular systems. These new techniques can be classified into three main categories:

- Theoretical-based techniques such as continuum mechanics methods and micromechanics analysis of particle collisions.
- Statistical averaging-based techniques such as the dense gas kinetic theory methods.
- Molecular dynamic simulation-based techniques such as the soft and hard particle discrete element methods (DEM), Monte Carlo techniques, and cellular automata techniques.

With the advance in computer technology, the molecular dynamic simulations or discrete approaches have recently been emerged. These methods have gained popularity and have been considered as powerful tools capable of handling the demands of the granular system research. In this chapter, based on the two-dimensional soft particle discrete element method (DEM), numerical simulations are carried out to study the dynamics of projectiles impacting and penetrating, vertically, beds of granular materials. First, we investigate the relationship between the penetration displacement of a projectile underneath a granular bed and its impact velocity. Then we investigate the effect of the rotation direction of a spinning projectile on its trajectory beneath the surface of a granular bed.

2. Development of discrete element model

Discrete element methods (DEMs) are numerical techniques capable of simulating the entire behaviour of systems of discrete interacting elements. Examples of discrete element simulations

http://dx.doi.org/10.5772/intechopen.75550

include hard and soft particle methods. The most common and flexible type of discrete element simulation methods is the soft particles models. They are able to model any kind of configuration, including static and dynamic situations [3]. Diluted and dense as well as long-lasting granular systems can be modelled through soft particle methods. The first soft particle contact model was carried out by Cundall and Strack [4]. The term soft particle refers to the fact that the particles are assumed to have collisions of (small) limited time and possibly experience elastic deformation. During the finite contact, the geometrical shape of the particle remains rigid, and the deformation is represented as small overlap at the surface which is taken into the account in the force model. The values of forces at the contact points are always varying as the particles are being deformed. At the same time, a particle may undergo multiple contacts with neighbouring particles and hence, numerous acting contact forces. Many types of forces can be simulated to act on a particle and various contact force models such as elastic and viscoelastic can be incorporated in this case. The general outline of any soft particle contact model is to determine, at one instant, each individual particle interchanges. Those interchanges are the surface (normal and frictional contact) forces with neighbouring particles or with the system boundaries. The normal and frictional interaction forces between particle-particle and particle-boundary are modelled by system of linear springs, shock absorbers (Dashpots), and sometime sliding elements are used. Due to the influence of these interaction forces and other forces like gravitational body force, the particles change their positions and velocities continuously throughout the simulation time. For each particle, the motion is governed by the principle of linear momentum and the principle of angular momentum. The resultant force acting on any individual particle can be calculated. Therefore, the acceleration of each individual particle at any simulation time step can be determined by using Newton's second law. Finally, the new velocity and position of the particle can be obtained by integrating the differential equation of its motion over small simulation step time.

2.1. Mathematical formulation set-up

For a typical simulation, each granular particle within the granular system bears two types of forces: contact forces and gravitational body force. Any contact force between two particles is decomposed into normal and tangential components. The normal contact force is modelled by a damped linear spring, while the tangential contact force by a linear spring in series with a frictional sliding element. The formula that determines the contact force of particle *i* and particle *j* is

$$\vec{F}_{ij}(t) = \vec{F}_{ij,\hat{n}}(t)\hat{n} + \vec{F}_{ij,\hat{s}}(t)\hat{s}\,, \tag{1}$$

where $\hat{n}$ and $\hat{s}$ are unit vectors in the normal and shear directions of the contact plane, $\vec{F}_{ij,\hat{n}}(t)$ and $\vec{F}_{ij,\hat{s}}(t)$ are, respectively, the magnitudes of the normal contact force and shear contact force, namely,

$$\vec{F}_{ij,\hat{n}}(t) = -k_{\hat{n}}\,\vec{\delta}_{ij,\hat{n}}(t)\,, \tag{2}$$

$$\vec{F}_{ij,\hat{s}}(t) = -\,\mathrm{sign}\left[\vec{\delta}_{ij,\hat{s}}(t)\right]\min\left\{k_{\hat{s}}\left|\vec{\delta}_{ij,\hat{s}}(t)\right|,\ \mu\vec{F}^{e}_{ij,\hat{n}}(t)\right\} \tag{3}$$

where k_n and k_s are, respectively, the particle-particle normal and tangential spring coefficients, $\vec{F}^{e}_{ij,n}(t)$ and μ are, respectively, the elastic contribution of the contact force between the particles i and j in the normal direction ($\hat{n}$ direction) and the friction coefficient of the granular particles, $\vec{\delta}_{ij,n}(t) \quad \left(R_i + R_j\right) - \vec{r}_i(t) - \vec{r}_j(t)\right|$ and $\vec{\delta}_{ij,s}(t) = \int_{t_0}^{t} \left(\dot{\vec{r}}_i(\eta) \quad \dot{\vec{r}}_j(\eta)\right) \hat{s}\, d\eta$ are, respectively, the normal compression and the tangential displacement between the particles i and j over the time step $\Delta t = t - t_0$, R_i R_i and R_j are the radii of the particles i and j. Under the contact forces and the gravitational body force, each particle has the following motion dynamic equations

$$m_i \frac{d^2\vec{r}_i}{dt^2} - \sum_{j=1}^{N_p} \vec{F}_{ij} + \vec{F}_{\omega}, \tag{4}$$

$$I_i \frac{d^2\vec{\theta}_i}{dt^2} = \sum_{j=1}^{N_p} \vec{M}_{ij} \mid \vec{M}_{ei}. \tag{5}$$

where m_i, I_i, $\vec{r}_i$, and $\dot{\vec{\theta}}_i$, are, respectively, the mass, rotational moment of inertia, position, and rotational vectors of the centre of particle i, $\vec{F}_{ij}$, $\vec{M}_{ij}$, $\vec{F}_{\omega}$, $\vec{M}_{ei}$, are, respectively, contact force and moment acting on particle i due to particle j and external forces and moment acting on particle i, N_p is the number of particles within the granular bed. Hence, $\forall i = 1, 2, 3, \mathrm{K}, N_p$, we have a system of first-order ordinary differential equations as follows:

$$\dot{\vec{r}}_i(t) \quad \vec{v}_i(t), \tag{6}$$

$$\dot{\vec{\theta}}_i(t) = \vec{\omega}_i(t), \tag{7}$$

$$\dot{\vec{v}}_i(t) \quad \frac{\sum_{j=1}^{N_p} \vec{F}_{ij} + \vec{F}_{ei}}{m_i}, \tag{8}$$

$$\dot{\vec{\omega}}_i(t) \quad \frac{\sum_{j=1}^{N_p} \vec{M}_{ij} + \vec{M}_{ei}}{I_i}. \tag{9}$$

Therefore, by numerical integration of Newton's equation of motion, the updated velocities and positions of all particles can be determined.

2.2. Numerical simulation structure

In general, numerical simulations are performed in two environments, namely, two dimensions and three dimensions. Most of the current numerical simulations are of two dimensions. They are popular due to the low computational cost by comparison with three-dimensional simulations. The behaviour of the entire granular system is also well observable. Furthermore,

most of the granular dynamical problems require the employ of two-dimensional simulations rather than three-dimensional simulations. For instance, two-dimensional simulations work well for problems such as the motion of a projectile penetrating into granular beds. Furthermore, in three-dimensional simulations, more contact points and extra spatial degrees of freedom have to be considered for each individual particle inside the system, and thus more computational power and memory storage are required.

When developing a two-dimensional discrete element code to imitate a particular granular problem, several aspects have to be taken in consideration. For instance, penetration of vertical projectile into granular beds is a granular dynamical problem in which most of particles in the system experience considerable multiple, long duration contacts. In this case, sufficient number of particles, in atypical simulation, needs to be taken into account, and the collisions and particles' overlaps should be easy to detect.

The current two-dimensional discrete element simulation code assumes the particles as a set of circular disks which are placed in the workplace at predetermined positions and velocities. The boundary conditions are assumed to be frictional. In the simulation workplace, any particle can be characterised through its radius R_i, mass m_i, initial moment I_i, position vector of the particle centre $\vec{r}_i$, translational (linear) velocity $\dot{\vec{r}}_i$, and the rotational (angular) velocity $\dot{\vec{\theta}}_i$, for $i = 1, 2, 3, \ldots, N_p$, where N_p is the total number of particles in the simulation. During the simulation, three types of forces are considered to act on the particles. These forces are gravitational body force and particle-particle and particle-boundary contact forces. A proper simulation time step was chosen so that short contacts are not missed. The interstitial fluid, cohesive, electromagnetic forces were neglected. Therefore, this model simulates granular material as dry particles in a blanked space and gravity field.

3. Vertical penetration displacement of a projectile and its impact velocity

In order to describe a relationship between the vertical penetration displacement of a projectile and its impact velocity, a series of numerical simulations were conducted. The methodology was to vary the impact velocity of the projectile and keep the other simulation parameters alike. The projectile impact velocities range from 5 to 65 m/s. The particle bed was considered to be mono-sized with particle diameter equal to 1.5 mm. **Figure 1** shows simulation sequential snapshots of the vertical penetration process. During the entire process, one can identify three distinct regimes, namely, impact, penetration, and collapse.

Figure 2(a) shows the relationship between the impact velocities and the penetration distances underneath the granular bed's surface for three different values of projectile's diameter. The observations reveal that the projectile's penetration downward displacement $\left(\vec{d}_{pen}\right)$ increases linearly with the projectile's impact velocity $\left(\vec{v}_{imp}\right)$.

To extrapolate a power law that governs the relationship between the projectile impact velocity and its penetration displacement, we convert the obtained data to log-log plots, as shown in

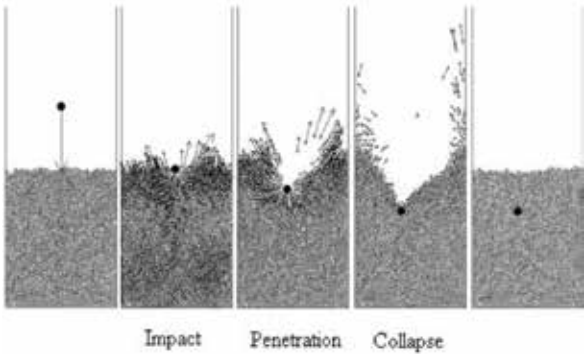

Figure 1. Simulation snapshots show the penetration process.

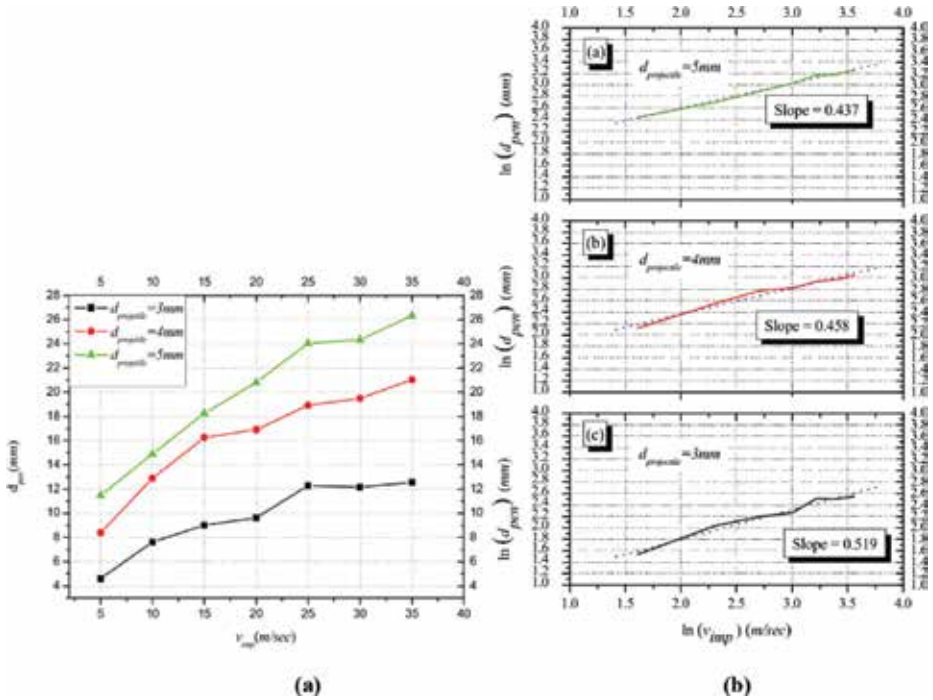

Figure 2. (a) Impact velocities versus penetration distances and (b) log-log plots of impact velocities versus penetration distances.

Figure 2(b). Obviously, the relationship between the penetration displacement and the impact velocity follows a power law of the form

$$\vec{d}_{penetration} \propto \left(\vec{v}_{impact}\right)^{\frac{1}{2}}. \tag{10}$$

The results from the simulation compare well with previous experimental results such as [5].

http://dx.doi.org/10.5772/intechopen.75550

4. Vertical penetration of rotating projectiles into granular beds

To analyse the relationship between the angular velocity of a rotating projectile on its orthogonal penetration displacement, a set of numerical simulations was carried out with different aspects. The method is to equip the rotating projectile with various angular impact velocities and keep all other simulation parameters identical including its impact velocity ($v_{imp} = 30$ m/sec). **Figure 3** shows snapshots of simulation of a rotating projectile orthogonally penetrating mono-sized granular bed with $d_s = 0.9$ mm.

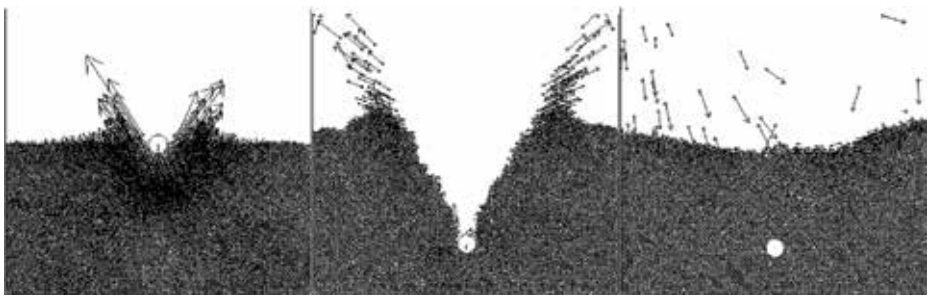

Figure 3. Simulation sequential snapshots of normal penetration of a rotating projectile.

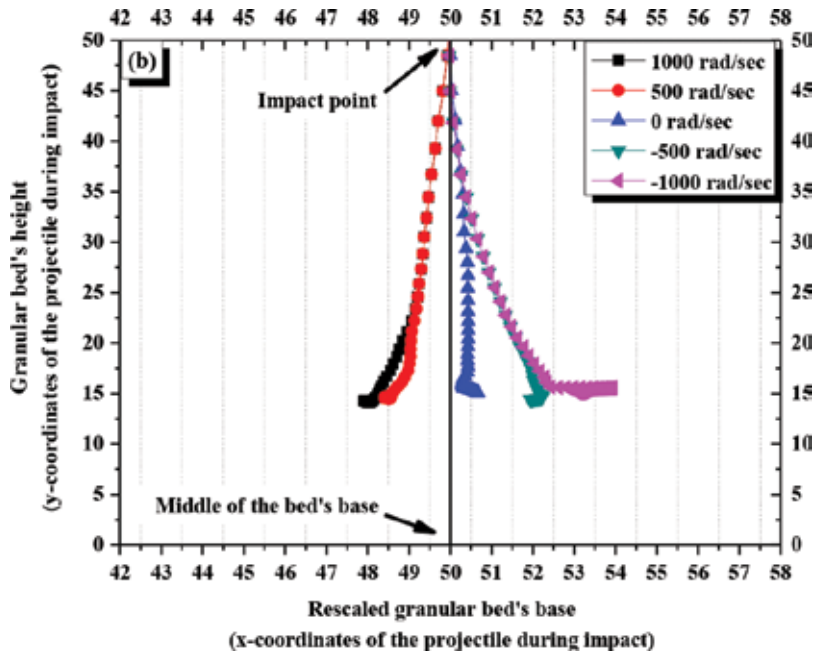

Figure 4. Deviation of the projectile's x-coordinate ultimate stopping point from that of its original impact point for various values of angular velocities. (a) Multisized particle bed. (b) Monosized particle bed.

For series of numerical simulations, a rotating projectile with fixed impact vertical velocity $\vec{v}_{imp} = 30$ m/sec is given various angular velocities, namely, $\vec{\omega} - 0, 500, 500, 1000,$ and -1000 rad/sec. Then the projectile strikes the middle of the free surface of the mono-sized granular bed. **Figure 4** shows the resultant trajectories of the rotating projectile underneath the granular bed's surface for each different value of the angular velocities. In general, the trajectory profile of the projectile exhibits two different regimes. For negative angular velocities, namely, $\omega = -500$ and -1000 rad/sec the penetration trajectories of the projectile under the granular bed exhibit negative exponential like traces. Conversely, positive exponential-like traces have been recorded for positive angular velocities, namely, $\omega = 500$ and 1000 rad/sec. The case when the projectile has no angular velocity, i.e. $\omega = 0$ rad/sec, can be considered as a turning value angular velocity between the two regimes. The resultant projectile's trajectory, in this case, locates in the middle of the two regimes' traces and the ultimate penetration point of the projectile is located, approximately, under its impact point. Moreover, it is found that, when the projectile comes to rest after achieving its maximum penetration depth, there is a considerable deviation for the x-coordinate of its ultimate stopping point from that of its original impact point. For negative angular velocities, namely, $\omega = -500$ and -1000 rad/sec, a deviation to the right under the original impact point occurs while a left deviation happens for positive angular velocities, namely, $\omega = 500$ and 1000 rad/sec.

5. Conclusion

This chapter focuses on the development of mathematical model based on the soft particle discrete element method for the study of two granular dynamical problems:

1. The relation between the vertical penetration displacement of projectile and its impact velocity. It has been found that the scaling law of the penetration displacement of a projectile with its impact velocity follows a power law of the form

$$\vec{d}_{penetration} \propto \left(\vec{v}_{impact}\right)^{\frac{1}{2}}. \tag{11}$$

2. We investigate the trajectories of a rotating projectile penetrating normally a granular system. Our numerical results show that the model is capable to simulate the normal penetration process for the various values of angular velocities. Moreover, it is found that the trajectory profile of the rotating projectile underneath the granular bed is affected the magnitude as well as the direction of its angular velocity. Depending on the rotation direction of the projectile, there is a relatively small change on the ultimate horizontal position of the projectile after penetration. For negative angular velocities, a right shift on the ultimate penetration point from the original projectile's impact point is observed. On the other hand, the projectile's eventual penetration point is located to the left of its original impact point for the positive angular velocities.

Author details

Waseem Ghazi Alshanti

Address all correspondence to: shantiw@ucj.edu.sa

General Studies Department, Jubail University College, Jubail, Saudi Arabia

References

[1] Goldhirsch I. Some open problems in granular media. Department of Fluid Mechanics and Heat Transfer. Faculty of Engineering. Tel-Aviv University. In: Subprogram on Uncertainty in Models of Granular Materials: *Sources and Consequences*; Kickoff Workshop; September 10-14, 2006

[2] Janssen HA. Versuche über getreidedruck in silozellen (investigation on the pressure of grain in silos). Zeitschrift des Vereines Deutscher Ingenieure. 1895;(39):1045

[3] Babic M, Shen HH, Shen HT. The stress tensor in granular shear flows of uniform, deformable disks at high solids concentrations. Journal of Fluid Mechanics. 1990;**219**:81-118

[4] Cundall PA, Strack DL. A discrete numerical model for granular assemblies. Geotechnique. 1979;**29**:47-65

[5] de Bruyn JR, Walsh AM. Penetration of spheres into loose granular media. Canadian Journal of Physics. 2004;**82**:439-446

Chapter 4

Analytical Prediction for Grain Burn Time and Burning Area Kinematics in a Solid Rocket Combustion Chamber

Charles A. Osheku, Oluleke O. Babayomi and Oluwaseyi T. Olawole

Additional information is available at the end of the chapter

http://dx.doi.org/10.5772/intechopen.82822

Abstract

This chapter proposes the application of Newtonian particle mechanics for the derivation of predictive equations for burn time, burning and unburnt area propagation for the case of a core propellant grain. The grain is considered to be inhibited in a solid rocket combustion chamber subject to the assumption that the flame propagation speed is constant for the particular solid fuel formulation and formation chemistry in any direction. Here, intricacies surrounding reaction chemistry and kinetic mechanisms are not of interest at the moment. Meanwhile, the physics derives from the assumption of a regressive solid fuel pyrolysis in a cylindrical combustion chamber subject to any theoretical or empirical burn rate characterization law. Essential parametric variables are expressed in terms of the propellant geometrical configuration at any instantaneous time. Profiles from simulation studies revealed the effect of modulating variables on the burning propagation arising from the kinematics and ordinary differential equations models. In the meantime, this mathematical exercise explored the tendency for a tie between essential kernels and matching polynomial approximations. In the limiting cases, closed form expressions are couched in terms of the propellant grain geometrical parameters. Notably, for the fuel burn time, a good agreement is observed for the theoretical and experimental results.

Keywords: solid rocket fuel, tubular rocket propellant, differential equations, burn rate

1. Introduction

Since the advent of rocketry, researchers have preoccupied their minds on the development of effective solid fuels for rocket and missile propulsion systems. A compendium of scholarly

works in propellant chemistry, aerothermodynamics, flight mechanics, guidance, navigation and control analyses abound in the literature. Solid fuels have been and are still in high demand for space mission and missile development planning. Notwithstanding the progresses in solid fuels physics and the advent of huge numerical studies, analytical conjectures are aptly handy for novel mechanical maneuvering of flight trajectories.

In the meantime, considerable progress was made by Tseng and Yang [1] in investigating the combustion of homogeneous propellants in realistic motor environments. The impact of the dispersion of instability signatures into the burning regions on combustion characteristics of the propellant was investigated. On this note, Roh et al. [2, 3] studied in details the relationship between acoustic oscillations and fast changing propellant burning in laminar flows. While the purpose of the study was to discover the underlying causes of perturbations, the inclusion of chemical characteristics provided a more robust mathematical solution. As a matter of scientific fact, same analysis was extended to incorporate the effect of turbulence [4, 5].

Likewise, a comprehensive numerical analysis was conducted in [6] to study the combustion of a double-base homogeneous propellant in a rocket motor. Emphasis was placed on the motor internal flow development and its influence on propellant combustion. The formulation was based on the Favre-averaged, filtered equations for the conservation laws and took into account finite-rate chemical kinetics and variable thermophysical properties. Nonetheless, results from the study showed that a smoother axial velocity gradient in conjunction with a vertical flow convection have a tendency to prevent or circumvent turbulence regime from deep penetration into the primary flame zone. These turbulence energy spectra have prompted dominant harmonics in a frequency range capable of triggering combustion instabilities. Meanwhile, a methodology for the solution of the internal physics of solid propellant rocket motors was described in [7]. The mathematical problem involved the simulation of a burning surface that dynamically changed the interface between the solid propellant and combustion gas phases.

An additional study in [8] showed how a technique was developed to obtain a burning rate data across a range of pressures from ambient to 345 MPa. It combines the uses of a low loading density combustion bomb with a high loading density closed bomb procedure. Furthermore, a series of nine ammonium perchlorate (AP)-based propellants were used to demonstrate the uses of the technique in comparison to the neat AP burning rate barrier. The effect of plasticizer, oxidizer particle size, catalyst and binder type was investigated. This necessitated an experimental program that was performed at the Space Propulsion Laboratory of the Politecnico di Milano. Notably, within the explored operating conditions and the associated uncertainty bands, a neutral trend for the solid fuel regression rate with increasing pressure was observed. The formulation tested was hydroxyl-terminated polybutadiene in gaseous oxygen at pressures ranging from 4 to 16 bars. A simplified analytical model, which retains the essential physics and accounts for pressure dependency, was developed for hybrid rockets in conjunction with the corresponding numerical simulation reported in [9]. However, the results of its simplified analytical model may not translate directly for use with solid rockets.

Nonetheless, the study reported in [10] was concerned with the prediction of the pressure history during the process of flame-spreading and combustion of solid propellant grains as

http://dx.doi.org/10.5772/intechopen.82822

would occur, for example, in a gun cartridge. Solution of the governing conservation equations for the two-phase media requires the use of empirical relations to account for the physical processes of momentum and energy interaction between the solid grains and hot propellant gas. The results indicated the significance of these interactions for the predictions of pressure and velocity fields. Of note too is the study in [11], where the combustion response of homogeneous and heterogeneous solid propellants to an imposed velocity field was certified to be a viable model for erosive burning mechanism. This leads to an imposed velocity field that has its roots in a multistate analysis of a solid rocket motor combustion processes. In the meantime, for homogeneous solid propellants, it has been shown that for certain realistic choices of the parameters, both positive and negative erosions simultaneously occurred. The underlying mechanism for erosive burning is tied flame stretching. On the hand, for heterogeneous solid propellants, any enhancements of the burn rate are tied to the cross flow velocity, propellant morphology and geometry and chamber pressure.

While information on thermodynamics is readily available in the literature, very clear analytical representation of the burn time of any geometry is rare. For now a gap exists for theoretical closed form results and experiential validation investigations. Theoretical equations that predict analytical burn time, thermal stresses buildup and how they are related ab initio to the solid propellant geometry are rare in literature. It is therefore necessary to have simplified analytical models that reduce computational time and laborious procedures and having reliance on numerically complicated methods such as computational fluid dynamics (CFD) or computational heat transfer (CHT) that would be utilized in the estimation of the burn time.

Traditionally, design and analysis of solid rocket motors have relied on empirical measurements to characterize fuel burn times and other propellant/motor performance quantities. This has been primarily because of the complexity of modeling adequately nontrivial fuel grain geometries and combustion processes. As overall system and vehicle performance models become more advanced and answer greater demands in terms of accuracy and detail, it is increasingly necessary to include more sophisticated models of subsystems such as the rocket motor. On the other hand, improved computational capabilities and better insights gleaned from experimental studies provide the means of achieving these better subsystem models. This chapter therefore covers a topic that is ripe for study and has potential to be of significant use to engineers who need to model burning performance for solid rocket propulsion. It may be of particular interest to those who lack the luxury of pursuing an experimental test campaign for a range of candidate fuel grain designs and parameters.

Several competing approaches exist in recent literature based on different focuses in terms of fundamental physics: analysis of radiation, temperature distribution and a range of coupled fluid flow/combustion approaches of varying complexity from 1D flow models to CFD. The method proposed in this chapter is beneficial in terms of its simplicity and consequently low computational cost, although its significant central assumptions mean that it can be applied only to certain cases (homogeneous propellants, tubular (regressive) grain designs and constant regression rates/steady-state operation). Its focus on only the kinematic viewpoint, without accounting for minutiae of chemical kinetic mechanisms, appears fairly unique among recent studies which have instead delved into the physically dominant processes at work.

Predicting grain burn time and burning area kinematics can be done in three ways: empirically (by experiment), analytically (using approximated mathematical models solved exactly) or numerically (by applying exact mathematical models solved approximately). The method proposed in the chapter falls into two parts: the first (burning time determination) combines analysis for modeling supplemented by empirical test data; the second part (burning/unburnt area determination) only covers an analytical approach without experimental or numerical validation [12].

The chapter is organized as follows: first is the derivation of the burn time equation, followed by an analysis of the effects of multiple points of ignition on the burn time. Analytical models are developed for unburnt and burning area propagation and discussion of results and the conclusion.

2. Derivation of burn time equation

In this section, the theory conjured is subject to the under listed assumptions, namely:

i. Propellant is homogeneous with uniform grain geometry.

ii. Any characterization burning rate law applies.

iii. After ignition, simultaneous burning process ensues along specified directions with constant regression rates. The alternative model, in [13], focuses on transient conditions and also describes erosive burning, which may be of interest in contrast to the erosive burning that can be accounted for in this chapter's proposed method based on kinematics. One evident advantage of this chapter's proposal is that it does not require any calculation of the fluid flow field, whereas even the alternative simplified 1D flow calculation proposed in [14] necessitates further computational expense, potentially.

iv. Inner tubular burning characterizes the process.

The typical tubular propellant and the combustion propagation are illustrated in **Figures 1** and **2**, while **Figure 3** gives an analytical model of the flame particle traversing in the designated axes.

In general, the average value of any time-dependent function $F_0(t)$ within the time interval t_H and t_G satisfies any of the equations:

$$F_{0(avg)} = \frac{1}{(t_G - t_H)} \int_{t_H}^{t_G} F_0(t)dt \tag{1}$$

$$\dot{F}_{0(avg)} = \frac{1}{(t_G - t_H)} \int_{t_H}^{t_G} \left(\frac{dF_0(t)}{dt}\right) dt \tag{2}$$

Given that, (W, L, A_s) are the web (thickness), length (L) and the sectorial area (A_s) of any typical tubular propellant grain, where the following holds:

http://dx.doi.org/10.5772/intechopen.82822

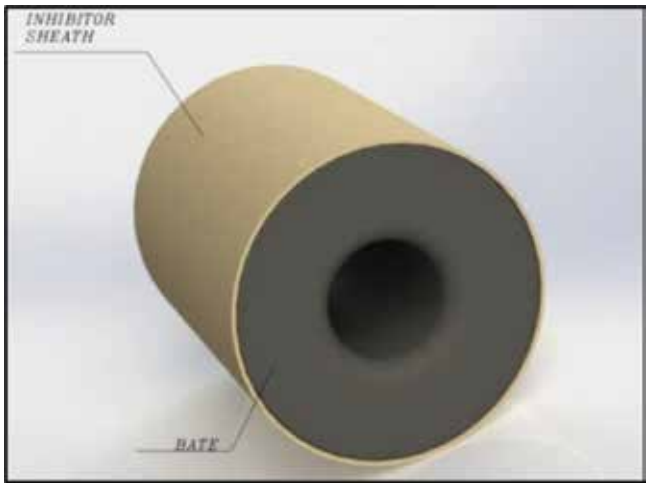

Figure 1. Typical tubular solid fuel.

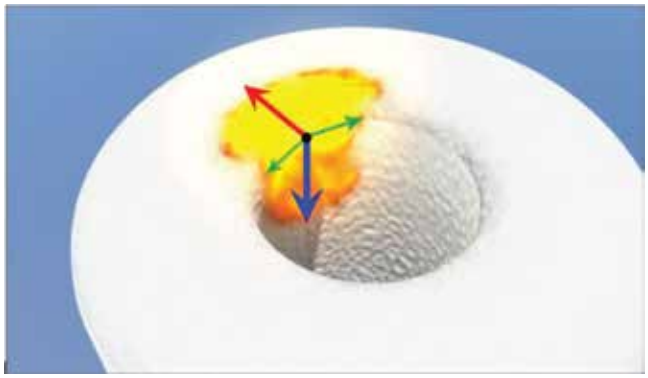

Figure 2. Illustration of different burning directions at point of ignition.

$$(W, L, A_s) \in F_o(t); \left(\dot{W}, \dot{L}, \dot{A}_s\right) \in \dot{F}_o(t)$$

Consequently, the total time required for the entire burning process specified in **Figure 4** must satisfy the following kinematic equation, namely:

$$t_{b(total)} = \frac{W}{\dot{W}} + \frac{L}{\dot{L}} + 2\frac{A_s}{\dot{A}_s} \tag{3}$$

From the point of ignition, as illustrated in **Figure 2**, the following further holds:

$$W = W_o - \dot{r}t_{b(web)}; L = L_o - \dot{r}t_{b(axial)}; d = \mathrm{d}_o + 2\dot{r}t_{b(radial)} \tag{4}$$

$$\|W\| = \left\|W_o - \dot{r}t_{b(web)}\right\|; \|L\| = \left\|L_o - \dot{r}t_{b(axial)}\right\|; \|d\| = \left\|d_o + 2\dot{r}t_{b(radial)}\right\| \tag{5}$$

in conjunction with a constant regression rate $(\dot{r})$. Under these circumstances, Eq. (3) now becomes

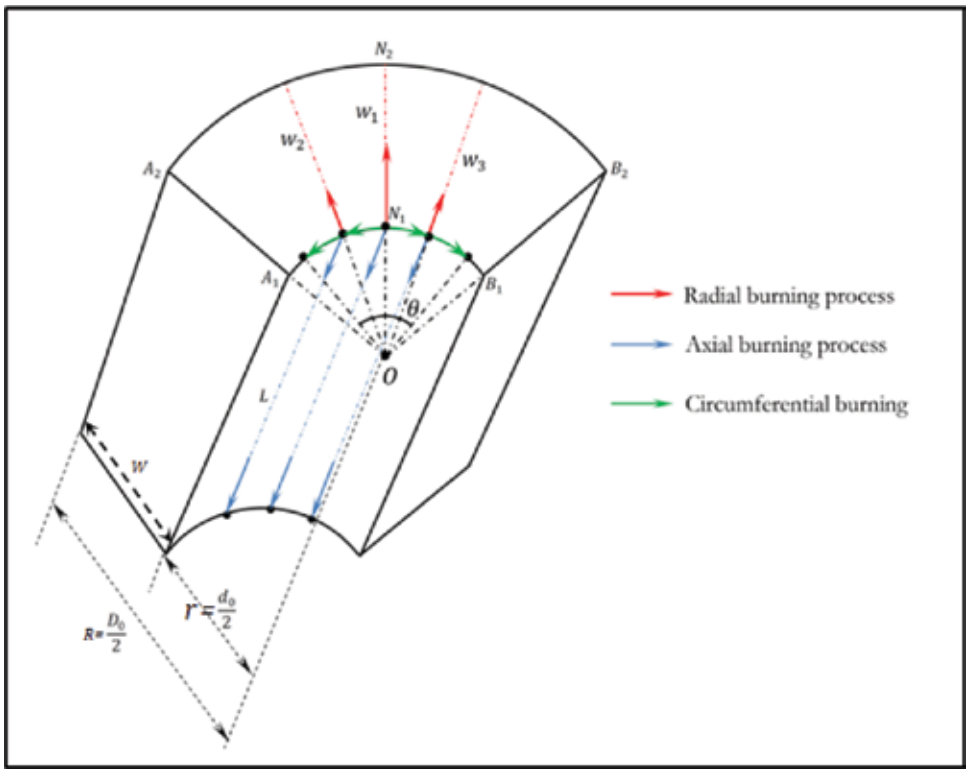

Figure 3. Regression along burn regions.

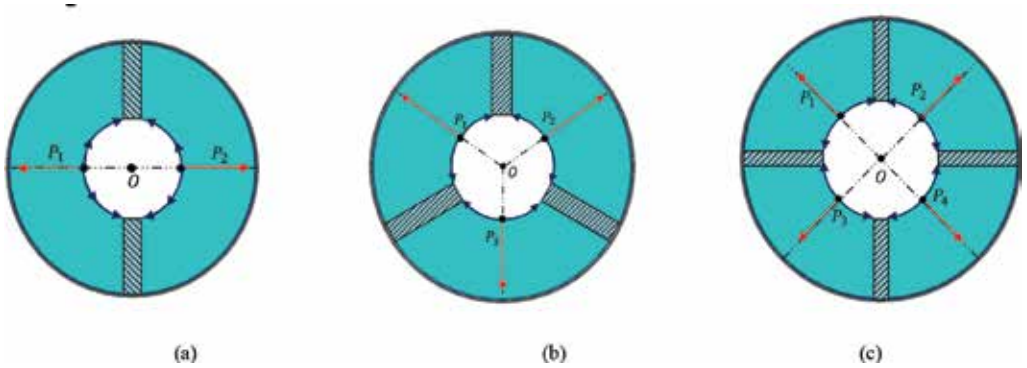

Figure 4. Illustrations of integral part of multiple ignition points on propellant grain. (a) 2-points, (b) 3-points, and (c) 4-points.

$$t_{b(total)} = \frac{W(1+2\eta)+\eta d}{\dot{r}} + 2\frac{A_s}{\dot{A}_s}; \quad \eta = \frac{L}{D} \tag{6}$$

From the sector burning area configuration, the following ensues, viz.:

$$A_S = \frac{1}{2}(R^2 - r^2)\theta = \frac{1}{2}W(W+d)\theta \quad ; \quad \dot{A}_S = \frac{1}{2}\left[\dot{\theta}W(W+d) - \theta d\dot{r}\right] \tag{7}$$

where θ is in radians, in conjunction with the following kinematics relation, viz.:

$$\dot{R} = 0; \dot{r} = \dot{r}_0; \forall\ \ddot{r} = 0 \tag{8}$$

leading to the total segmental burn time for the sectorial propellant grain as

$$\frac{A_s}{\dot{A}_s} = \frac{1}{\dot{r}} \quad \frac{(W+d)\theta}{4\eta\left(1+\frac{W}{d}\right) - \frac{\theta d}{W}} \tag{9}$$

From Eq. (9), Eq. (6) becomes

$$t_{b(total)} = \left(\frac{W(1+2\eta)+\eta d}{\dot{r}} + \frac{2}{\dot{r}}\left(\frac{(W+d)\theta}{4\eta\left(1+\frac{W}{d}\right) - \frac{\theta d}{W}}\right)\right) \quad 0 \le \theta \le 2\pi \tag{10}$$

In the meantime, Eq. (9) in terms of the instantaneous burning time t_ε takes the form, viz.

$$t_{b(total)} = \frac{1}{\dot{r}}\left\{\left((1+2\eta)W_0 + \eta d_0\right) - t_\varepsilon + 2\left(\frac{(W_0+d_0)\theta_0 + (W_0+d_0)\dot{\theta}t_\varepsilon + \theta_0\dot{r}t_\varepsilon + \dot{\theta}\dot{r}t_\varepsilon^2}{4\eta\left(1+\frac{W_0-\dot{r}t_\varepsilon}{d_0+2\dot{r}t_\varepsilon}\right) - \left(\frac{d_0\theta_0+\left(2\dot{r}\theta_0+\dot{\theta}d_0\right)t_\varepsilon+2r\dot{\theta}t_\varepsilon^2}{W_0-\dot{r}t_\varepsilon}\right)}\right)\right\} \tag{11}$$

arising from the following flame additional kinematics relations, namely, $\theta = \theta_0 + \dot{\theta}t_\varepsilon$, in conjunction with others specified in Eq. (5).

It is significant to examine the limiting case of Eq. (11) as $t_\varepsilon \to 0$, viz.:

$$\lim_{t_\varepsilon \to 0} t_{b(total)} = \lim_{t_\varepsilon \to 0} \frac{1}{\dot{r}}\left\{\left((1+2\eta)W_0 + \eta d_0\right) - t_\varepsilon + 2\left(\frac{(W_0+d_0)\theta_0 + (W_0+d_0)\dot{\theta}t_\varepsilon + \theta_0\dot{r}t_\varepsilon + \dot{\theta}\dot{r}t_\varepsilon^2}{4\eta\left(1+\frac{W_0-\dot{r}t_\varepsilon}{d_0+2\dot{r}t_\varepsilon}\right) - \left(\frac{d_0\theta_0+\left(2\dot{r}\theta_0+\dot{\theta}d_0\right)t_\varepsilon+2r\dot{\theta}t_\varepsilon^2}{W_0-\dot{r}t_\varepsilon}\right)}\right)\right\}$$

$$= \frac{1}{\dot{r}}\left\{\left[(1+2\eta_0)W_0 + \eta d_0\right] + \left(\frac{2(W_0+d_0)\theta_0}{4\eta\left(1+\frac{W_0}{d_0}\right) - \frac{d_0\theta_0}{W_0}}\right)\right\}; \forall\ \eta = \eta_0 - \frac{\dot{r}t_\varepsilon}{d_0+2W_0}; \eta_0 = \frac{L_0}{d_0+2W_0} \tag{12}$$

to indicate the closed form burn time prediction in terms of the tubular initial geometrical configuration.

In the meantime, Eqs. (10) and (11) are expressed further as

$$t_{b(total)} = \frac{d}{\dot{r}}\left\{\left[(1+2\eta)\chi + \eta\right] + \left(\frac{2(1+\chi)\overline{\theta}_0}{4\eta(1+\chi) - \frac{\overline{\theta}_0}{\chi}}\right)\right\};$$

$$\forall\ \chi = \frac{W}{d} = Lt_{t_{\varepsilon=0}}\left(\chi = \frac{W_0 - \dot{r}t_\varepsilon}{d_0 + 2\dot{r}t_\varepsilon}\right) = Lt_{t_{\varepsilon=0}}(\chi) = Lt_{t_{\varepsilon=0}} \quad \left(\frac{\chi_0 - \frac{\dot{r}t_\varepsilon}{d_0}}{1 + \frac{2\dot{r}t_\varepsilon}{d_0}}\right) \tag{13}$$

and

$$t_{b(total)} = \frac{d_0}{\dot{r}}\left\{\left[(1+2\eta)\chi_0 + \eta\right] + \left(\frac{2(1+\chi_0)\overline{\theta}_0}{4\eta(1+\chi_0) - \frac{\overline{\theta}_0}{\chi_0}}\right)\right\}\left(;\quad \chi_0 = \frac{W_0}{d_0}\quad ;\quad 0 \le \overline{\theta}_0 \le 2\pi\right) \tag{14}$$

When a propellant is completely burned out $\overline{\theta}_0 = 2\pi$, which corresponds to the case of 1-point ignition, to give the following expression, viz.

$$t_{b(total)} = \frac{d}{\dot{r}}\left\{\left[(1+2\eta)\chi + \eta\right] + \quad \frac{\pi(1+\chi)}{\eta(1+\chi) - \frac{\pi}{2\chi}}\right\}\left(\tag{15}$$

When $\overline{\theta}_0 = \pi$, which corresponds to the case of diametric ignition at two opposite sides to give the following expression, viz.

$$t_{b(total)} = \frac{d_0}{\dot{r}}\left\{\left[(1+2\eta)\chi_0 + \eta\right] + \quad \frac{\pi(1+\chi_0)}{\eta(1+\chi_0) - \frac{\pi}{2\chi_0}}\right\}\left(\tag{16}$$

This is to be further examined in the subsection for multiple ignition points.

2.1. Effect of multiple ignition points (N_p)

The effect of multiple ignition points is expected to create multiple sectorial flame propagation kinematics as illustrated in the figures below. Here, hatchings are indicating burning surfaces intersection arising from the sectorial kinematic propagation of the flame in line with the description in **Figures 2** and **3**.

Here, the matching kinematic equation takes the form

$$\frac{A_s}{\dot{A}_s}(N_p) = \frac{1}{\dot{r}}\left(\frac{(W+d)\theta_{(N_p)}}{4\eta\left(1+\frac{W}{d}\right) - \frac{\theta_{(N_p)}d}{W}}\right)\left(\forall\ \theta_{(N_p)} = \frac{2\pi}{N_p}\right. \tag{17}$$

It should be noted that propagations in radial and axial directions are expected to be rapid in consonance with the number of ignitions points. The overall effect therefore modulates Eq. (16) as

$$t_{b_{(N_p)}(total)} = \frac{d_0}{\dot{r}}\left\{\left[(1+2\eta)\frac{\chi_0}{N_p} + \frac{\eta}{N_p}\right]\left(+\left(\frac{\frac{\pi}{{N_p}^2}(1+\chi_0)}{\frac{\eta}{N_p}(1+\chi_0) - \frac{\pi}{2\chi_0{N_p}^2}}\right)\right\}\right($$

$$= \frac{d_0}{\dot{r}} \left\{ \left[\left(\frac{1+2\eta}{N_p} \right) \chi_0 + \frac{\eta}{N_p} \right] + \left(\frac{\pi \left(\frac{1+\chi_0}{{N_p}^2} \right)}{\eta \left(\frac{1+\chi_0}{N_p} \right) - \frac{\pi}{2\chi_0 {N_p}^2}} \right) \right\} = \frac{t_{b(total)}}{N_p} \tag{18}$$

3. Unburnt and burning area propagation

The plan and sectional views of the propellant grain geometries are illustrated in the figure below (**Figure 5**). These views are expected to provide illustrations on how the unburnt propellant grain area is derived.

From the figures above, the tubular grain's surface area is given by

$$A_{ub} = \frac{\pi}{2}\left(D^2 - d^2\right) + \pi d L \tag{19}$$

On introducing the aspect ratio, $\eta = \frac{L}{D}$, where $D = d_0 + 2W_0$, Eq. (19) becomes

$$A_{ub} = \pi\left[2W^2 + \eta d^2 + 2(1+\eta)Wd\right] \tag{20}$$

Using parts of Eq. (5), the above equation is further simplified as

$$A_{ub}(t_\varepsilon) = A_0 - \pi\left[B_1 \dot{r} t_\varepsilon + B_2 \dot{r}^2 t_\varepsilon^2 + B_3 \dot{r}^3 t_\varepsilon^3\right] \tag{21}$$

where t_ε is the instantaneous burning time.

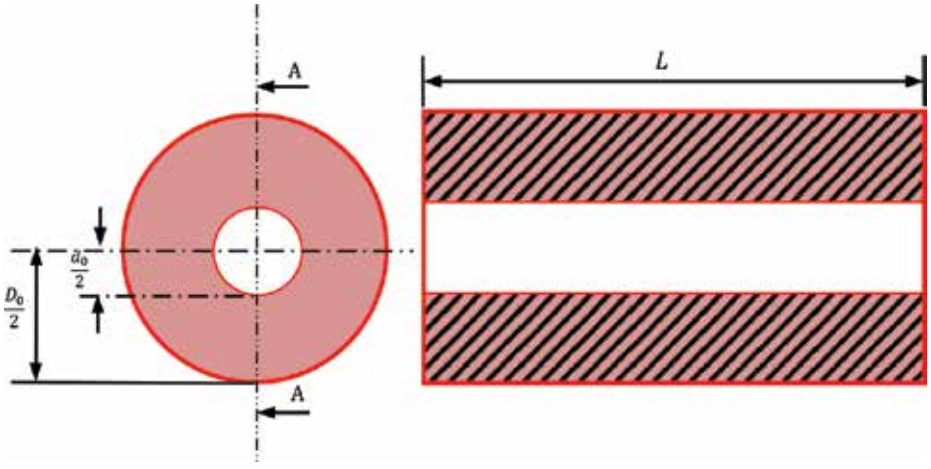

Figure 5. Tubular solid fuel geometrical parameters.

$$A_0 = \pi\left[2W_0^2 + 2(1+\eta_0)W_0 d_0 + \eta d_0^2\right]; \eta_0 = \frac{L_0}{d_0 + 2W_0};$$

$$B_1 = d_0\left[\frac{1}{\left(1+\frac{2W_0}{d_0}\right)} - 4\eta_0\right] + 2(1+\eta_0)(d_0 - W_0) + \frac{W_0}{\left(1+\frac{2W_0}{d_0}\right)}$$

$$B_2 = 2\left[(1-\eta_0) + \frac{2}{\left(1+\frac{2W_0}{d_0}\right)}\right]; B_3 = \frac{2}{\left(1+\frac{2W_0}{d_0}\right)}$$

Eq. (21) can be further written as

$$A_{ub}(t_\varepsilon) = A_{ub}(0) - A_b(t_\varepsilon) \tag{22}$$

where $A_{ub}(0) = A_0$, as illustrated below (**Figure 6**).

Above is the closed form expression for the instantaneous burning propellant area. Using Eq. (12), the kernel in the unburnt area $A_{ub}(t_\varepsilon)$ are rearranged to effect erosive regressive burning process, where

$$A_{ub}(t_\varepsilon) = A_0\left[1 - C_1\dot{r}t_\varepsilon - C_2\dot{r}^2t_\varepsilon^2 - C_3\dot{r}^3t_\varepsilon^3\right] \tag{23}$$

where $C_1 = \frac{B_1}{\Lambda_0}; C_2 = \frac{B_2}{\Lambda_0}; C_3 = \frac{B_3}{\Lambda_0}; \Lambda_0 = \left[2W_0^2 + 2(1+\eta_0)W_0 d_0 + \eta d_0^2\right]$

$$\Psi = \left[[(1+2\eta)W_0 + \eta d_0] + \left(\frac{2(W_0 + d_0)\overline{\theta}_0}{4\eta\left(1+\frac{W_0}{d_0}\right) - \frac{\overline{\theta}_0 d_0}{W_0}}\right)\right]; \forall\ 0 \le \overline{\theta}_0 \le 2\pi.$$

By introducing $X_0 = \frac{W_0}{d_0}$, Eq. (23) results to

$$A_{ub}(t_\varepsilon) = \overline{A}_0\left[1 - \overline{C}_1\tau - \overline{C}_2\tau^2 - \overline{C}_3\tau^3\right] \tag{24}$$

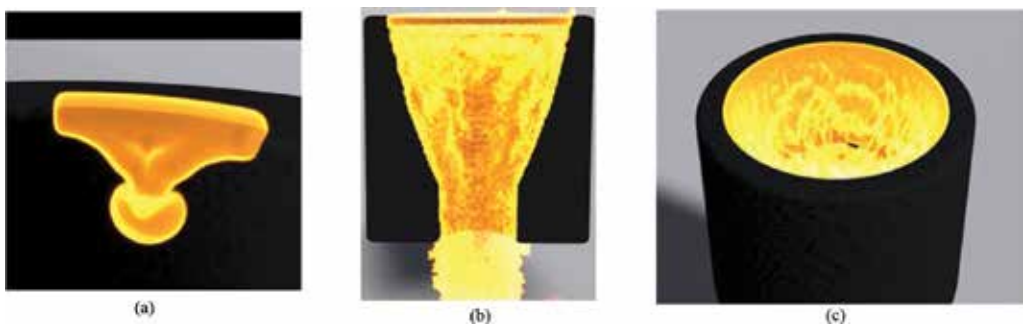

Figure 6. (a) Illustration of a point ignition at the commencement of burning propagation. (b) Cross section of burning propagation. (c) Complete burning process.

where $\overline{A}_0 = \pi d_0^2\left[2\chi_0^2 + 2(1+\eta_0)\chi_0 + \eta_0\right]; \overline{C}_1 = \frac{\overline{B}_1\overline{\Psi}}{\Lambda_0}; \overline{C}_2 = \frac{\overline{B}_2\overline{\Psi}^2}{\Lambda_0}; \overline{C}_3 = \frac{\overline{B}_3\overline{\Psi}^3}{\Lambda_0}$

where $\Lambda_0 = 2W_0^2 + 2(1+\eta_0)W_0 d_0 + \eta d_0^2; \overline{\overline{\Psi}} = [(1+2\eta)\chi_0 + \eta] + \left(\frac{\pi(1+\chi_0)}{\eta(1+\chi_0) - \frac{\pi}{2\chi_0}}\right)$

$$\text{Now at } t_\varepsilon = t_b \quad ; \quad A_{ub}(t_b) = A_0(1 - C_1 - C_2 - C_3) \tag{25}$$

From Eqs. (24) and (25), the non-dimensionalized unburnt propellant grain area is evaluated as

$$\frac{A_{ub}(t_\varepsilon)}{A_{ub}(t_b)} = A_{ub}(\tau) = \frac{\left[1 - \overline{C}_1\tau - \overline{C}_2\tau^2 - \overline{C}_3\tau^3\right]}{\left[1 - \overline{C}_1 - \overline{C}_2 - \overline{C}_3\right]} \tag{26}$$

Next, we return to the instantaneous burning area propagation via the following expression, namely:

$$A_b(t_\varepsilon) = \overline{A}_0\left[\overline{C}_1\tau + \overline{C}_2\tau^2 + \overline{C}_3\tau^3\right] \quad \forall \quad \tau = \frac{t_\varepsilon}{t_b} \tag{27}$$

$$\text{Now at } \; t_\varepsilon = t_b, A_b(t_b) = \overline{A}_0\left[\overline{C}_1 + \overline{C}_2 + \overline{C}_3\right] \tag{28}$$

From Eqs. (25) and (28), the non-dimensionalized form of the instantaneous burning area becomes

$$\frac{A_b(t_\varepsilon)}{A_b(t_b)} = \overline{A}_b(\tau) = \left(\frac{\overline{C}_1}{\overline{C}_1 + \overline{C}_2 + \overline{C}_3}\right)\tau + \left(\frac{\overline{C}_2}{\overline{C}_1 + \overline{C}_2 + \overline{C}_3}\right)\tau^2 + \left(\frac{\overline{C}_3}{\overline{C}_1 + \overline{C}_2 + \overline{C}_3}\right)\tau^3 \tag{29}$$

3.1. Effect of multiple ignition points

The effect of multiple ignition points (N_p) is expected to fractionalize the unburnt area time-dependent equations as follows, viz.:

$$A_{ub}(\tau) = \left(\frac{\frac{1}{N_p} - \overline{\overline{C}}_1\tau - \overline{\overline{C}}_2\tau^2 - \overline{\overline{C}}_3\tau^3}{\left(\frac{1}{N_p} - \overline{\overline{C}}_1 - \overline{\overline{C}}_2 - \overline{\overline{C}}_3\right)}\right); \forall\, \overline{\overline{C}}_1 = \overline{C}_1(N_p); \overline{\overline{C}}_2 = \overline{C}_2(N_p); \overline{\overline{C}}_3 = \overline{C}_3(N_p) \tag{30}$$

$$\overline{C}_1(N_p) = B_1\overline{\overline{\Psi}}(N_p); \overline{C}_2(N_p) = B_2\overline{\overline{\Psi}}^2(N_p); \overline{C}_3(N_p) = B_3\overline{\overline{\Psi}}^3(N_p)$$

$$\overline{\overline{\Psi}}(N_p) = \left[\left[\frac{(1+2\eta_0)\chi_0}{N_p} + \frac{\eta_0}{N_p}\right] + \left(\frac{\frac{\pi(1+\chi_0)}{N_p^2}}{\eta_0\left(\frac{1+\chi_0}{N_p}\right) - \frac{\pi}{2\chi_0 N_p^2}}\right)\right];$$

while for the burning area, the modification is

$$A_b(\tau) = \left(\frac{\overline{\overline{C}}_1\tau + \overline{\overline{C}}_2\tau^2 + \overline{\overline{C}}_3\tau^3}{\left(\overline{\overline{C}}_1 + \overline{\overline{C}}_2 + \overline{\overline{C}}_3\right)}\right) = \overline{\overline{B}}_1\tau + \overline{\overline{B}}_2\tau^2 + \overline{\overline{B}}_3\tau^3 \tag{31}$$

where $$\overline{\overline{B}}_1 = \left[\frac{1}{1+2\chi_0} - 4\eta_0 + 2(1+\eta_0)(1-\chi_0) + \frac{\chi_0}{1+2\chi_0}\right]\overline{\overline{\Psi}};$$

$$\overline{\overline{B}}_2 = 2\left[(1-\eta_0) + \frac{2}{1+2\chi_0}\right]\overline{\overline{\Psi}}^2; \quad \overline{\overline{B}}_3 = \frac{2}{1+2\chi_0}\overline{\overline{\Psi}}^3$$

For $\chi_0 = \frac{W_0}{d_0} \ll 1$, Eqs. (26) and (31) can be further written as

$$A_{ub}(\tau) = \left(\frac{1 - \overline{\overline{C}}_1\tau - \overline{\overline{C}}_2\tau^2 - \overline{\overline{C}}_3\tau^3}{1 - \overline{\overline{C}}_1 - \overline{\overline{C}}_2 - \overline{\overline{C}}_3}\right); \ \forall \ \overline{\overline{C}}_1 = \frac{\overline{\overline{B}}_1\overline{\overline{\Psi}}}{\Lambda_0}; \ \overline{\overline{C}}_2 = \frac{\overline{\overline{B}}_1\overline{\overline{\Psi}}^2}{\Lambda_0}; \ \overline{\overline{C}}_3 = \frac{\overline{\overline{B}}_3\overline{\overline{\Psi}}^3}{\Lambda_0} \tag{32}$$

$$\overline{\overline{B}}_1 \approx 3(1-2\eta_0) - (3+2\eta_0)\chi_0 - 2{\chi_0}^2 \, ; \overline{\overline{B}}_2 \approx 2(3-\eta_0-4\chi_0); \overline{\overline{B}}_3 \approx 2(1-2\chi_0)$$

$$A_b(\tau) = \overline{\overline{B}}_1\tau + \overline{\overline{B}}_2\tau^2 + \overline{\overline{B}}_3\tau^3 \tag{33}$$

Note that these closed form propagation profiles are kinematically derived. From the kernels, they exhibit third-order polynomial equations. To enable us study these profiles further, the following ordinary differential equation (ODE) modeling follows in the subsection.

4. Ordinary differential equation (ODE) modeling

As previously done, the modeling is taking off from the unburnt propagation problem. Given that $A_{ub}(t_\varepsilon)$ and $A_{ub}(t_\varepsilon + \Delta t_\varepsilon)$ are unburnt propellant grains at time (t_ε) and $(t_\varepsilon + \Delta t_\varepsilon)$, respectively, it is apparent that $A_{ub}(t_\varepsilon + \Delta t_\varepsilon) < A_{ub}(t_\varepsilon); \forall \, 0 < t_\varepsilon < (t_\varepsilon + \Delta t_\varepsilon)$.

Consequently,

$$\lim_{\Delta t_\varepsilon \to 0}\left(\frac{A_{ub}(t_\varepsilon + \Delta t_\varepsilon) - A_{ub}(t_\varepsilon)}{\Delta t_\varepsilon}\right) = \frac{-dA_{ub}(t)}{dt_\varepsilon} \tag{34}$$

leading to a simple linear ODE of the form

$$\frac{dA_{ub}(t_\varepsilon)}{dt_\varepsilon} = -\lambda_b A_{ub}(t_\varepsilon) \tag{35}$$

where $\lambda_b =$ propagation constant/s.

For Eq. (35) to be well posed, the following conditions are specified, viz.:

$$(i) \quad t_\varepsilon = 0; \ A_{ub}(0) = A_0$$

$$(ii) \quad t_\varepsilon = t_b; \ A_{ub}(t_b) = -A_0(C_1 + C_2 + C_3) \, \forall \, A_{ub}(t_b) + A_b(t_b) = 0 \tag{36}$$

In the meantime, the solution to Eq. (35) is given by

$$\therefore A_{ub}(t_\varepsilon) = A_{ub}(0)e^{-\lambda_b t_\varepsilon} \tag{37}$$

On imposing the conditions in Eq. (36), the following closed forms ensue, namely:

$$\therefore A_{ub}(t_\varepsilon) = A_{ub}(0)e^{-\lambda_b t_\varepsilon} \tag{38}$$

$$A_{ub}(t_\varepsilon) = A_0 e^{-\lambda_b t_\varepsilon} = A_0(C_1 + C_2) \tag{39}$$

Meanwhile, Eq. (38) satisfies the following form:

$$A_{ub}(t_\varepsilon) = A_0 e^{-\beta}\left(\frac{t_\varepsilon}{t_b}\right) = A_0 e^{-\beta\tau};\ \forall\ \beta = \ln(C_1 + C_2 + C_3);\ \tau = \frac{t_\varepsilon}{t_b} \tag{40}$$

to give a simple relation of the form

$$\overline{A}_{ub}(\tau) = e^{\beta(1-\tau)}\ \forall\ \beta = \ln\left(\overline{C}_1 + \overline{C}_2 + \overline{C}_3\right) \tag{41}$$

The foregoing represents the generalized unburnt propellant area propagation as a function of the dimensionless time(τ). To enable us generate semi-infinite polynomial models, the following series approximation suffices, namely:

$$\begin{aligned} e^{\beta(1-\tau)} &\approx \sum_{n=0}^{\infty}\frac{\beta^n(1-\tau)^n}{n!} \\ &\approx \left\{1 + \beta(1-\tau) + \frac{\beta^2(1-\tau)^2}{2!} + \frac{\beta^3(1-\tau)^3}{3!} + \frac{\beta^4(1-\tau)^4}{4!} + \ldots + \frac{\beta^n(1-\tau)^n}{n!} + R_N(\beta,\tau)\right\} \end{aligned} \tag{42}$$

From Eqs. (43) and (44), linear to infinite order profiles can be further deduced. A few illustrations follow, namely:

a. Linear unburnt area profile

$$A_{ub}^{(1)}(\tau) = \left((1+\beta) - \beta\tau\right) \tag{43}$$

b. Secondary degree unburnt area propagation profile (quadratic)

$$A_{ub}^{(2)}(\tau) = \left(\left(1 + \beta + \frac{\beta^2}{2}\right) - \left(\beta + \beta^2\right)\tau + \frac{\beta^2}{2}\tau^2\right) \tag{44}$$

c. Third-degree unburnt area propagation profile (cubic)

$$A_{ub}^{(3)}(\tau) = \left(\left(1 + \beta + \frac{\beta^2}{2} + \frac{\beta^3}{6}\right) - \left(\beta + \beta^2 + \frac{\beta^3}{2}\right)\tau + \left(\frac{\beta^2 + \beta^3}{2}\right)\tau^2 - \frac{\beta^3}{6}\tau^3\right) \tag{45}$$

d. Fourth-degree unburnt area propagation profile

$$A_{ub}^{(4)}(\tau) = \left(\left(1+\beta+\frac{\beta^2}{2}+\frac{\beta^3}{6}+\frac{\beta^4}{24}\right)-\left(\left(\beta+\beta^2+\frac{\beta^3}{2}-\frac{2\beta^4}{3}\right)\tau+\left(\left(\frac{\beta^2}{2}+\frac{\beta^3}{2}+\frac{\beta^4}{4}\right)\tau^2-\left(\frac{\beta^2}{6}+\frac{\beta^4}{6}\right)\tau^3+\left(\frac{\beta^4}{24}\right)\tau^4\right)\right)\right) \tag{46}$$

e. Nth degree unburnt area propagation profile

$$A_{ub}^{(Nth)}(\tau) = \left\{\left(1+\beta(1-\tau)+\frac{\beta^2(1-\tau)^2}{2!}+\frac{\beta^3(1-\tau)^3}{3!}+\frac{\beta^4(1-\tau)^4}{4!}+\cdots+\frac{\beta^N(1-\tau)^N}{N!}\right)\right\} \tag{47}$$

4.1. Burning propellant area modeling

The burning area $A_b(t_\varepsilon)$ can be deduced from the following equation, namely:

$$A_b(t_\varepsilon) = A_{ub}(0) - A_{ub}(t_\varepsilon) \tag{48}$$

resulting to an expression of the form

$$A_b(t_\varepsilon) = A_0\left(1-e^{-\lambda_b t_\varepsilon}\right) \tag{49}$$

subject to the following conditions, viz.:

$$\begin{aligned} &(i) \quad t_\varepsilon = 0; A_b(t_\varepsilon) = 0 \\ &(ii) \quad t_\varepsilon = t_b; A_b(t_b) = \overline{A}_0\left(\overline{C}_1+\overline{C}_2+\overline{C}_3\right) \end{aligned} \tag{50}$$

Note that Eq. (47) from the second part of Eq. (48) becomes

$$A_b(t_b) = A_0 \quad 1-e^{-\beta\left(\frac{t_\varepsilon}{t_b}\right)} \tag{51}$$

such that at

$$t_\varepsilon = t_b; A_b(t_b) = A_0\left(1-e^{-\beta}\right) \tag{52}$$

from which the following equation ensues:

$$\frac{A_b(t_\varepsilon)}{A_b(t_b)} = \overline{A}_b(\tau) = \left(\frac{1-e^{-\beta\tau}}{1-e^{-\beta}}\right) \tag{53}$$

upon using the following series approximations, viz.:

$$e^{-\beta\tau} \approx \sum_{n=0}^{\infty} \frac{(-\beta\tau)^n}{n!} \quad ; \quad e^{-\beta\tau} \approx \sum_{n=0}^{\infty} \frac{(-\beta)^n}{n!} \tag{54}$$

The following hold, namely:

$$(1 - e^{-\beta\tau}) \approx \quad 1 - \sum_{n=0}^{\infty} \frac{(-\beta\tau)^n}{n!}; \quad (1 - e^{-\beta}) \approx \quad 1 - \sum_{n=0}^{\infty} \frac{(-\beta)^n}{n!} \tag{55}$$

The use of the above equations transforms $\overline{A}_b(\tau)$ as

$$\overline{A}_b(\tau) = \frac{\sum_{N=0}^{\infty} \frac{(-1)^{N+1}\beta^N\tau^N}{N!}}{\sum_{N=1}^{\infty} \frac{(-1)^{N+1}\beta^N}{N!}} \tag{56}$$

The following approximated profiles can be generated, viz.:

(a) First-degree profile (linear)

$$\overline{A}_b^{(1)}(\tau) = \frac{\beta\tau}{\sum_{N=1}^{\infty} \frac{(-1)^{N+1}\beta^N}{N!}}$$

(b) Second-degree profile (quadratic)

$$\overline{A}_b^{(2)}(\tau) = \frac{\sum_{N=1}^{2} \frac{(-1)^{N+1}\beta^N\tau^N}{N!}}{\sum_{N=1}^{\infty} \frac{(-1)^{N+1}\beta^N}{N!}}$$

(c) Third-degree profile (cubic)

$$\overline{A}_b^{(3)}(\tau) = \frac{\sum_{N=1}^{3} \frac{(-1)^{N+1}\beta^N\tau^N}{N!}}{\sum_{N=1}^{\infty} \frac{(-1)^{N+1}\beta^N}{N!}}$$

(d) Fourth-degree profile (biquadratic)

$$\overline{A}_b^{(4)}(\tau) = \frac{\sum_{N=1}^{4} \frac{(-1)^{N+1}\beta^N\tau^N}{N!}}{\sum_{N=1}^{\infty} \frac{(-1)^{N+1}\beta^N}{N!}} \tag{57}$$

(e) Mth order degree profile

$$\overline{A}_b^{(M)}(\tau) = \frac{\sum_{N=1}^{M} \frac{(-1)^{N+1}\beta^N\tau^N}{N!}}{\sum_{N=1}^{\infty} \frac{(-1)^{N+1}\beta^N}{N!}}$$

5. Effect of multiple ignition points

The effects of multiple ignition points are accounted for in the following equations, viz. (unburnt area propagation):

$$\overline{A}_{ub}^{(N_p)}(\tau) = e^{\beta(N_p)(1-\tau)}; \overline{A}_b^{(N_p)}(\tau) = \quad \frac{1 - e^{-\beta(N_p)\tau}}{1 - e^{-\beta(N_p)}} \tag{58}$$

where $\beta(N_p) = \ln(\overline{C}_1(N_p) + \overline{C}_2(N_p) + \overline{C}_3(N_p))$

For the various associated polynomials, the matching kernel $\alpha(N_p)$ applies.

6. Discussion of results

Having shown the details of mathematical analyses, which leads to the derivation of closed form equations for both burning and unburnt propellant grain areas, subject to treating a flame particle arising from one to multiple ignition points theoretically using Newtonian mechanics, we shall now shift focus to discussing parametric modulations of these closed form equations. The interest here is to match theoretical simulated burn time results to those of conducted static burning tests of the propellant as demonstrated in **Figures 7** and **8**. Firstly, a cache of experimental set-ups for measuring the burn time are illustrated in **Figures 7** and **8**.

The static test rig holder as shown in **Figures 7** and **8** has an in-built sensor system which captures the burning propagation signature in the form of a digitized time signal that is fed into a transducer for a real-time display. A redundant system that has a stop-watch is also utilized for comparative purposes. After a number of static test experiments as demonstrated in **Figures 7** and **8**, the experimental results and theoretical comparisons are contained in **Tables 2** and **3**. The parameters of the solid propellant and combustion chamber are highlighted in **Tables 1** and **4**.

Meanwhile, the associated generalized chemical combustion equation for two classical composite formulations as illustrated below, namely,

Dextrose-based composite combustion equation:

$$6.09KNO_{3(s)} + 1.438C_6H_{12}O_{6(s)} + 4.11M_{g(s)} + 1.07C_{(s)} + 0.094Fe_2O_{3(s)} = 5.17CO_{(g)} + 4.94KOH_{(g)} + 4.74H_2O_{(g)} + 4.11CO_{2(g)} + 4.11MgO_{(s)} + 3.12N_{2(g)} + 1.42H_{2(g)} + 1.15K_{(g)}$$

Figure 7. Static test rigs with single motor.

Figure 8. Static test rigs with tri-cluster rocket motors.

Mass of propellant (kg)	Web thickness w_0 (m)	Internal diameter d_0 (m)	Outer diameter D (m)	Total length of grain L (m)	Aspect ratio (η)	Chamber pressure (MPa)
4.26	0.0360	0.0380	0.110	0.277	2.518	5.676
4.59	0.0276	0.0497	0.105	0.373	3.547	8.160
5.19	0.0360	0.0380	0.110	0.338	3.070	7.133
5.97	0.0276	0.0497	0.105	0.521	4.914	10.715

Table 1. Experimental parameters.

Sorbitol-based composite combustion equation:

$$5.53KNO_{3(s)} + 1.42C_6H_{14}O_{6(s)} + 4.11M_{g(s)} + 0.378C_{(s)} + 0.377Fe_2O_{3(s)} = 5.59CO_{(g)} + 5.44H_2O_{(g)} + 4.48KOH_{(g)} + 4.11MgO_{(s)} + 3.32CO_{2(g)} + 3.12N_{2(g)} + 2.28H_{2(g)} + 1.05K_{(g)}$$

Figure 9 depicts the behavioral pattern of the burn time as a function of the burn rate in conjunction with the modulating role of number of ignition points. It is noted from the closed form expression Eq. (16) that an inverse or semi-hyperbolic relationship holds for each of the curves asymptotically. From design consideration, ab initio prediction can be conjured for appropriate ballistic suitability (**Tables 2–4**). Secondly, reduction in burn time is noted with higher ignition points for any burn rate, by having a hold on other variables as couched in Eq. (16). Very significantly, the role of the ignition points is essential for controlling the amount of transient buildup of the combustion chamber pressure in such a manner that is helpful to fasten the occurrences of explosion if hollow cylindrical explosives are desired for military purposes. This transient pressure can be built up very rapidly and reach high levels for a very

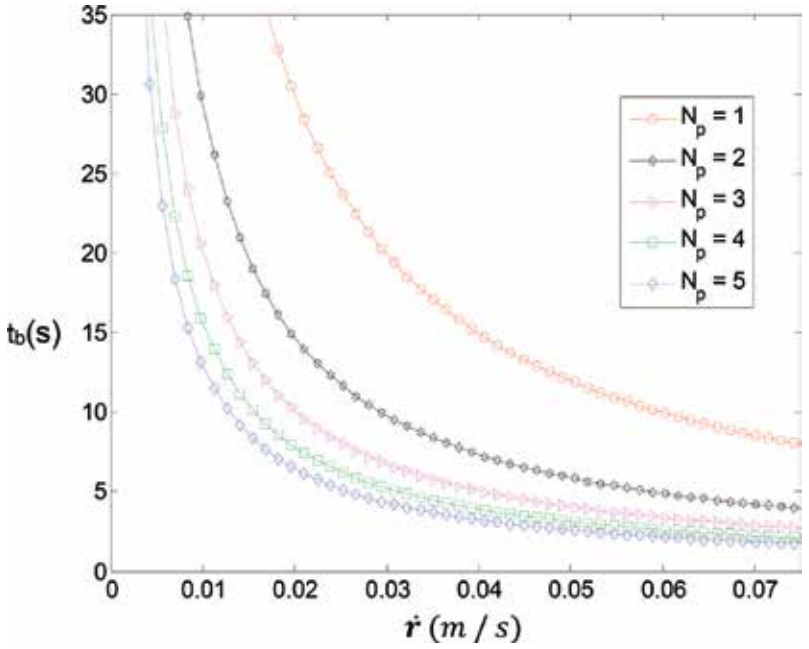

Figure 9. Plot of burn time against regression rate.

Mass of propellant (kg)	Theoretical burn time t_b (s) ($\theta = \pi$)	Theoretical burn time t_b (s) ($\theta = 2\pi$)	Experimental result burn time $t_a = t_b + t_s$ (s)
4.26	4.640	4.757	5.27
4.59	5.899	6.023	6.13
5.19	5.507	5.595	7.00
5.97	7.943	8.032	8.00

t_b, total burn time calculated; t_a, experimental burn time result; t_s, burnout time; θ, total sectorial angle covered by flame.

Table 2. Experimental results.

short burn time. It is very important to state here that such pressure value preferences must take into cognizance of the ultimate tensile strength of the combustion chamber material to forestall thermal rupturing of the walls.

In the meantime, **Figure 10** indicates the characteristic profiles of the burn time as a function of web thickness to core diameter ratio. As seen clearly, two zones are exhibited with a jump tendency in each case. Notably too, the effect of multiple ignition points is copiously observed to be very central here. As an option, a preferred burn time to govern the fuel ballistic characteristics can be selected to match desired ignition points by holding other parametric values of the grain geometry. Meanwhile, in the first zone, the burn time is noted to be fairly constant before transiting through an impulsive spark to a local peak. Beyond these points,

http://dx.doi.org/10.5772/intechopen.82822

Mass of propellant (kg)	Theoretical burn time t_b (s) ($\theta = \pi$)	Theoretical burn time t_b (s) ($\theta = 2\pi$)	Experimental result burn time t_a(s)
4.26	4.640	4.757	5.27
4.59	5.899	6.023	6.13
5.19	5.507	5.595	7.00
5.97	7.943	8.032	8.00

Table 3. Experimental results (burn time).

First set		Second set	
L (m)	0.521	L (m)	0.528
D (m)	0.105	D (m)	0.105
d_0 (m)	0.0497	d_0 (m)	0.038
$\dot{r}$ (m/s)	0.0688	$\dot{r}$ (m/s)	0.0688
a ($m^2kg^{-1}\ s^{-1}$)	0.01899		

Table 4. Table of simulation parameters.

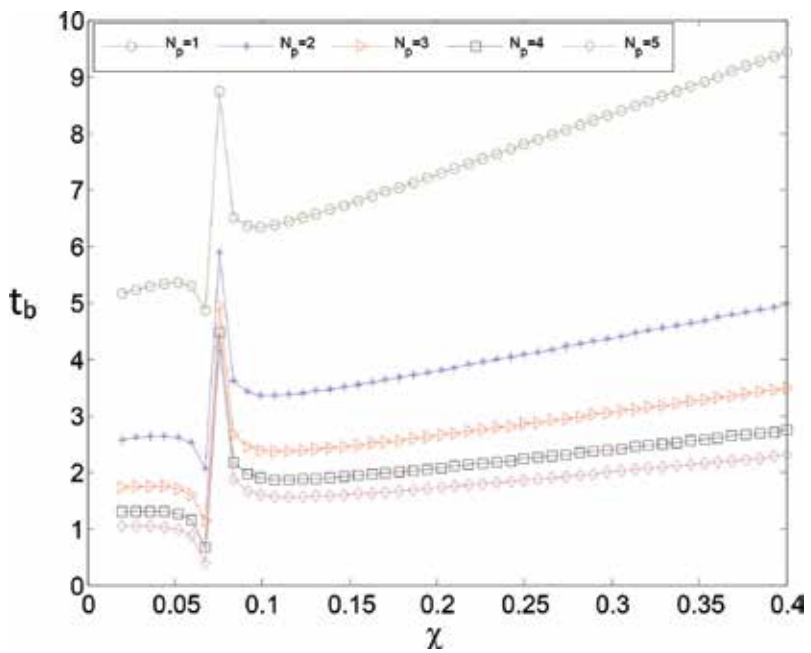

Figure 10. Plot of normalized burn time against χ.

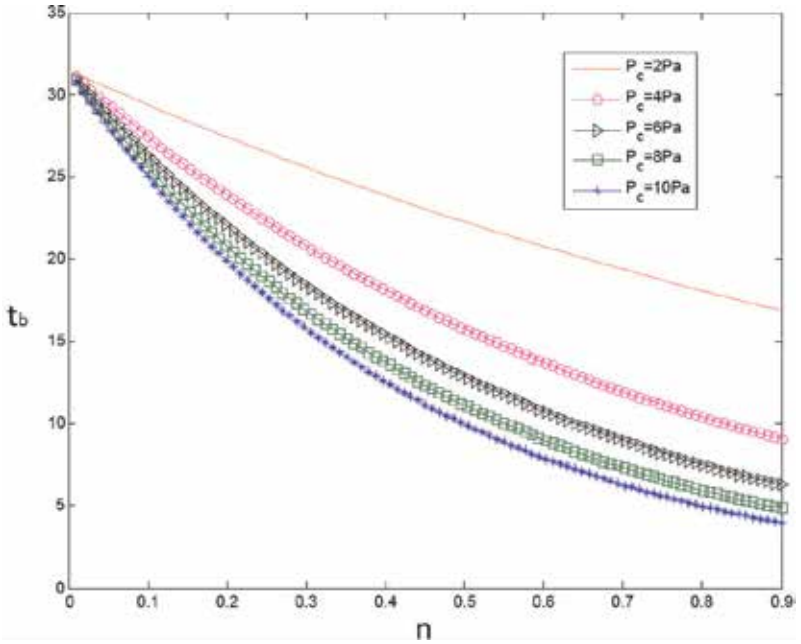

Figure 11. Plot of burn time against pressure index.

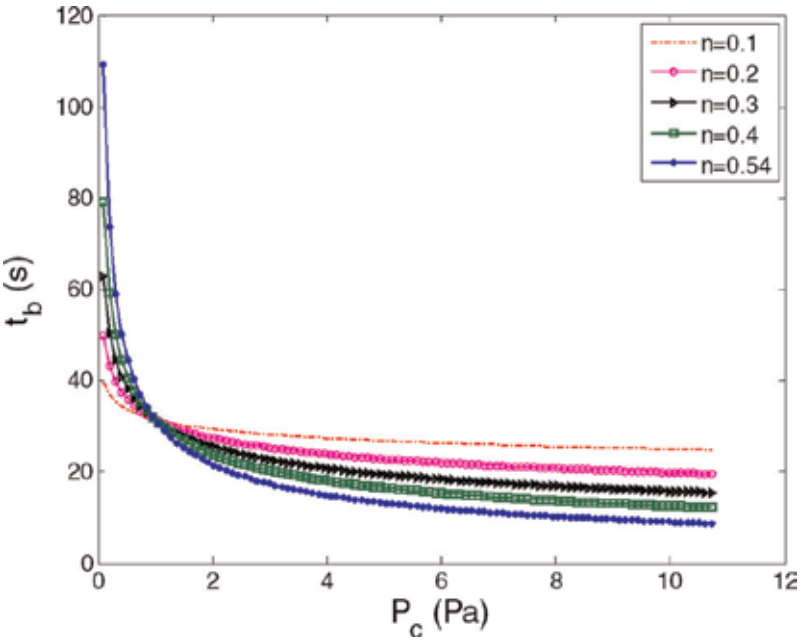

Figure 12. Plot of burn time against pressure.

http://dx.doi.org/10.5772/intechopen.82822

slight droppings are noted till sharp turning points are initiated to prompt monotonic increasing linear profiles.

In the meantime, we illustrate in **Figure 11** the characteristics of the burn time versus the propellant characterization index. Expectedly, all the curves originate from a common point irrespective of the value or quantum of the combustion chamber pressure. It is a direct consequence of Saint Robert Veille's law adopted for this study. In general, inverse relationships for any kernels must hold as can be inferred from the nature of the closed form equation tying the burn time with other parametric values deducible from empirical relations as published in literature.

Figure 12 illustrates the plot of burn time against combustion chamber pressure for any index (n). Here, we note two zones in each case where increasing pressure has decreasing effects on the burn time consistently up to a common crossover point before exhibiting reverse ordering to prompt fairly constant horizontal curves for any index value. Parts of these characteristics are previously noted in **Figure 11**. We expect these profiles to be generic irrespective of the propellant formulation and chemistry for this class of solid geometry. In grain design exercise, a number of choices are handy starting from index selection to consideration of stress tolerance of the chamber wall and aerothermodynamic properties arising from a fuel compositional chemistry and reaction kinetics.

Having examined the characteristic profiles of the burn time as modulated by specified parameters in the previous figures, we next shift focus in observing the commutative effects it is having on the burning and unburning propellant grain areas. Firstly, the behavioral pattern of

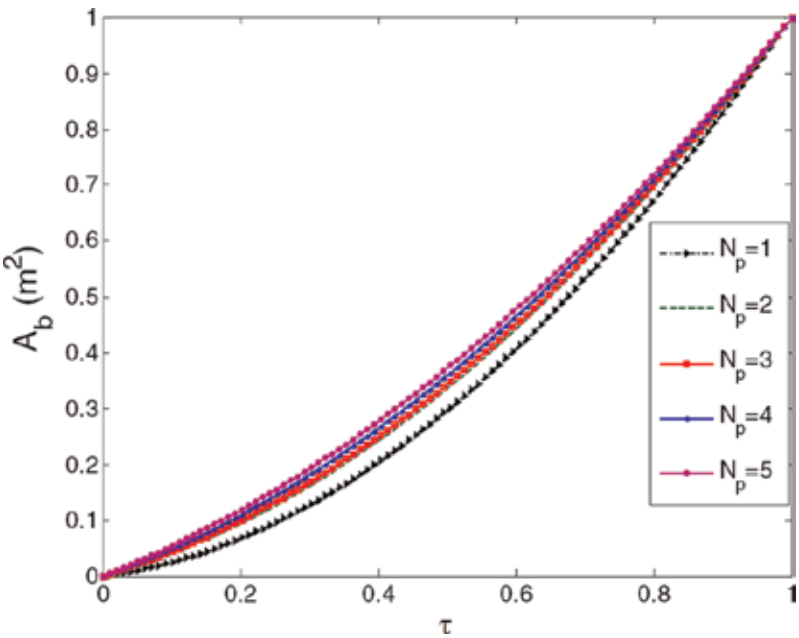

Figure 13. Plot of burnt area against normalized time.

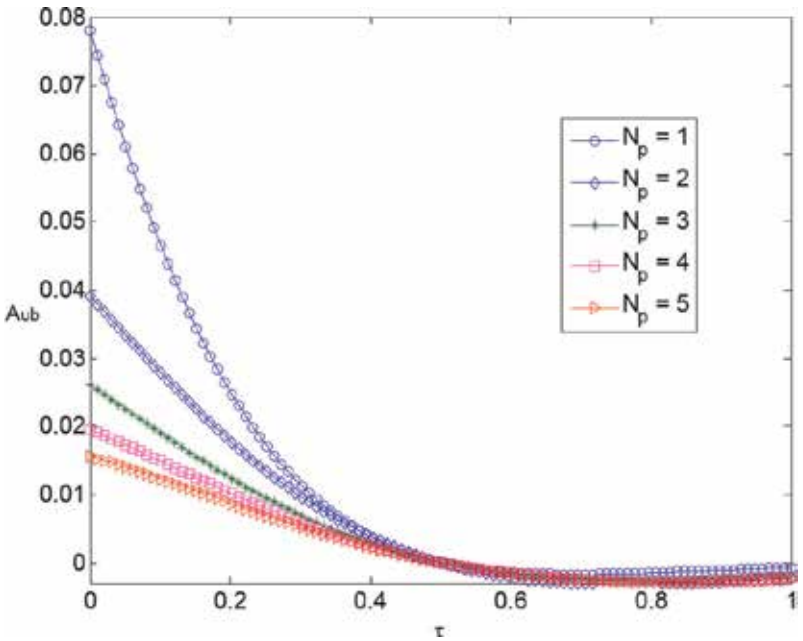

Figure 14. Plot of normalized unburnt area against normalized time.

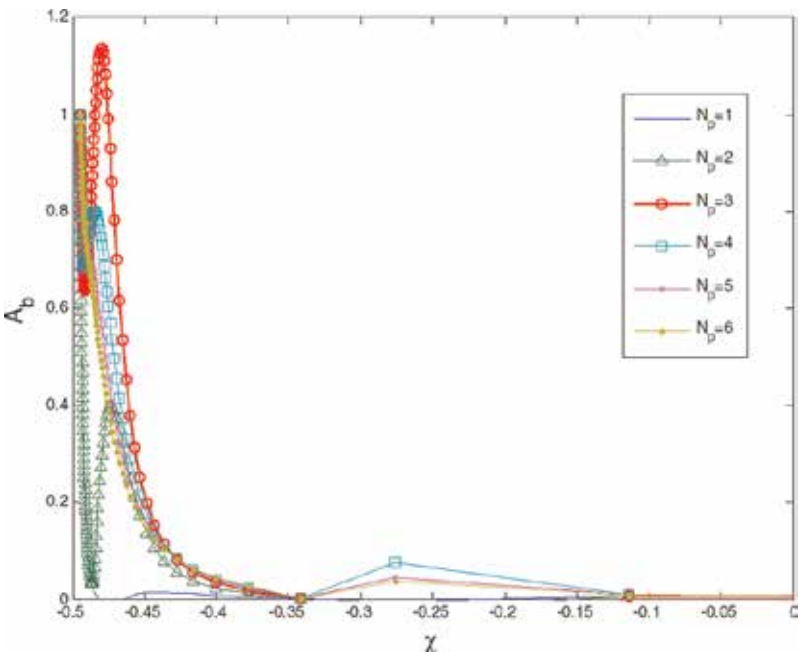

Figure 15. Plot of burnt area against χ.

http://dx.doi.org/10.5772/intechopen.82822

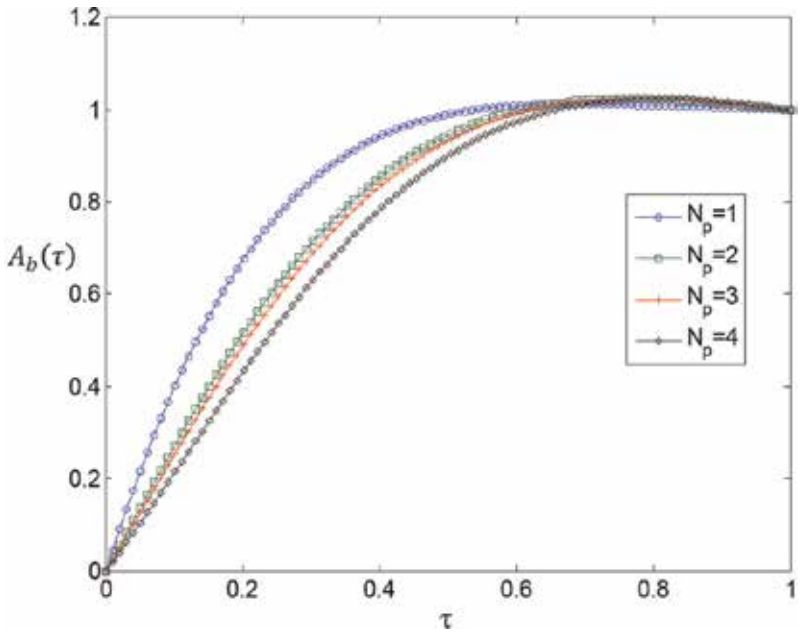

Figure 16. Plot of normalized burnt area against normalized time.

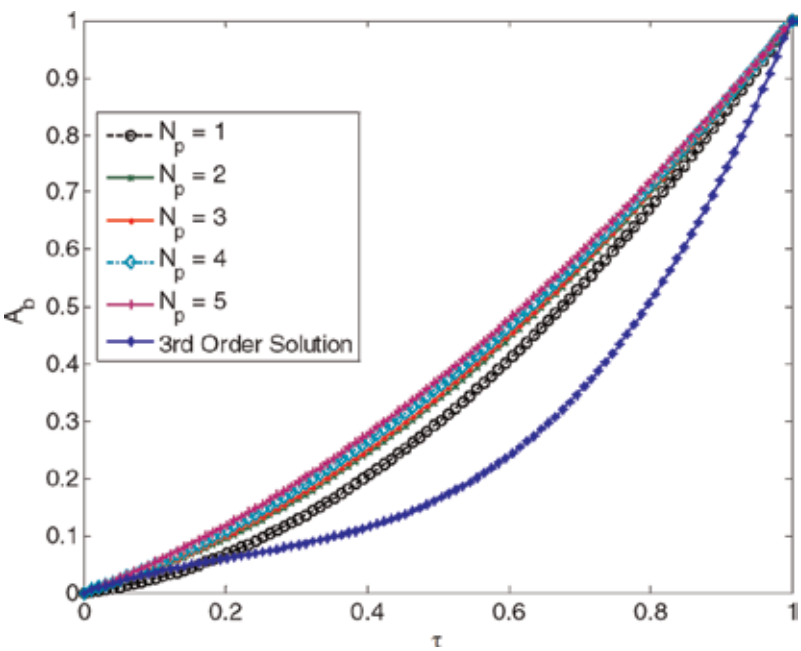

Figure 17. Comparison of a third-order polynomial approximation with kinematic prediction of burn area against time.

the burning area against the normalized burn time is illustrated in **Figure 13**. As can be seen, ordering is in consonance with increasing number of ignition points. Note clearly too that profiles are curvilinear for all the ignition points. We now proceed further to the case of the ordinary differential equation model in the illustration. Next, as seen, ordering is in reverse consonance with increasing number of ignition points. Note clearly that the pattern of profiles is curvilinear for all the ignition points. These distinct appearances are apparently visible from the onset, while overlapping tendencies are exhibited from the midpoint of the normalized time. This is possibly sequel to the segmental placement of the ignition points, to reduce the unburnt areas proportionally as indicated in the vertical axis of the plotted figure.

At this point, we shift focus to studying the ordinary differential equation model for predicting the behavioral pattern for a temporal dependent closed form unburnt grain depreciation conjectural result. The mathematical functional relation is a geometrically decaying exponential kernel that is tied to the parametric variables linking a number of factors ranging from the aspect ratio to the web thickness and the number of points at which the propellant bate is ignited. **Figure 14** depicts the behavioral pattern of the unburnt area as a function of normalized time in conjunction with the modulating role of ignition points. As can be seen, all the curves exhibit a decaying exponential characteristic. This is expected, as Eq. (41) is an exponential function. Next, as seen, ordering occurs in the order of increasing ignition points.

Figure 15 is a plot of Eq. (58) to demonstrate the modulating roles of web thickness to core diameter ratio (χ) on the burning area propagation for one to multiple (six) ignition points in

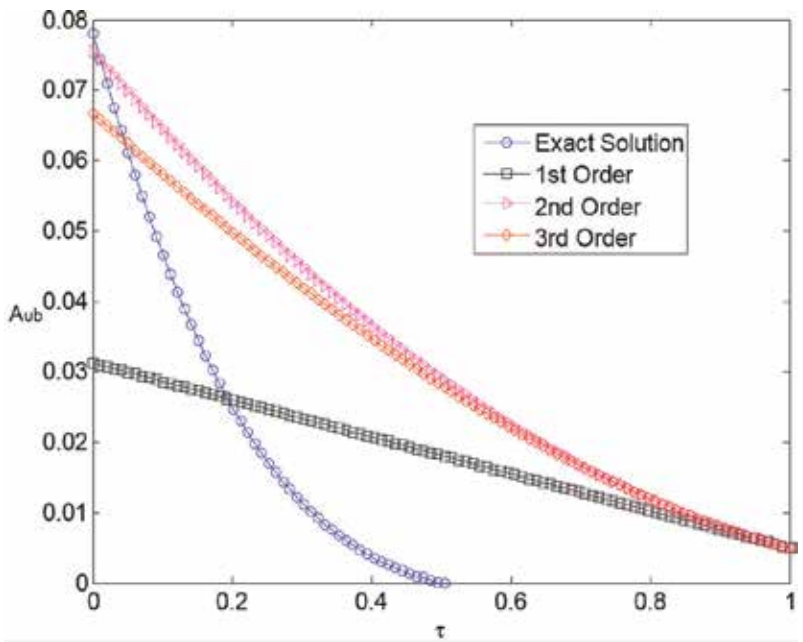

Figure 18. Plot of polynomial approximations of normalized unburnt area.

http://dx.doi.org/10.5772/intechopen.82822

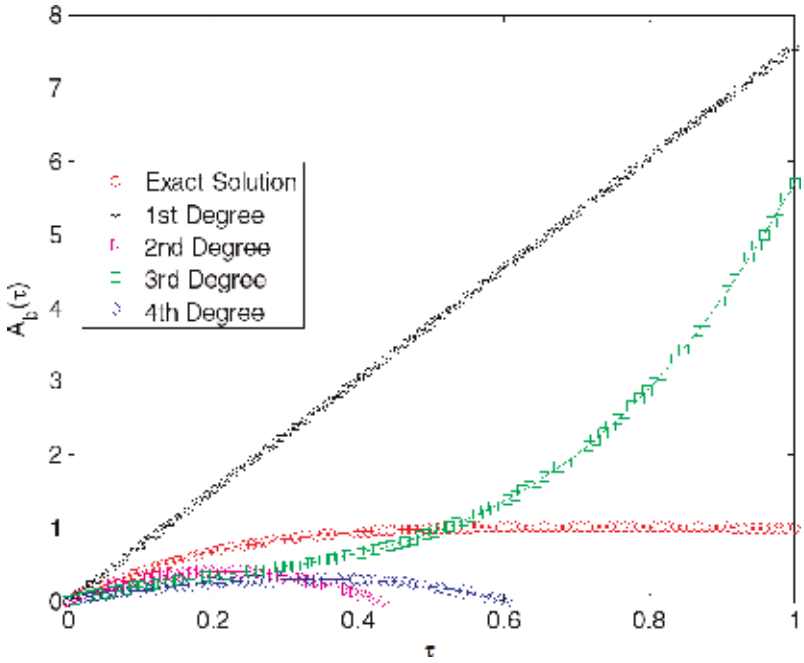

Figure 19. Plot of polynomial approximations of normalized burnt area: Eq. (54).

the range of χ hyperbolic profiles as noted for $N_p = 1$ and $N_p = 2$. A turning point is initiated at the maximum point and thereafter decreases asymptotically.

The profile of non-dimensionalized burnt area with respect to normalized time is depicted in **Figure 16**. Firstly, for the different numbers of ignition points simulated, the normalized burnt area has a characteristic increasing curvilinear signature. Secondly, the curves are ordered with increasing ignition points. There is also an overlap of the curves at the beginning and end points.

The kinematic prediction of burn area against time is illustrated in **Figure 17**. As can be seen, the profiles are curvilinear for all the points of ignition. With increasing number of ignition points, the curvilinear signature tends toward a linear profile. Next, as seen, ordering is in reverse consonance with increasing number of ignition points. Note clearly that the profiles are curvilinear for all the ignition points. These distinct appearances are apparently visible from the onset, while overlapping tendencies are exhibited from the midpoint of the normalized time. The third-order burnt area propagation profile also exhibits a curvilinear profile that is similar to the kinematic prediction.

The polynomial approximations of unburnt area propagation of the propellant are depicted in **Figure 18**. For all orders of the polynomial approximations, profiles are fairly linear with monotonic decreases. The exact solution on the other hand is a decreasing curvilinear profile with a steeper slope than the approximations. All the polynomial approximations have approximately equal values of unburnt area at onset of the time period and decrease to the

same value at the end of the burning. The value at the end of the period can be regarded as the unburnt propellant residue.

The profiles of first- to fourth-degree approximate burnt area propagation and the exact polynomial solution are shown in **Figure 19**. The exact solution manifests an initial increasing curvilinear feature for the first half of the burning period. During the second half of burning, the burnt area is constant until the end of the period. The second- and fourth-degree approximations have similar profiles. They rise to a maximum and fall curvilinearly to zero. The first-degree polynomial increases linearly throughout the period, while the third-degree approximation rises curvilinearly to a value above the exact solution.

7. Conclusion

This chapter proposes the derivation of equations to predict burn time, burning and unburnt area propagation of a tubular propellant grain. A regressive solid fuel pyrolysis in a cylindrical combustion chamber is assumed to hold. The behavioral patterns of simulated results reveal the modulating impact of variables on the burning propagation due to the kinematic and mathematical models. Closed form expressions are couched in terms of the propellant grain geometrical constraints. In addition, for the burn time, a close conformity between theoretical models and experimental results is shown.

Our findings include:

1. The reduction in burn time is noted with higher ignition points for any burn rate, by having a hold on other variables as couched in Eq. (16).

2. An inverse or semi-hyperbolic relationship holds for the relationship between burn time and the burn rate.

3. Increasing pressure has decreasing effects on the burn time consistently up to a common crossover point.

4. The profiles of burn area with time are curvilinear for all the points of ignition. With increasing number of ignition points, the curvilinear signature tends toward a linear profile.

The above find application in the use of variable number of ignition points for controlling the amount of transient buildup of the combustion chamber pressure. This helps to fasten the occurrences of explosion if hollow cylindrical explosives are desired for military purposes. Also, preferred burn time to govern the fuel ballistic characteristics can be selected to match desired ignition points by holding other parametric values of the grain geometry constant. In grain design exercise, different parameters can be altered, namely, pressure index selection to consideration of stress tolerance of the chamber wall and aerothermodynamic properties arising from a fuel compositional chemistry and reaction kinetics.

Nomenclature

A	constant.
W	Web thickness of tubular propellant grain.
L	Length of tubular propellant grain.
A_s	Sectorial area of tubular propellant grain.
$\dot{r}$	Constant regression rate.
χ	Ratio of web thickness to diameter.
η	Aspect ratio; ratio of propellant bate length to diameter.
A_{ub}	Unburnt area.
A_b	Burnt area.
N_p	Number of ignition points.
λ_p	Propagation constant/sec.
P_c	Combustion chamber pressure.
n	Propellant characteristic index.

Author details

Charles A. Osheku*†, Oluleke O. Babayomi and Oluwaseyi T. Olawole

*Address all correspondence to: charlesosheku2002@yahoo.com

Centre for Space Transport and Propulsion, National Space Research and Development Agency, Federal Ministry of Science and Technology, Lagos, Nigeria

†On Leave of Absence from the Department of Systems Engineering, Faculty of Engineering, University of Lagos.

References

[1] Tseng IS, Yang V. Combustion of a double-base homogeneous propellant in a rocket motor. Combustion and Flame. 1994;**96**:325-342

[2] Roh TS, Tseng IS, Yang V. Effects of acoustic oscillations on flame dynamics of homogeneous propellants in rocket motors. Journal of Propulsion and Power. 1995;**11**:640

[3] Roh T-S, Apte SV, Yang V. Proceedings of the Combustion Institute. 1998;**27**:2335-2341

[4] Roh T-S, Yang V. AIAA Paper No. 96-2623

[5] Roh T-S, Apte SV, Yang V. Progress in Astronautics and Aeronautics. 2000;**185**:837-857

[6] Apte S, Yang V. Proceedings of the Combustion Institute. 2000;**28**:903-910

[7] Zmelter J, Ortiz P. Burning surfaces evolution in solid propellants: A numerical model. Proceedings of the Institution of Mechanical Engineers, Part G: Journal of Aerospace Engineering. **221**(3):429-439

[8] Atwood AI, Ford KP, Wheeler CJ. High pressure burning rate studies of solid rocket propellants. Progress in Propulsion Physics. 2013;**4**:3-14

[9] Favaró FM, Sirignano WA, Manzoni M, DeLuca LT. Solid-fuel regression rate modeling for hybrid rockets. Journal of Propulsion and Power. 2013;**29**(1)

[10] Krier H, Rajan S, Van Tassell WF. Flame-spreading and combustion in packed beds of propellant grains. AIAA Journal. 1976;**14**(3):301-309

[11] Jackson TL, Zhang J, Topalian V. Erosive burning of solid propellants. In: 48th AIAA Aerospace Sciences Meeting Including the New Horizons Forum and Aerospace Exposition; 4–7 January 2010; Orlando, Florida

[12] Kadosh JS. A general note on modeling approaches for solid rocket fuel burning. Green Lightning Research Paper SRM-01. August 2018. Available from: http://www.greenlightningresearch.com/pubs/GLR_paper_SRM-01.html

[13] Greatrix DR. Transient burning rate model for solid rocket motor internal ballistic simulations. International Journal of Aerospace Engineering. 2008;**2008**:826070

[14] Willcox MA, Quinn Brewster M, Tang KC, Scott Stewart D, Kuznetsov I. Solid rocket motor internal ballistics simulation using three-dimensional grain burnback. Journal of Propulsion and Power. 2007;**23**(3)

Chapter 5

Ballistic Testing of Armor Panels Based on Aramid

Catalin Pirvu and Lorena Deleanu

Additional information is available at the end of the chapter

http://dx.doi.org/10.5772/intechopen.78315

Abstract

Industry and market of ballistic protection materials and systems are characterized by a dynamic and competing succession of inventions for projectiles and protective systems. The requirements for the ballistic panels are many and complex, varying depending on the threat type, the required mobility in the tactical theater, and protection level. The safety degree, the price, and the dynamics of research in the field are also taken into account. This chapter underlines the necessity of testing ballistic protection panels made of LFT SB1 plus (multidirectional fiber fabrics, supplied by Teijin) against a certain threat in order to assess their resistance to this specific threat and the investigation of failure mechanisms in order to improve their behavior at ballistic impact. The models for ballistic impact are useful when they are particularly formulated for resembling the actual system projectile, target, and can be validated through laboratory experiments. Tests made on panels made of LFT SB1plus, according to NIJ Standard-0101.06-2008 gave good results for the panels made of 12 layers of this fabric, and the backface signature (BFS) was measured. The BFS upper tolerance limit of 24,441 mm recommends this system for protection level IIA, according to the abovementioned standard.

Keywords: ballistic impact, aramid fabrics, damage investigation

1. Introduction

Industry and market of ballistic protection materials and systems are characterized by a dynamic and competing succession of inventions for projectiles and protective systems. The requirements for the ballistic panels are many and complex, varying depending on the threat type, the required mobility in a tactical theater, and protection level. The safety degree, the price, and the dynamics of research in the field are also taken into account. The research on hit targets by a projectile characterized by more than 120 m/s is of high interest nowadays in several important domains, like army, navy, space systems, and nuclear one. The intensive

competition on polymeric, woven or not, fabrics and the growth of their market at a global level are factors that bust research toward efficient innovations, including the assembling technologies here.

The initial design of a protective system is supported by simulations using sophisticated codes that take into account the material characteristics under a high strain rate and particular processes characterizing the impact (friction, heating, material modifications concerning phase and structure, stratifications, and/or the fibers arrangements, etc.). Simulations by the help of finite element method (FEM) or smoothed-particle hydrodynamics method (SPH) [1] of the impact have become an initial stage in designing new systems, but the experimental validation of models is asked by the particular use of the protective system. The tests on ballistic systems or panels are strictly necessary for evaluating the impact level and for identifying factors influencing penetration and failure mechanisms that could help improve the already existing systems.

Starting from these considerations, the main goal of the study "Ballistic testing of armor panels based on aramid fibers" is the concern of balancing innovations of destructive systems (projectiles, fragments, bullets, etc.) with those that are designated to protect personnel and equipment, using materials like fabrics, woven or multidirectional, stratified and complex composites. At a low speed, even glass fiber fabrics could have satisfactory results [1], but for protecting personnel and equipment at a higher impact velocity, aramid and ultrahigh density polyethylene fibers are more efficient (**Figure 1**) [1, 2].

Even if simulation and modeling offer results closer to the actual processes by using new principles and performance codes and computers in solving impact issues, the experimental work is the final and main stage for the approval of new and improved protective systems. In terminal ballistics, experimental complex techniques, specific equipment, and a testing methodology are required to determine the performance of both the projectile and the protection system and, ultimately, by analyzing the results, to characterize and improve the

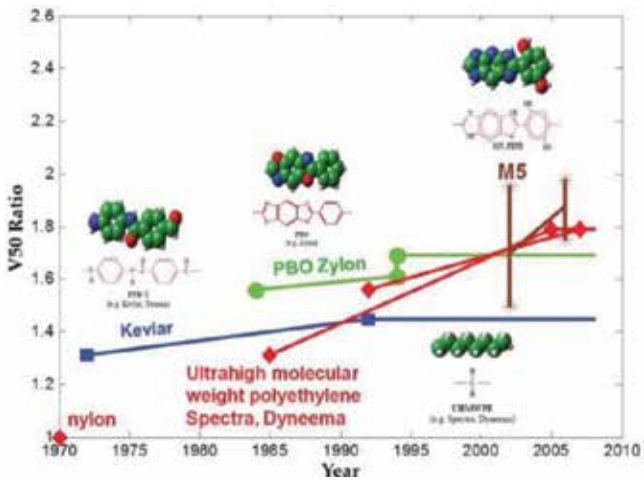

Figure 1. An increase in ballistic performance as a function of the fiber type used in manufacturing body armor [1].

protection system. If, in a classic war, the splinters and fragments are the most dangerous, in other conflicts, bullets remain a major threat to lives and physical integrity of fighters and civilians, representing the main cause of human loss, including during peacetime.

Bullets differ in caliber, initial velocity, mass, jacket, core and shape, and so on. A bullet must have a considerable kinetic energy when reaching the target to penetrate it. In terms of terminal ballistics, mechanical work involves many aspects of bullet-target interaction. Part of the energy is transformed into heat, a part is lost by friction, and the other part by rotating the bullet, by elastic and plastic deformation of both bullet and target. It is a practical impossibility to produce individual ballistic protection equipment that provides total security for the whole arsenal, given the drastic constraint imposed by the limitation of the total mass of protective equipment that a combatant or a user can wear.

In order to assess the impact resistance of protective panels, there are reference standards that offer test methods and procedure, as found in [3]. The test results give the possibility of including ballistic panels in a level of protection. For individual armor front panels, the standards require the absence of perforation for a determined number of repetitions under the same firing conditions, plus a condition related to the depth of the trace generated in a support material (ballistic clays) after impact [4].

The purpose of this chapter includes the process of manufacturing specific flexible ballistic panels made of quatro-axial fiber fabrics in layered composites, tested at fire with 9-mm bullet and 400 m/s (II and IIA protection levels, according to [4]), followed by an investigation of processes and stages of deterioration using scanning electron microscopy (SEM) and macrophotography of the failed zones of the panels after the bullet recovery. Also, a statistical analysis of the depth in the support material [backface signature (BFS)] is presented.

2. Manufacturing and testing the flexible panels

Personnel armor for ballistic protection includes both body systems and helmets. The threats for which this armor is designed are small-caliber projectiles, including bullets and fragments. The level of ballistic protection is taken as the total kinetic energy of a single round that the armor can stop [5].

For polymeric, carbon, ceramic, and glass fibers, researchers reported that the tensile strength increases with decreasing their diameter. For polymeric fibers (**Table 1**), diameters are in the range of 10–15 μm, greater than those for carbon fibers (4–10 μm), but smaller than fibers obtained by chemical vapor deposition, such as boron fibers (100–150 μm). The probability of defects decreases with decreasing the fiber diameter.

Fabrics from fibers and yarns by weaving allow for designing panels that can face both ballistic and blast events. Most ballistic fabrics have two-dimensional plain weave yarns in two orthogonal directions, although some work is being done on three-dimensional weaves and on nonwoven and knitted fabrics [6, 7]. Polymers, glass, and ceramic fibers have high stiffness and high strength-to-weight ratios. From less a decade, the unidirectional and multidirectional

Polymeric fibers	Density (g/cm^3)	Modulus (GPa)	Tensile strength (GPa)	Compressive strength (GPa)	Strain-to-failure (%)
Nylon 66	1.14	4.3			25
Silk	1.36	30–60	1.1–2.9		7–12
Kevlar 49	1.45	12.5	3.5	0.4	2.6–4.2
Kevlar 149	1.47	18.5	3.4	0.4	
Kevlar 1000		8.9	2.4–3.4	0.4	2.8–3
Zylon HM	1.56	27	5.8	0.3	2.5
M5 (PIPD)	1.70	27	> 4		>1.4
Vectran	1.47	65	2.9		3.3

Table 1. Typical properties of fibers [2].

fabrics made of polymeric and glass fibers tend to replace the woven ones for certain applications, including panels for the ballistic protection of personnel and equipment.

Figure 2 and **Table 2** present characteristics of threats, as classified by NIJ Standard-0101.06.2008, Ballistic Resistance of Body Armor, and it is obvious that the kinetic energy is the key parameter that will destroy a body armor, for each level of protection.

Many parameters influence the response of fabrics to ballistic impact. These include material properties of and yarn, fabric architecture, boundary conditions, inter-yarn friction, friction between the projectile and the yarn, projectile geometry and velocity, impact direction, and environmental conditions.

The designers of body armor take into account the specific threat that has to face the vest and the helmet. Depending on these threats, the protective body system could be made of polymeric, metallic, and/or ceramic materials, and engineers have to select them. Vests made of

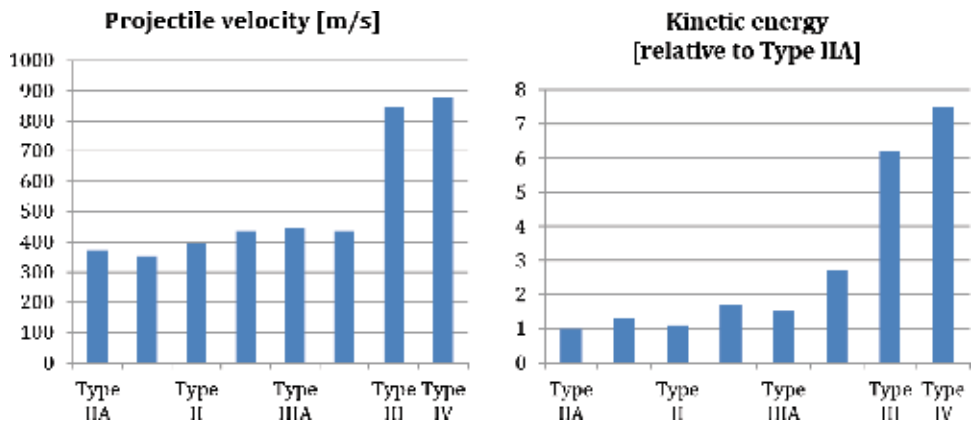

Figure 2. Characteristics of threats as given by NIJ Standard-0101.06. 2008.

Level	Projectile
II	9 mm full-metal-jacketed round nose (FMJ RN) 0.40 S&W FMJ
IIA	9 mm FMJ RN 0.357 magnum-jacketed soft point(JSP)
III	0.357 SIG FMJ flat nose (FN) 0.44 magnum semi-jacketed hollow point (SJHP)
IIIA	7.62 mm FMJ, steel-jacketed bullets (U.S. military designation M80)
IV	0.30 caliber armor piercing (AP) bullets (U.S. military designation M2 AP)

Table 2. Levels of ballistic resistance [5].

only polymeric materials are intended for protecting human body against fragments and lower velocity projectiles. Glass fibers and polyamide fibers were firstly used, but polyaramid fibers, introduced by DuPont [8] and later by Teijin [9], make the armor lighter and more reliable for a greater ballistic limit V_{50}. In the 1980s, fibers made of high-molecular-weight polyethylene (UHDWPE) and polybenzobisoxazole (PBO) have also been used.

Body armors have to fulfill two types of requirements:

- to arrest (stop) the projectile within the armor, even to withstand multiple hits on the same armor panel, depending on the protection level the armor is classified in; and
- to have a deflection that would not severely injure the wearer.

There is no universal method to design an armor system, but the report "Opportunities in Protection Materials Science and Technology for Future Army Applications" [10] gives a flow chart of activities for homologating a new or a redesigned armor, pointing out the place and importance of simulation based on the actual material properties when bearing a high strain rate as in ballistic impact (**Figure 3**). Certainly, the main stage in evaluating the armor is the shoot test.

New materials are developed, but these are infrequently selected for protective systems because their behavior in actual events and configurations is not directly related to the laboratory tests. Moreover, most non-armor application materials are chosen according to their bulk quasi-static properties, even though such properties do not always predict their ballistic performance. If the constitutive relations for properties characterizing new materials needed for running simulations are not known, then the engineer has to use information from the most similar existing material [11], making the result uncertain. This is another reason why armor designers do not consider using new-entry materials that have not yet been sufficiently characterized under particular dynamic conditions. The simulation is often done as a guide to identify trends due to design modifications than as a source of practical results. The modeling of a protective system or a panel is difficult to do at different levels [12, 13]. For instance, the panel made of polymeric fibers of an armor could be considered as a stratified material at macro-level (**Figure 4**), but each layer is a fabric, woven or unidirectional, that contains yarns, their cross-dimensions being thousand times smaller than their length. This could be a

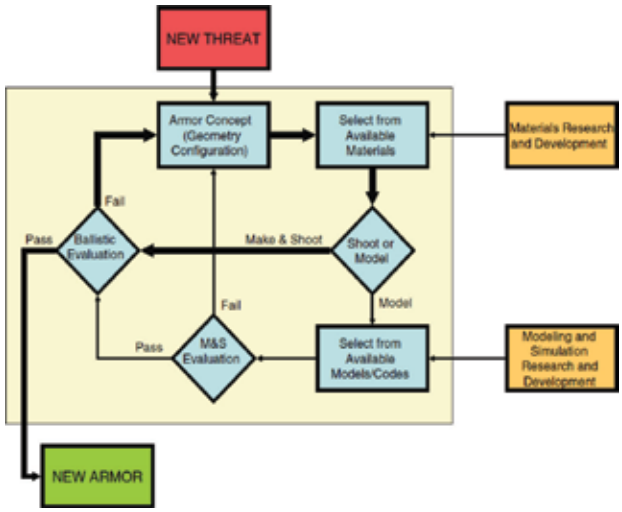

Figure 3. Flow chart of new or redesigned armor [10].

mezzo-level in modeling [14]. And there is the micro-level: each yarn contains hundreds of fibers, their diameter also being smaller by several orders of magnitude. The simulation could not cover all these levels at the same time, in one model, and the designers have to rely on their experience and ingenuity to generate a model that could help restraining the feasible solutions.

The panels were made of layers of Twaron LFT SB1plus, as supplied by Teijin Aramid [9], a new entry on the market in 2012. The four sublayers of LFT SB1plus, laminated together with a very thin sheet of resin, are visible as shown in **Figure 5**: the angle positioning of the

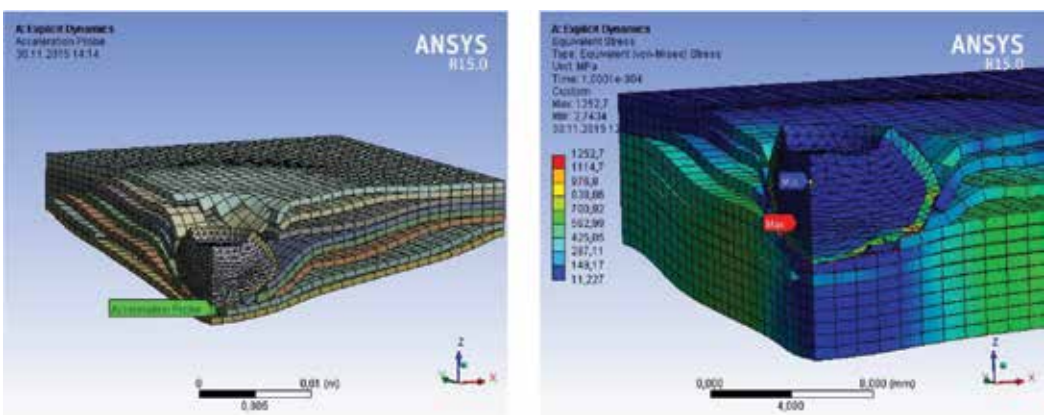

a) 8 layers (t=10⁻⁴ s), 7 broken layers

b) 12 layers (t=10⁻⁴ s), 4 broken layers

Figure 4. A simplified isothermal macro-model of a flexible panel (v = 400 m/s, friction contact between bodies**:** Friction coefficient between layers 0,4, friction coefficient between layers and bullet: 0.3 [14], bilinear hardening constitutive models for materials) (see **Table 3**). (a) 8 layers (t = 10^{-4} s), 7 broken layers. (b) 12 layers (t = 10^{-4} s), 4 broken layers.

unidirectional yarns of sublayers being 0, 90, 45, and −45° and the specific area density 430 g/m^2. The layers in a panel were secured by sewing on two edges to maintain the integrity and order of the layers. The sewing line had a length of approx. 200 mm, made at 25 mm from the panel edge, with a step of 2–2.5 mm.

The manufacturing of the panels consists of cutting squared layers of 500 × 500 mm, having an area of 0.25 m^2, from fabrics with the width of 1200 mm. The area value positioned these panels between NIJ-C-4 (0.23 m^2) and NIJ-C-5 (0.3 m^2) for large and very large surfaces. After cutting the squared layers, these were arranged in three types of panels, each one containing a different number of layers: 4, 8, and 12, respectively (**Table 4**). The number of layers was selected after a simulation [14] at macro-level (**Figure 4**), with layer properties similar to aramid fiber, as given in the study [15].

Taking into account the standard Ballistic Resistance of Body Armor, NIJ Standard-0101.06, U.S., 2008, the test plan for flexible ballistic protection panels based on aramid fibers included the fire with 9-mm bullet for level II and level IIA (**Figure 6**).

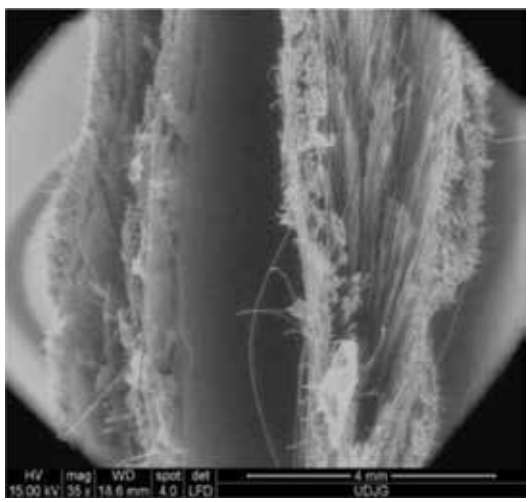

Figure 5. Cross section on a LFT SB1plus fabric (4 sublayers (0, 90, 45, −45), each one with unidirectional yarns).

Material	Young modulus, Pa	Poisson coefficient	Bulk modulus, Pa	Shear modulus, Pa	Yield limit, Pa	Tangent modulus, Pa	Max. equivalent plastic strain, EPS
Layer	7×10^{10}	0.35	7.77×10^{10}	2.59×10^{10}	6.3×10^{8}	1.9×10^{10}	0.06
Copper alloy (bullet jacket)	1.1×10^{11}	0.34	1.14×10^{11}	4.10×10^{10}	2.8×10^{8}	1.15×10^{9}	—
Lead alloy (bullet core)	1.6×10^{10}	0.44	4.44×10^{10}	5.55×10^{9}	3×10^{7}	1.1×10^{8}	—

Table 3. Material properties for the impact model bullet—Stratified pack [11].

Panel	Number of layers	Calculated mass (g)
LFT SB1 plus	4	450
	8	900
	12	1300

Table 4. Calculated mass of a flexible panel.

In order to evaluate the impact resistance of the protective panels, there are reference standards proposing testing methods, the results being ranked as a protection level, characterized especially by the projectile mass and velocity. For panels used as body armor, these standards require the absence of total perforation and a supplementary condition of limiting the back deformation as human body could not face a high deformation without critical injuries, even fatal, even if the bullet does not penetrate this one. As testing directly on the human body is not recommended neither ethical, panels are required to have a maximum value in a support material that could be similar (in a closer manner) to the human body response, as, for instance, the ballistic clay.

The impact velocity (just before hitting the target) was measured with the help of a system including a chronograph Oehler model 43, stable for the temperature range of 5–40°C and having an accuracy of 0.3%. Other measurement devices used for these tests were a ballistic barrel for bullets of 9-mm FMJ (fulfilling the requirements of NIJ 0101.04/2000) and a fire arm table with a blow-back compensation [4], a hygrometer with an accuracy of 1%, a barometer with an accuracy of 1 mm Hg, a thermometer with an accuracy of 1°C, a box for the ballistic clay, an oven allowing for tempering at 20 ± 5°C, a climate enclosure allowing for maintaining a temperature of 20 ± 5°C, and an oven for ammunition conditioning. A partial view of the test facilities is presented in **Figure 7**.

The shooting was done in the Scientific Research Center for CBRN Defense and Ecology laboratory, by specialized personnel in order to fulfill the requirements of reference [4], including the arrangement shown in **Figure 8**, the distance between fires and the distance from

Figure 6. Tested panel made of 12 layers of LFT SB1plus.

Figure 7. Fire laboratory at the scientific research center for CBRN defense and ecology, Bucharest, Romania.

the panel edges and the regulations of protection, specific to this type of laboratory, being observed [16].

The framed box has the dimensions 610 × 610 × 140 mm (±2 mm). The back of the box is detachable, and it was made of wood (19.1 mm). The frame is made of steel and helps the ballistic clay to be leveled. As recommended by [4, 5], the clay grade was Roma Plastilina no. 1, which has a durability of about 1 year. This clay must have no voids, a smooth-free surface, and it has be easy to level with a ruler, the free surface being determined by the metal frame.

The panel behavior was evaluated by the number of failed (broken) layers and by the values of backface signature (BFS). **Figure 9** presents the method of measuring the depth of the impact deformation within the support material.

The determination of ballistic resistance of protection materials and equipment at the action of infantry bullets is carried out according to NIJ Standard-0101.06 [4] (**Figure 6** presents one of the tested panels). The samples were tested with a ballistic pipe (with a measured velocity of

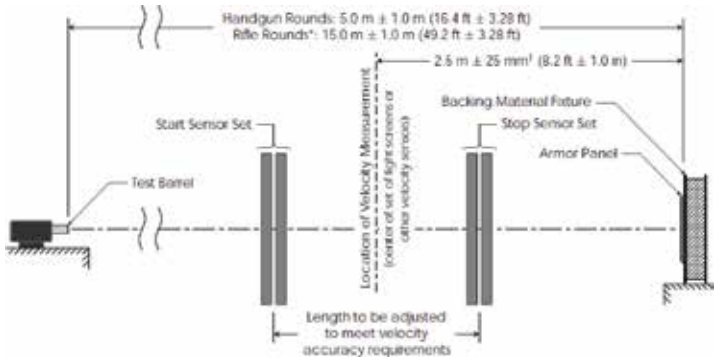

Figure 8. Shooting arrangement [4].

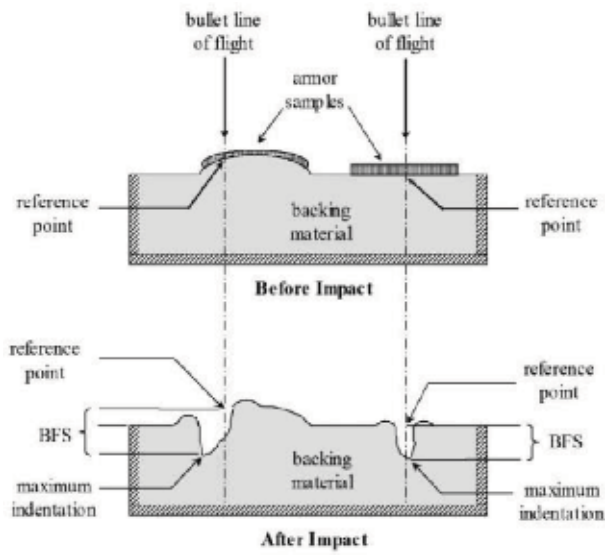

Figure 9. Measuring the BFS according to ballistic resistance of body armor, NIJ Standard-0101.06, U.S., 2008 [4].

430 ± 10 m/s), with a projectile of 9-mm full metal jacket (FMJ) bullet. The deformation remained in the ballistic clay (backface signature or BFS) that was measured according to [4], with a depth caliper, with an accuracy of ±0.1 mm. After each measurement, the calipers were cleaned to avoid any traces of clay on the measuring area. The evaluation of the total penetration of a package is in many cases simple, when a hole with a diameter at least equal to the size of the bullet is found and the entire bullet passes through it. When testing individual ballistic protection equipment, the trauma to the human body is evaluated by the depth of the print that is formed in the clay on which the sample is fixed.

Environmental parameters inside the fire enclosure were as follows: temperature: 20°C (±5°C), relative humidity: 50–70%, atmospheric pressure: 760 mm Hg (±15 mm Hg).

After the fire, the projectile or their fragments were removed from the clay. The clay was added anytime needed, after measuring the backface signature (BFS).

The fire procedure has the following steps:

- the test equipment is positioned in the mounting bracket at the distance required for each equipment from the muzzle; the types of armaments and ammunition required by each level of protection for which the test is being conducted, for Level II and IIA [4] in this study;
- positioning the bullet speed measurement system, starting at a distance of 2 m from the muzzle, so that the frames of the system are in planes perpendicular to the fire direction; the distance between the frames is set at 0.5 m; distance measurements are made with an accuracy of 1 mm;
- fire runs on the sample panel.

3. Evaluation of ballistic resistance for the flexible panels made of aramid fibers

At molecular level, variables in polymers include chemical makeup, the length and degree of branching of molecular chains, the degree of alignment and entanglement, and the extent of cross-linking. The types and strengths of bonds in chains and among chains influence the polymeric fiber strength and strain and influence the failure mechanisms.

The factors affecting the ballistic performance may be grouped into three categories:

- the factors of projectile (mass, velocity, materials, shape, and impact direction);
- the target architecture (material, structure at nano-, micro-, and macro-level); and
- the environment (temperature, humidity, clamping, and support material as, for instance, the human body or the car body).

When fabrics are impacted by a projectile, the target size, its clamping conditions are important. A longer yarn can absorb more deformation energy than a shorter one before failure. Thus, a larger target area will lead to a higher energy dissipation. However, this is not true when the velocity of the projectile is very high as compared to the velocity of the shock wave in the fibers since only a small zone of the target can dissipate the kinetic energy of the projectile. The boundary conditions of the target also play an important role. Shockey et al. [17] observed that a two-edge gripped fabric absorbs more energy than a four-edge gripped fabric, and fabrics with free boundaries absorb the least energy. Chitrangad et al. [18] observed that when pretension is applied on aramid fabrics, their ballistic performance is improved. Zeng et al. [19] observed that for four-edge gripped fabrics, energy absorbed is improved if the yarns are oriented at 45° relative to the edge.

The number of fabric plies or sublayers also affects the ballistic performance (note that typically there may be 20–50 plies). Shockey et al. [17] observed an increased specific energy absorbed for multi-ply targets due to friction forces between layers. The influence of interplay materials and the distance on ballistic performance have also been investigated [7]. The influence of a projectile geometry also becomes less important with an increased number of plies [20].

Frictional effects between a projectile and a fabric are observed at a low-velocity impact, but they diminish at a higher velocity [17]. Friction does help maintain the integrity of fabrics in the impact region by allowing more yarns to be involved in the impact and it increases energy absorption by increasing yarn strain and kinetic energy. Dischler [21] applied a thin polymeric film on Kevlar (20-ply), which increased the coefficient of friction from 0.19 to 0.27 and reported a 19% improvement in ballistic performance in stopping a flechette. Carrillo et al. [22] investigated the ballistic behavior of a multilayer Kevlar aramid fabric/polypropylene (atactic PP films of 0.032 mm and a density of 910 kg/m^3) composite laminate and simply plain-layered aramid panel (plain-woven Hexcel aramid 720 fabric, Kevlar129 fiber, 1420 denier), under a sphere impact (with a diameter of 6.7 mm and a mass m of 1.11 g), at a velocity of 274.5 m/s and found that the improved performance of composite laminate is due to the fact that the thermoplastic matrix enables energy-absorbing mechanisms, such as fabric/matrix debonding and delamination.

There is a tendency to combine high-resistance fabrics with lower cost ones, but the results are still indecisive. Yahaya et al. [28] presented ballistic properties of non-woven kenaf fibers/Kevlar epoxy-hybrid laminates with thicknesses ranging from 3.1 to 10.8 mm, when impacting with a 9-mm full metal jacket bullet at speeds varying from 172 to 339 m/s, at normal incidence, but hybrid composites recorded a lower ballistic limit (V_{50}) and energy absorption than the Kevlar/epoxy composite.

The processes evidenced by macrophotography and SEM images help for understanding the failure mechanisms specific for the designed panels with layers of LFT SB1 plus a quatro-axial fabric.

Taking into account reference works [23], several stages for this type of panels were identified:

Stage I is dominated by deformation, yarn breakage, and energy dissipation mechanisms; the moment transfer between the projectile and the fabric leads to an increase in the kinetic energy of the fabric, which initially leads to the production of the pyramidal deformation, less evident on flexible panel with unidirectional fibers (see **Figure 10** with photographs 1F-1 and 2F-1). Simultaneously, the yarns begin to stretch as the longitudinal wave propagates along the thread, leading to an increase in internal energy and/or wire deformation (statistical process). The sheet of resin, even very thin, keeps the yarns in positions, being more difficult to be laterally impelled.

Stage II is characterized by friction produced by pulling the yarns; one or more yarns can be pulled out of the fabric and a large amount of energy dissipates through this sliding friction; the rate of deceleration is lower at this step than in Stage I, but excessive yarn drawing promotes the fabric opening mechanism, the bullet pushing several yarns laterally. The fabric pattern or the way of arranging and maintaining the unidirectional yarn compaction (by sewing or a rare weaving with other types of fibers that maintain the surface density of yarns) influences the opening mechanism.

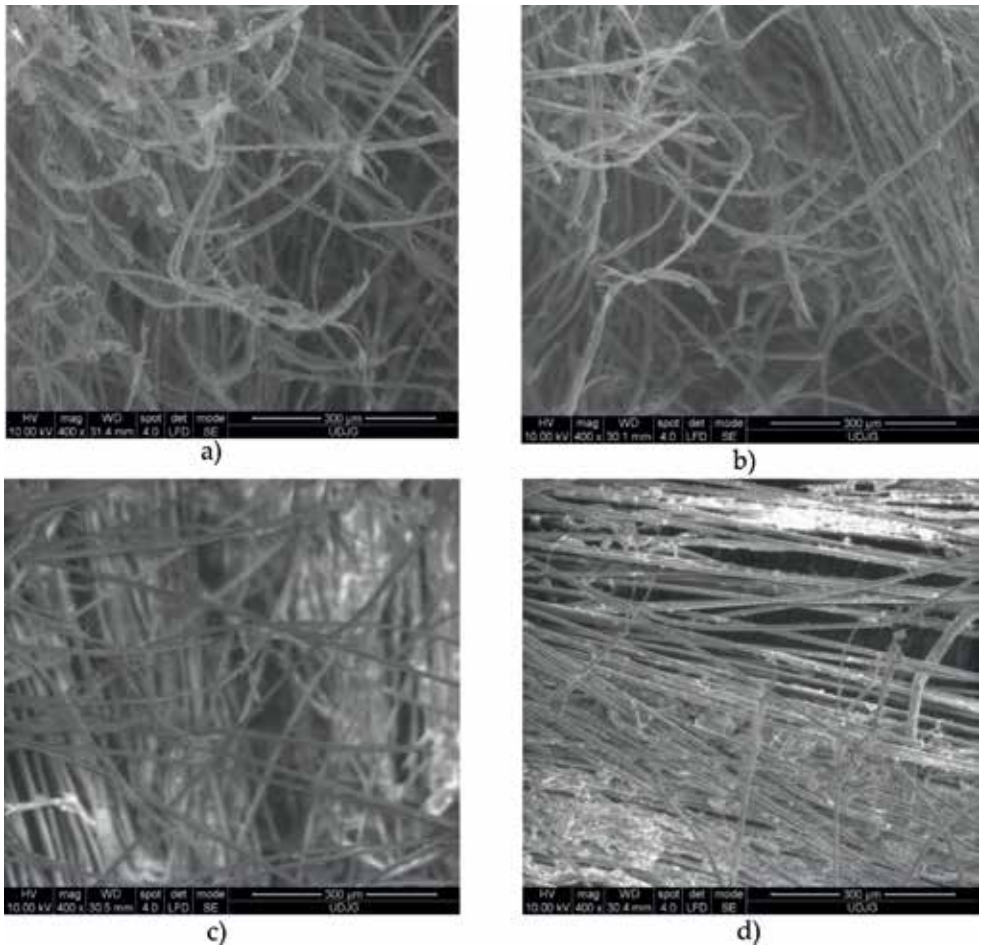

Figure 10. Posttest images of fabric damage from a panel made of a layer of LFT SB1plus, showing yarn and fibers' breakage characteristics. (a) 1F-1. (b) 2F-1. (c) Fiber damage on the front of 3-rd layers (3F-1). (d) Fiber damage on the back of the 12-th layer of a panel (12B-1).

Stage III corresponds to the postimpact region for impact without penetration, and the projectile can be arrested in the fabric. The bullet is strongly flattened, remaining with the typical aspect of mushroom (see **Figure 15**). Depending on material, projectile, and impact parameters, these steps may differ in duration and appearance.

4. Failure mechanisms of panels, yarns, and fibers by SEM and macrophotography investigations

The study of ballistic impact of fabrics includes residual velocity, stroke response, energy absorption, and tensile properties of yarns and failure mechanisms [17].

Mechanisms of energy dissipation are breaking the fibers/yarns, fibers' deformation (stretching, twisting) (see **Figures 11a** and **16c**), fiber fibrillations (**Figures 12** and **16c**), bullet deformation and cracking, local heating, acoustic energy, air entrainment, cross-sectional deformation of yarn (**Figure 16b**) and friction among yarn fibers, yarns, and also friction between these ones and the bullet.

Types of damage in filaments, yarns, and fabrics may be noticed at both micro- and macro-levels. The micro-level involves breaking bonds that are involved in the structure of the

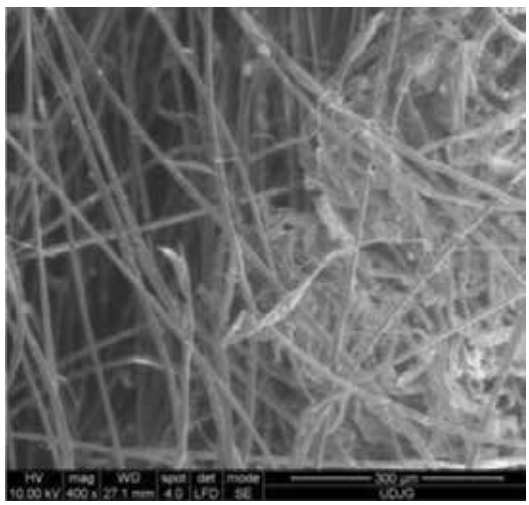

Figure 11. Fiber break in the third layer of the panel (front view, code 3F-1); less fibers with fibrillation.

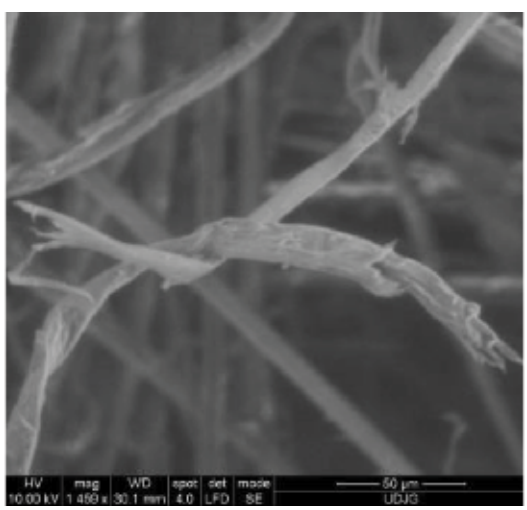

Figure 12. Fibrillation of fibers (front view, code 2F-1).

filaments, while at the macro-level, the destruction may be characterized by mechanisms such as yarn pulling or bowing.

Higher magnifications show that the fibrils in broken fibers are also stretched (see **Figure 10b**). Fiber material very likely has plastic strain but, more obviously, localized plastic ones, failure also occurring due to nucleation of voids, cracks, and shear bands. Failure initiators are thought to originate in material defects such as tiny voids, foreign particles, and chain entanglements, resulting from chemical non-homogeneities or manufacturing procedures.

Fiber failure modes other than tensile failure are also observed. The influence of the structure of polymeric fibers at nano (molecular)-level on failure behavior is not well understood, especially at high strain rates and high pressures [3].

When a projectile hits a fabric or a panel made of layers of fabrics, it is caught by the yarn network (woven or not). Kinetic energy is transferred to the fabric as the stress wave spreads outward from the point of impact. The energy is partially dissipated by fiber deformation and breakage and by friction caused by inter-fiber slippage. A projectile with a sufficiently high mass and velocity may penetrate the fabric and cause it to fail.

Figure 10 indicates that tensile fracture first occurred at defects such as voids and kinks and was assisted by the residual stresses that are induced during processing. Similar mechanisms were reported by Allen et al. [24].

For example, a projectile impact on fabric compresses the fabric against the backing layers and causes transverse loads on the yarns and fibers that can result in deformation and failure (breakage). When compressed fibers are examined by SEM, they and the fibrils show flattening, kinking, and buckling (see **Figures 11** and **16c**).

When a projectile hits the individual fiber or a yarn [14, 16], longitudinal and transverse waves propagate from the impact point. Most of the kinetic energy transfers from the projectile to the principal yarns (those that come directly into contact with the projectile). The orthogonal yarns, which intersect the principal yarns, absorb less energy. The transient deformation within the fabric was simulated by Grujicic et al. [12]. The transverse deflection continuously increases until it reaches the breaking strain of the fibers and causes failure. Failure mechanisms characterizing the fabrics under ballistic impact include

- breakage of fiber bonds and yarns,
- yarn pullout,
- remote yarn failure,
- wedge-through phenomenon (hole smaller than the diameter of projectile),
- fibrillation,
- effects induced by friction between the projectile and the fabric, yarn, and fibers.

In accordance with the kinetic theory of rupture, breaking the bond occurs when it is excited beyond its activating energy. When activation energy or stress for a particular type of destruction is reached, the failure mechanism is triggered.

Localized fracture of the yarn occurs when all fibers of the yarn break almost in the same location, usually at the sharpest point of a penetrator. This type of failure is accompanied by a popping sound and a sudden decrease in the measured load. The two causes of yarn breakage are the traction of yarns along their length and the shear in their thickness. The fiber in this yarn will break when the induced strain exceeds the strain at breakage that depends also on the strain rate but the strain at breakage generally decreases as the strain rate increases.

The breakage of yarns could occur at different points along their length and not necessarily at the point of impact. Also, if the penetrator is not too sharp, it compresses the superficial material between its front and the bulk material, outside its contact to the target, and the yarns could be pulled up and could break in traction.

In multilayered (stratified) systems, **friction** between layers is important in reducing damage [11]. All projectiles penetrating through a fabric, with semispherical, ogival, or conical shape, cause a splitting of the yarns [25]. Martinez et al. [26] have stipulated that pulling or rubbing is involved during the fabric-woven manufacturing and that its severity depends on the contact pressure between the layers.

The yarn pulling occurs when none of the yarn fibers break, but the yarn is pulled out of the fabric mesh. This type of failure can happen to lose or unfixed yarns (on the edge). The force required to pull the yarn from the net depends on the frictional force on the contact area between the yarn in question and the other perpendicular yarns with which it intersects (for woven fabrics) or on the friction among yarns and sublayers when the fabric is made of unidirectional yarns. As the yarn is pulled out, the number of yarns intersecting constantly decreases, resulting in a gradual decrease in the measured impact load.

Splitting of fibers along their length or fibrillation is a type of destruction favored by the abrasive action on the fiber length (but also uneven traction along the fiber and their local defects play an important role in fibrillation).

The bowing is dominant in the back layers of a multilayer panel, where the projectile attempts to penetrate through a tip-edge approach, after that, it is considerably slowed down by the back layers that did not fail. The passing process of the projectile through the layers usually produces a hole less than the diameter of the projectile in the first layers, a smaller number of yarns being broken as compared to the number of threads intersecting or contacting the projectile [27]. Typical aspects of the aramid fiber failure are given in **Figures 12** and **13**: micro-fibrillation, peeling, and shear, but also fiber twisting and thinning zones along the fiber. An obvious less strain rate could be noticed in **Figure 13** as compared to that in **Figure 12**.

A study at the macro- and micro-level was done for pointing out the failure processes characterizing each layer. **Figure 14** shows the front and back views of the panel made of 12 layers LFT SB1plus. On this type of package, a partial penetration was obtained, that is, the destruction of the first four layers of the panels. The photographs show the entire pack after testing with three shots. It is obvious from **Figure 14** that the design of the unidirectional fabrics helps yarns to develop a better resistance against pulling out.

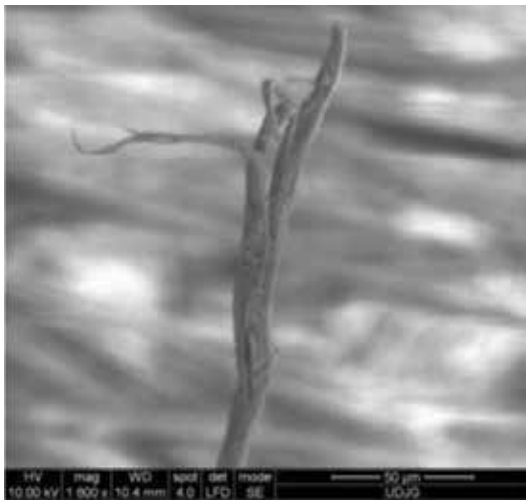

Figure 13. A fiber broken on the back of the last layer (the 12th layer).

The layers may be grouped as follows (**Figure 14**):

- layers with hole dimensions less than the projectile diameter (layers 1 and 2 from the studied panel),
- layers laterally impelled (pushed) (layers 3 and 4),
- layers only compressed, with a shallow print of the arrested bullet (layers 5–11),

the last layer with pull-out yarns and disorder yarns, especially on the back of the last layer (layer 12).

An investigation of the arrested bullet offers details on how the yarns are broken. **Figure 15** shows that the projectile attack makes the yarn to break laterally from the direct impact, mainly from tensile solicitation. On the top of the projectile, the fragment of the yarn remains. One may notice an orientation similar but not exactly as the orientation of yarns in the four sublayers (0, 90, 45, −45), meaning the bullet is forced to change the initial position due to yarn resistance and break unevenly. The jacket of the bullet is split like a flower petal and migrates toward the boundary of the lead core. When the core hits the target, it is strongly compressed and laterally expanded, some of the yarn fragments being embedded into the lead alloy.

The holes in layers 1 and 2 are similar, resulting that the process of yarn destruction is also similar, which argues that the perforation of the first two layers is made approximately with the same parameters (the velocity of the bullet through the first two layers is not significantly reduced and the shape of the bullet is not modified too much because it does not face yet the resistance of the other layers and it only cuts the yarns, as it is presented in a FE model in [11, 14]. It is worth mentioning that the tests were carried out under conditions of a small variations in the initial bullet velocity (410–430 m/s). The impact angle is normal on the target surface, with deviations of less than 5% at the mouth of the pipe.

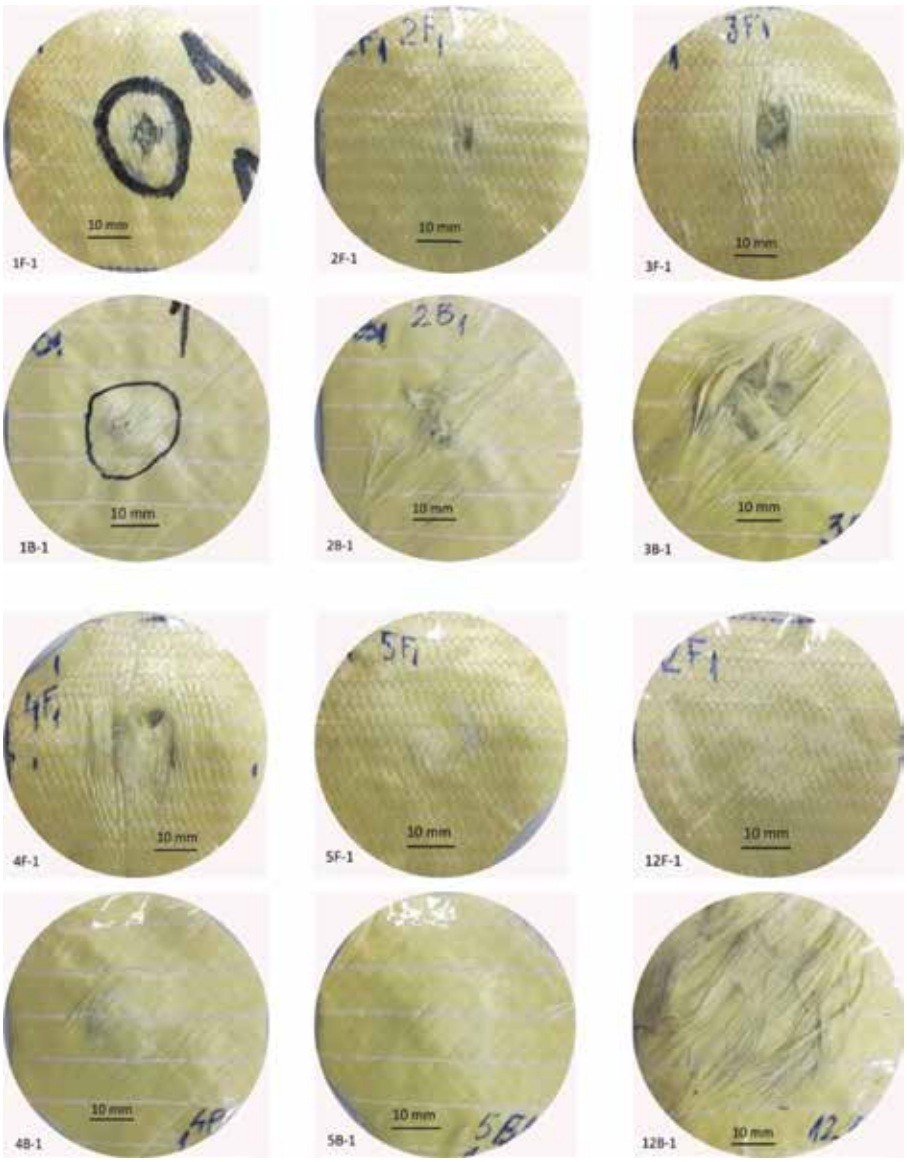

Figure 14. Macrophotographic study of a panel made of 12 layers of LFT SB1plus.

Starting from layers 3 and 4, the widening of holes and the pulling-out process of the yarns are noticed. Layer 4 is the last layer in the LFT SB1plus panels through which bullets have passed or stopped (arrested).

Layer 5 shows more uniformly circular shapes of crushing/compression, imparting a tendency to uniformize the response of the material.

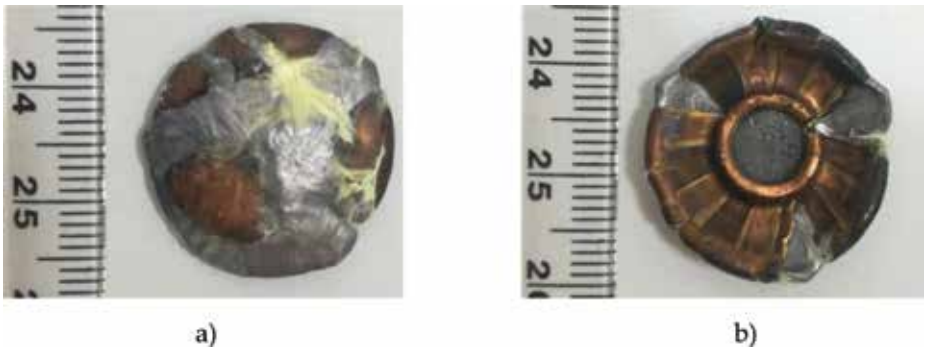

Figure 15. The bullet extracted from the sample panel presented in **Figure 14**. (a) Front view. (b) back view of the same bullet.

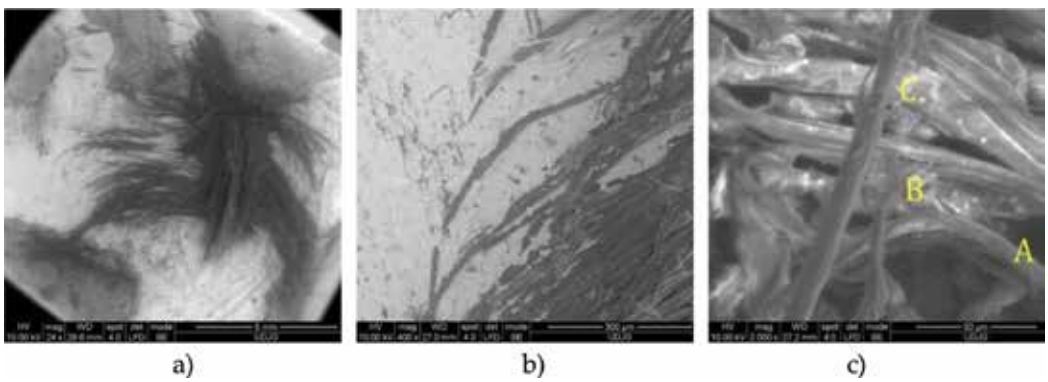

Figure 16. SEM images of the bullet with fragments of yarns on its front. (a) SEM image of the flattened bullet, as extracted between the fourth and the fifth layer. (b) Magnification of embedded fibers, very probably from the first yarn touching the bullet. (c) A—Fibrillation, B—Break by tensile loading with twisting of the fiber end, C—Necking of the fiber without break.

Figure 16a shows the fragmentation of fibers and the embedding of the yarn fragments remained under the bullet, with details shown in **Figure 16b**. **Figure 16c** points out the types of failures on the fibers remained on the projectile.

5. A statistical analysis of backface signature

The values of BFS for panels made of layers LFT SB1plus are given in **Table 5** and they were measured according to Ballistic Resistance of Body Armor, NIJ Standard-0101.06, 2008 [4].

NIJ Standard-0101.06 [4] asks for having fires complying with requirements concerning the shot-to-edge distance and shot-to-shot distance (minimum of 51 mm). For armor types subjected to a single threat and for the lighter weight threat round when two threats are

LFT SB1plus Layers/identification code	Shots		
	1	2	3
	BFS (mm)		
12/8	18	12	23
12/9	16	14	20
12/11	20	24	21
12/12	21	23	21
12/14	17	22	19
8/3	27	TP	
8/5	30	TP	
8/6	31	33	TP
4/1	TP		
4/2	TP		
4/3	TP		

Table 5. BFS for panels made of layers of LFT SB1plus.

specified, the minimum shot-to-edge distance shall not be greater than 51 mm. For the heavier threat round when two threats are specified, the minimum shot-to-edge distance shall not be greater than 76 mm.

Each test panel must withstand the appropriate number of fair hits and may not experience any perforations. Any complete perforation by a fair hit constitutes a failure. Each new size of a body armor model shall either have no BFS depth measurements that exceed 44 mm (**Figure 17**), or for each threat round, an estimated probability of a single BFS depth measurement exceeding 44 mm of less than 20% with a confidence of 95%.

The armor model shall be deemed to meet these requirements if no BFS depth measurement due to a fair hit exceeds 50 mm, and either

- all BFS measurements due to fair hits are 44 mm or less or
- the one-sided tolerance interval for a normal distribution indicates that there is 95% probability that 80% of the test BFS measurements for armor samples of that particular model, size, condition, and test threat will be 44 mm or less.

In this case, the upper tolerance limit, Y_U, and the sample standard deviation, s, of all recorded BFS measurements for body armor sample panels of a particular model, size, condition, and test threat shall be calculated, and

$$Y_U = \overline{Y} + K_1 s \tag{1}$$

where $\overline{Y}$ is the average of all BFS measurements for armor samples of that particular model, size, condition, and test threat; s is the sample standard deviation of the same set of BFS measurements; and K_1 is a factor that must be determined such that the interval covers the appropriate proportion, with a confidence of γ.

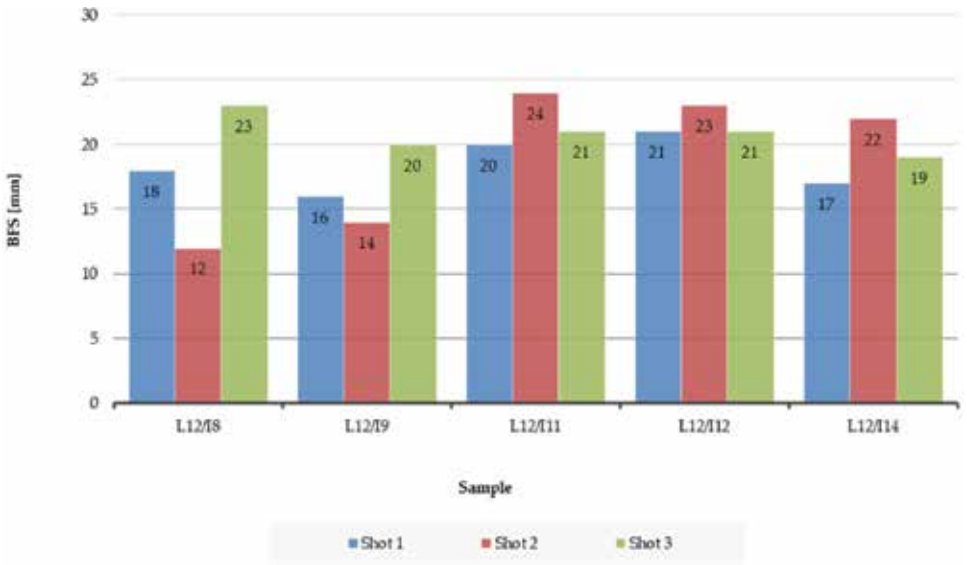

Figure 17. BFS results, based on the number of shoots/panel, for panels made of 12 layers of LFT B1plus.

The average $\overline{Y}$ is simply calculated as

$$\acute{Y} = \frac{1}{N}\sum_{i=l}^{N} Y_i \tag{2}$$

where N is the number of BSF measurements and Yi is the BFS value for the i-th shot. The standard deviation of the sample population, s, is calculated with the relationship:

$$s = \sqrt{\frac{1}{N-1}}\sum_{i=1}^{N}\left(Y_i - \acute{Y}\right)^2 \tag{3}$$

The approximate factor, k_1, for a one-sided tolerance interval can be calculated as

$$K_1 = \frac{z_{1-p} + \sqrt{z_{1-p}^2 - ab}}{a} \tag{4}$$

where z_{1-p} is the critical value of the normal distribution which is overpassed with a probability $1 - p$. The factors a and b are defined as

$$a = 1 - \frac{z_{1-\gamma}^2}{2(N-1)} \tag{5}$$

$$b = z_{1-p}^2 - \frac{z_{1-\gamma}^2}{N} \tag{6}$$

where z_{1-p} is the critical normal distribution which is overpassed by a probability $1 - \gamma$.

In order to analyze the BFS measurements in accordance with [4], the probability for no BFS measurement to be higher than 44 mm has to be at least 80%, thus $p = 0.80$ and the confidence coefficient is 95%

$$\gamma = 0.95 \tag{7}$$

The critical values for the normal distribution for this case study are

$$z_{1-\gamma} = z_{0.05} = 1.645$$

$$z_{1-p} = z_{0.20} = 0.842$$

Using these data, the factors a and b may be calculated for an imposed number of BFS measurements, N. For N = 15, the factors a and b are

$$a = 1 - \frac{1.645^2}{2(15-1)} = 0.903, \qquad b = 0.842^2 - \frac{1.645^2}{15} = 0.528.$$

And the factor k_1 is

$$k_1 = \frac{0.842 + \sqrt{0.842^2 - 0.903 \cdot 0.528}}{0.903} \approx 1.466$$

The allowable excessive BFS probability, 20%, may appear to be high; however, this value is intended to account for both the variation in the armor's performance, which should be small, and the variation in the BFS measurement due to the backing material and the backing material preparation. While careful treatment and preparation of the backing material by the test laboratory can minimize the variation due to the backing material, there will always be some inherent variation introduced into the test results by the backing material. The required probability is chosen to reduce that possibility that an acceptable armor design will fail the PBFS test due to reasonable variation in the backing clay.

The average value of BFS $\acute{Y}$ was calculated for panels made of 12 layers of LFT SB1plus, with N = 15 (the values of BFS are given in **Table 5**)

$$\acute{Y} = \frac{1}{N} \sum_{i=l}^{N} Y_i = 19.4 \; mm$$

where N is the number of measured BFSs and Y_i is the value of measurement i for BFS.

The standard deviation of the sample population, s, for panels made of 12 layers LFT SB1 plus is equal to

$$s = \sqrt{\frac{1}{N-1}} \sum_{i=1}^{N} \left(Y_i - \acute{Y} \right)^2 = 3.439$$

The upper tolerance limit, Y_u, for panels made of 12 layers LFT SB1plus is

$$Y_u = \acute{Y} + k_1 s = 19.4 + 1.466 \cdot 3.439 = 24.441\ mm$$

6. Conclusions

This chapter underlines the necessity of testing ballistic protection packs made of LFT SB1 plus against a certain threat in order to assess their resistance to this specific threat and the investigation of failure mechanisms in order to improve their behavior at ballistic impact.

Ballistic testing of the LFT SB1 plus panels can provide reliable information about the new material.

Tests made on packs made of LFT SB1 plus according to NIJ Standard-0101.06-2008 gave good results for the packs made of 12 layers of this fabric and the BFS was measured.

The upper tolerance limit of 24,441 mm obtained for backface signature recommends this panel of 12 layers of LFT SB1 plus for protection level of IIA, according to the abovementioned standard.

Author details

Catalin Pirvu[1]* and Lorena Deleanu[2]

*Address all correspondence to: pirvu.catalin@incas.ro

1 National Institute for Aerospace Research "Elie Carafoli"—INCAS, Bucharest, Romania

2 Department of Mechanical Engineering, "Dunarea de Jos" University of Galati, Galati, Romania,

References

[1] Năstăsescu V, Ştefan A, Lupoiu C. Analiza neliniară prin metoda elementelor finite. Fundamente teoretice şi aplicaţii. Academia Tehnică Militară Bucureşti. 2001

[2] Cunniff P. Fiber Research for Soldier Protection. U.S. Army Natick Soldier Research. Development and Engineering Center; 2010

[3] Hinton MJ, Kaddour AS, Soden PD. Failure Criteria in Fibre Reinforced Polymer Composites: The World-Wide Failure Exercise. UK: Elsevier Ltd; 2004. ISBN: 978-0-08-044475-8

[4] Ballistic Resistance of Body Armor, NIJ Standard-0101.06, U.S. Department of Justice Office of Justice Programs National Institute of Justice; 2008

[5] Department of Justice, National Institute of Justice. NIJ Standard 0108.01 US. Ballistic Resistant Protective Materials; September 1985

[6] Montgomery JS, Chin ES. Protecting the future force: A new generation of metallic armors leads the way. AMPTIAC Quarterly. 2004;**8**(4):15-20

[7] Cunniff PM. An analysis of the system effects in woven fabrics under ballistic impact. Textile Research Journal. 1992;**62**(9):495-509

[8] Lakunin VY, Shablygin MV, Sklyarova GB, Tkacheva LV. Assortment and properties of aramid fibres manufactured by Kamenskvolokno Co. Fibre Chemistry. 2010;**42**(3)

[9] Ballistics Teijin Aramid, Ballistics Material Handbook 38-1405/2012; 2012

[10] National Research Council. Opportunities in Protection Materials Science and Technology for Future Army Applications. The National Academies Press; 2011. ISBN: 978-0-309-21285-4

[11] Pirvu C, Ionescu TF, Deleanu L, Badea S. Simplified simulation of impact bullet—Stratified pack for restraining ballistic tests. In: 21st Innovative Manufacturing Engineering & Energy International Conference—IManE&E. Romania: MATEC Web Conf; Vol. 112; 2017. DOI: https://doi.org/10.1051/matecconf/201711206023

[12] Grujicic M, Bell WC, Arakere G, He T, Xie X, Cheeseman BA. Development of a meso-scale material model for ballistic fabric and its use in flexible-armor protection systems. Journal of Materials Engineering and Performance. 2010;**19**(1):22-39

[13] Grujicic M, Snipes J, Ramaswami S, Avuthu V, Yen CF, Cheeseman B. Unit-cell-based derivation of the material models for armor-grade composites with different architectures of ultra-high molecular-weight polyethylene fibers. International Journal of Structural Integrity. 2010;**7**(4):458-489. ISSN: 1757-9864

[14] Pirvu C. Contribuţii la studiul experimental şi numeric al pachetelor de protecţie balistică cu fibre aramidice [thesis]. Dunarea de Jos University Galati; 2015

[15] Purushothaman A, Coimbatore G, Ramkumar SS. Soft body armor for law enforcement applications. Journal of Engineered Fibers and Fabrics. 2013;**8**:97-103

[16] Safta I. Contribuţii la studiul teoretic şi experimental al mijloacelor individuale de protecţie balistică [thesis]. Military Technical Academy Bucharest; 2011

[17] Shockey DA, Erlich DC, Simons JW. Lightweight fragment barriers for commercial aircraft. In: The 18th International Symposium on Ballistics San Antonio; 1999

[18] Chitrangad I. Hybrid Ballistic Fabric, Patent No. 5,187,003; 1993. Available from: http://www.freepatentsonline.com/5187003.pdf [Accessed: January 05, 2018]

[19] Zeng XS, Shim VPW, Tan VBC. Influence of boundary conditions on the ballistic performance of high-strength fabric targets. International Journal of Impact Engineering. 2005; **32**(1–4):631-642

[20] Lim CT, Tan VBC, Cheong CH. Perforation of highstrength double-ply fabric system by varying shaped projectiles. International Journal of Impact Engineering. 2002;**27**(6):577-591

[21] Dischler L. Bullet Resistant Fabric and Method of Manufacture. U.S. Patent 6,248,676; 2002. Available from: http://www.google.com/patents/about?id=nGsIAAAAEBAJ&dq=Martin-Electronics&ie=ISO-8859-1 [Accessed: January 05, 2018]

[22] Carrillo JG, Gamboa RA, Flores-Johnson EA, Gonzalez-Chi PI. Ballistic performance of thermoplastic composite laminates made from aramid woven fabric and polypropylene matrix. Polymer Testing. 2012;**31**:512-519

[23] Bhatnagar A. Lightweight Ballistic Composites. Boca Raton Boston New York: CRC Press; 2006

[24] Allen SR, Filippov AG, Farris RJ, Thomas EL. Macrostructure and mechanical behavior of fibers of poly-p-phenylene benzobisthiazole. Journal of Applied Polymer Science. 1981; **26**(1):291-301

[25] de Koning CAM, Dreumel WHM. Mechanical Jointing in Aramid Fibre Composites. An Experimental Study, Report LR-371. Department of Aerospace Engineering. Delft University of Technology; 1983

[26] Martinez MA, Navarro C, Cortis R, Rodriguez J, Sanchez-Galvez V. Friction and Wear Behaviour of Kevlar Fabrics. Journal of Materials Science. Vol. 28. pp. 1305-1311. Springer. New York: Science + Business Media; 1993

[27] Al-Bastaki NMS. Design of fibre reinforced composite structures subjected to high strain rates using finite element analysis. Applied Composite Materials. 1998;**5**:223-236. Kluwer Academic Publishers

[28] Yahaya R, Sapuan SM, Jawaid M, Leman Z, Zainudin ES. Quasi-static penetration and ballistic properties of kenaf-aramid hybrid composites. Materials and Design 63. Elsevier Ltd; 2014. p. 775-782

Edited by Charles Osheku

The edited volume *Ballistics* is a collection of reviewed and relevant research chapters, offering a comprehensive overview of recent developments in the field of engineered mechanics. The book comprises single chapters authored by various researchers and edited by an expert from the respective research area. Each chapter is complete in itself but united under a common research study topic. This publication aims to provide a thorough overview of the latest research efforts by international authors on engineered mechanics and opens new possible research paths for further novel developments.

Published in London, UK

IntechOpen

ISBN 978-1-83880-715-3
9 789535 125365